Astrophysical Contributions to the *Fermi* Galactic Centre GeV Excess

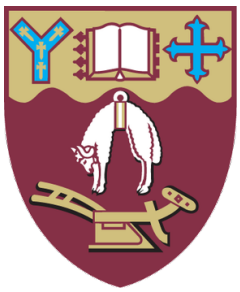

Dylan Paterson

School of Physical and Chemical Sciences
University of Canterbury

This dissertation is submitted for the degree of
Doctor of Philosophy

March 2020

For my parents.

Acknowledgements

I would like to thank my PhD supervisor, Chris, for his support and guidance. My friends, especially Ethan and Becca, thank you for the welcome distractions from my thesis work. (R.I.P. Eldrin). Maybe one day we will find all of the dimension artifacts. Special thanks to Brendan, these projects would have been a much bigger challenge without your insight. My family, thank you for the support during my time at university. I promise I will do my best to start positively contributing to society. Lastly, thank you to my loving wife, Amber, for bringing joy to my life (and ~~proof-reading~~ proofreading this thesis).

Abstract

An excess of GeV gamma rays above the expected astrophysical background has been detected in the region of the sky towards the centre of the Milky Way using observations from the *Fermi* Large Area Telescope. Early studies of the gamma-ray excess found that the spatial morphology and spectrum was consistent with annihilation of dark matter particles in the core of the galaxy. This thesis considers the astrophysical contributions to the gamma-ray landscape in the inner Milky Way. Spatial models are presented for the diffuse background of gamma rays from cosmic ray interactions with interstellar gas and extended emission from an unresolved population of millisecond pulsars.

Cosmic rays diffusing through the Milky Way produce gamma rays via the production and subsequent decay of π mesons, or bremsstrahlung, when interacting with the interstellar medium. The expected spatial distribution of the resulting gamma rays can then be modelled by the 3-D distribution of gas in the galaxy. Assuming the gas clouds move on circular orbits in the galaxy with a fixed rotation curve, the Doppler shift of the 21cm spectral line is used to place the atomic hydrogen into annular regions. A similar process is used for 2.6mm line emission of carbon monoxide to construct the 3-D distribution of molecular hydrogen, assuming the two species are well mixed. The gas column density is linearly interpolated along galactic longitude in the inner galaxy ($|l| < 10^{\circ}$) to account for the lack of kinematic resolution. An alternative model that uses hydrodynamic simulations to predict the orbital velocity field is also considered. In an analysis of 7 years of *Fermi* Large Area Telescope observations, the gas maps generated using the hydrodynamic method provides a statistically better fit to the gamma-ray background than the interpolated method recommended by the Fermi Collaboration. Including a contribution to the gamma-ray emission model from an unresolved population of millisecond pulsars, using the nuclear bulge and stellar boxy-bulge as a proxy, further improves the fit. Once the stellar contribution is accounted for, a spherically symmetric component, consistent with the annihilation of dark matter, only improves the fit by $2.7\,\sigma$.

To improve the previously used description of the boxy-bulge, a non parametric model is developed to reconstruct the stellar density in the Galactic bulge using the red clump giant stars in the Vista Variables in Via Lactea survey. The non parametric model uses maximum entropy regularisation and algorithmic smoothing regularisation to penalise the likelihood, allowing the stellar density to be reconstructed on a high resolution grid with nearly two million free parameters. A parametric model is also fitted to the VVV catalogues to use as a prior estimate of the density for the non parametric method. A number of systematic tests are performed on both the VVV data and a realistic synthetic population to test the robustness of the non parametric model. The reconstructed stellar density of VVV stars exhibits the boxy/peanut/X-shaped morphology as found with previous studies. Both the parametric and non parametric model densities provide an improved fit to the *Fermi* data, further supporting the millisecond pulsar explanation of the Galactic centre excess.

Table of contents

List of figures

List of tables

Nomenclature

Acronyms / Abbreviations

AGBB Asymptotic Giant Branch Bump

CASU Cambridge Astronomical Survey Unit

CSSM Constrained Minimalistic Supersymmetric Standard Model

CMZ Central Molecular Zone

CO Carbon Monoxide

DM Dark Matter

DNM Dark Neutral Medium

FB Fermi Bubbles

GCE Galactic Centre Excess

H_2 Molecular Hydrogen

HII Ionised Hydrogen

HI Atomic Hydrogen

IC Inverse Compton scattering

IEM Interstellar Emission Model

IMF Initial Mass Function

ISM Interstellar Medium

ISRF Interstellar Radiation Field

L-BFGS Limited Memory Broyden-Fletcher-Goldfarb-Shannon

LAT Large Area Telescope

LMXB Low Mass X-ray Binary

MEM Maximum Entropy Methods

MSP Millisecond Pulsar

NB Nuclear Bulge

NFW Navarro-Frenk-White

NP New Point sources

PSF Point Spread Function

RC Red Clump

RGBB Red Giant Branch Bump

RGB Red Giant Branch

TS Test Statistic

VVV Vista Variables in Via Lactea

WIMP Weakly Interacting Massive Particle

WNM Warm Neutral Medium

Chapter 1

Introduction

The centre of the Milky Way is host to a variety of high energy astrophysical phenomena including the super-massive black hole, Sgr A*, a dense nucleus of stars showing signs of recent bursts of star formation, potentially tens of thousands of compact stellar remnants in the stellar bulge, and the core of the dark matter halo that hosts our galaxy. Recent studies of the Galactic centre with the gamma ray satellite *Fermi* have detected an extended, nearly spherical anomalous signal. Many groups have studied the excess gamma rays, trying to discern the source, and hopefully detect the first non-gravitational evidence of dark matter. It is, however, unlikely that the gamma ray excess is coming from a single source, and is more likely a combination of astrophysical sources and potentially a dark matter source. In order to the constrain properties of a potential dark matter annihilation gamma ray source in the Galactic centre, we need to model all possible astrophysical contributions. The work we present in this thesis is concerned with the modelling of astrophysical sources of gamma rays towards the Galactic centre, in particular, the diffuse gamma rays produced in the interactions between cosmic rays and the interstellar medium, and gamma rays from millisecond pulsars in the Galactic bulge. In the following sections of this chapter we describe the nature of the *Fermi* Galactic centre excess (GCE) and motivate the unmodelled sources that likely contribute to it.

1.1 *Fermi* Large Area Telescope

The *Fermi* Large Area Telescope (LAT) is a gamma ray pair production telescope aboard the Fermi Gamma-ray Space Telescope satellite observatory (Atwood et al., 2009). Incoming gamma rays collide with a layer of tungsten foil, where they produce

an electron/positron pair. The path of the electron and positron through the detector is tracked by stacked layers of silicon detectors, which can be used to reconstruct the incoming direction of the incident gamma ray. A calorimeter also measures the energy of the particle pair, so that the initial energy of the gamma ray can also be inferred. Every incoming gamma ray is thus attributed an energy and a reconstructed origin on the sky, based on the pointing history of *Fermi*-LAT. The electron/positron pair produced by low energy gamma rays have less momentum than those produced from high energy gamma rays, so are more prone to multiple scattering as they move through the detector. This means that the photon reconstruction containment angle (and resulting image point spread function) is dependent on the photon energy. The containment angle for *Fermi*-LAT is 3° at 20 MeV (the lowest energy sensitivity limit), 0.2° at 2 GeV and 0.1° at 300 GeV (the highest energy sensitivity limit).

Fermi has nearly continuously surveyed the whole sky since its mission start in August 2008. Since then, a number of studies have reported an excess of gamma rays towards the Galactic centre above the expected astrophysical background (Goodenough et al., 2009; Boyarsky et al., 2011; Hooper et al., 2011a; Abazajian et al., 2012; Gordon et al., 2013; Macias et al., 2014; Abazajian et al., 2014; Ajello et al., 2016). Based on its nearly spherical morphology and gamma-ray spectrum that peaks at $\sim$ 2GeV, a number of explanations have been proposed. These include: annihilation of dark matter particles (Goodenough et al., 2009; Gordon et al., 2013; Abazajian et al., 2014), a population of unresolved millisecond pulsars (Abazajian, 2011; Gordon et al., 2013), or a recent series of comic-ray bursts from the the Galactic centre (Cholis et al., 2015). In the following sections we motivate these three possible sources of the GCE.

1.2 Dark Matter

Modern cosmological models tell us that nearly 80% of the matter in the universe is dark, cold and non-baryonic. Despite its apparent abundance, dark matter has never been definitively detected through non-gravitational observations or experiments. A likely candidate for dark matter is an exotic particle that is massive, electrically neutral, and stable over the lifetime of the universe. For an excellent review of particle candidates of dark matter, refer to Bertone et al., 2005. In this thesis, we only consider the well motivated Weakly Interacting Massive Particle (WIMP) candidate, though most of the conclusions are independent of the precise nature of the dark matter particle.

The very early universe was dominated by radiation, so much so that thermal equilibrium of particle species were maintained by spontaneous production/annihilation via interactions with the radiation field. As the universe cooled and expanded, the interaction rates decreased and particle species that were unable to maintain thermal equilibrium would freeze-out. The weaker the interaction, and thus the smaller the thermally averaged cross section $\langle \sigma v \rangle$, the earlier in the history of the universe a particular species would decouple from the radiation field. For particles that couple to the radiation field via the weak nuclear force, e.g WIMPs, the required thermal relic annihilation cross section to produce the dark matter content observed in the universe today is $\langle \sigma v \rangle_{WIMP} \approx 3 \times 10^{26}$ cm^{3}s^{-1}.

A number of experiments have searched for evidence of a $\sim$ 1-100 GeV/c^2 WIMP, either through direct WIMP-nucleon scattering, production in a particle collider, or indirect detection of WIMP annihilation in astrophysical systems. Direct detection experiments have not observed any significant WIMP-nucleon scattering signals, aside from the seasonally modulating DAMA/LIBRA "WIMP wind" (Bernabei et al., 2013), which has not been detected by other similarly sensitive detectors e.g LUX, XENON or PandaX-II (Akerib et al., 2017; Aprile et al., 2018; Tan et al., 2016). These experiments are reaching sensitivities capable of probing the mass-cross section parameter space for WIMPs predicted in minimal supersymmetry models, see Fig. 1.1. For further discussion on the recent experimental status of direct detection results see the thorough review in Roszkowski et al., 2018. The ATLAS and CMS collaborations have reported no evidence of supersymmetry from the 13 TeV experiments at the LHC, ruling out the most simple WIMP dark matter models for particle masses up to 250 GeV/c^2 (Atlas Collaboration, 2016; CMS Collaboration, 2017). See Arcadi et al., 2018 for an extensive review of searches for WIMPs in collider experiments. Observing the gamma rays from the annihilation of WIMP dark matter is an example of indirect detection. The expected gamma-ray spectrum is of the form

$$\frac{\mathrm{d}\phi_\gamma}{\mathrm{dE}_\gamma} = \underbrace{\frac{1}{4\pi}\frac{\langle \sigma v \rangle}{2m_\chi^2}\frac{\mathrm{d}N_\gamma}{\mathrm{d}E_\gamma}}_{\text{Particle Physics}} \times \underbrace{\int_{\Delta\Omega}\int_{\text{l.o.s.}} \rho^2_{\mathrm{DM}}(r)\mathrm{d}s\mathrm{d}\Omega}_{\text{Astrophysical J Factor}}, \tag{1.1}$$

where the energy dependence of the gamma-ray spectrum, $\frac{\mathrm{d}\phi_\gamma}{\mathrm{dE}_\gamma}$, ($\phi_\gamma$ is the gamma-ray flux and E_γ is the photon energy) is from the particle physics (left) term of the spectrum and spatial morphology is determined via the integral of the square of the dark matter density (ρ_{DM}) over the line-of-sight distance (s) and solid angle (Ω) in the astrophysical

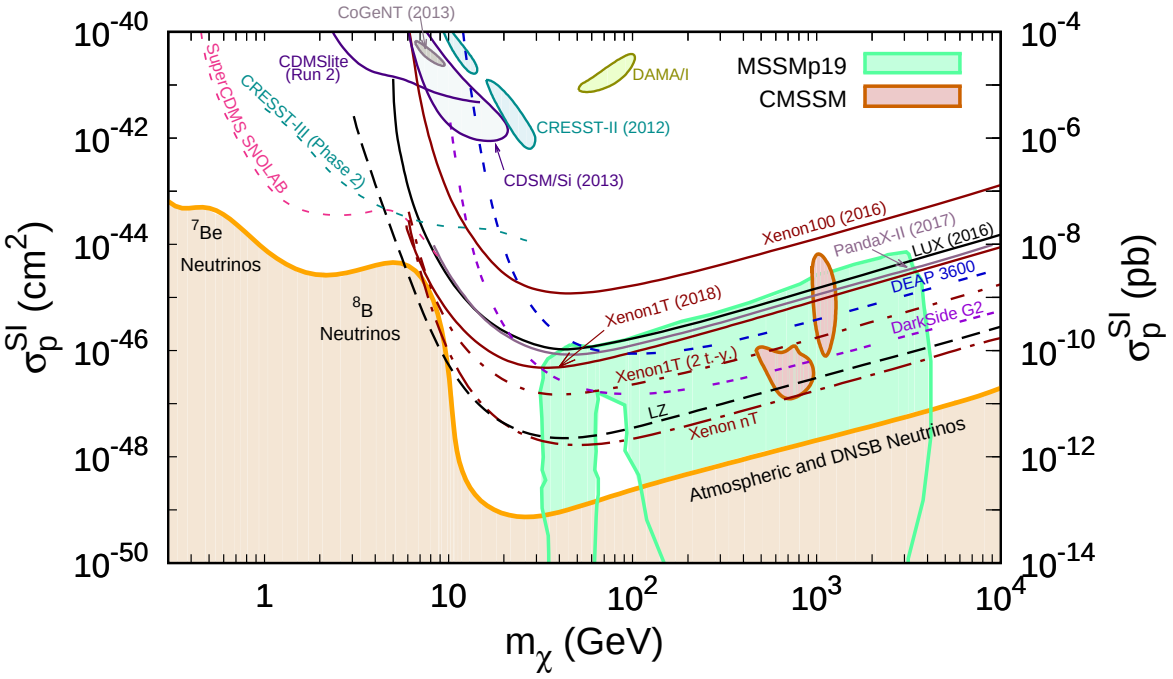

Fig. 1.1 Constraints on the WIMP-nucleon cross section (σ^{SI}) from current direct detection experiments (solid lines) and predicted constraints from future experiments (dashed lines). Direct detection experiments are starting to probe the parameter space predicted by simple supersymmetry models, constrained minimal super-symmetric Standard Model (CMSSM) or 19 parameter minimal super-symmetric Standard Model (MSSMp19) (green and red shaded regions). Figure from Roszkowski et al., 2018)

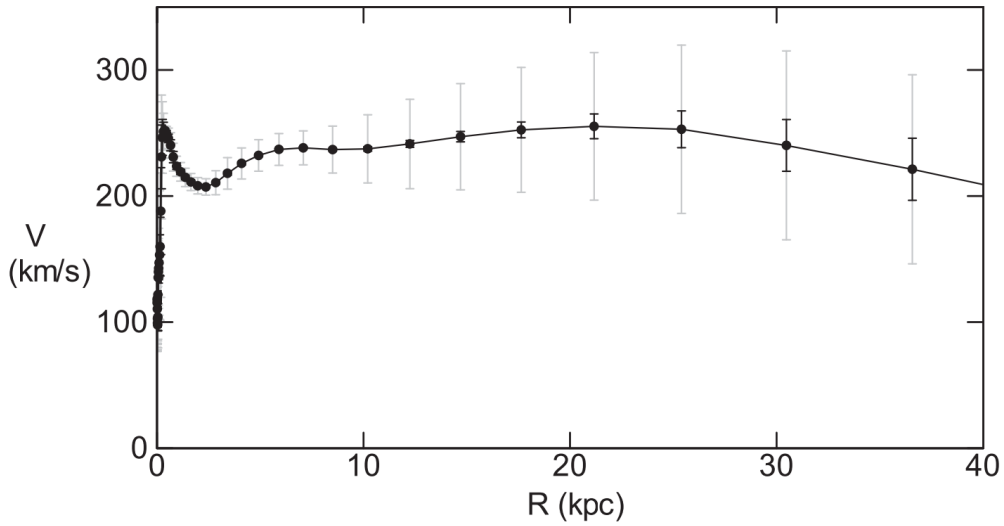

Fig. 1.2 Milky Way rotation curve of Sofue, 2015 from 21cm observations of atomic hydrogen.

J factor (right). WIMP dark matter does not directly annihilate to gamma rays, instead the gamma ray production is mediated by a pair of standard model particle/antiparticle e.g $b\bar{b}$ quarks or $\tau^+\tau^-$ leptons. The final state gamma-ray spectrum $\frac{\mathrm{dN}_\gamma}{\mathrm{dE}_\gamma}$ thus depends on the annihilation channel, which need not be limited to a single pair of mediating standard model particles. Also, note that there is a degeneracy between the thermally average cross section, $\langle\sigma v\rangle$, and the square of the mass of the dark matter particle, m_χ. For WIMP dark matter, we can assume that $\langle\sigma v\rangle$ is constrained by the present day dark matter density to be near the thermal relic density $\langle\sigma v\rangle_{\mathrm{WIMP}} \sim 3 \times 10^{26}$ cm^3 s^{-1}. In this way, the non-detection of a significant annihilation signal can place sensitivity based constraints on the mass of the WIMP dark matter particle. Combining these constraints with results from direct detection and collider experiments provides us with a way to narrow down the allowed parameter space (which is extremely vast *a priori*) for dark matter particle candidates, even without the positive identification of a dark matter signal. This thesis only considers the WIMP candidate for cold dark matter (e.g the neutralino in supersymmetry), but these experiments also place constraints on the parameter space of other particle candidates e.g the sterile neutrino in warm dark matter models, the QCD axion, or the ultra-light scalar in fuzzy/self-interacting dark matter models (Bertone et al., 2005).

The density distribution of dark matter in the Milky Way is a key factor in modelling a hypothetical dark matter annihilation gamma ray signal as an explanation for the

GCE. The density profile of the Milky Way dark matter halo can be inferred from the kinematics of gas and stars. Observations of the motions of gas in the Milky Way show that the rotation curve is flattened at distances $R > 10$ kpc from the Galactic centre, as in Fig. 1.2. At these distances, nearly all of the visible matter in the Milky Way is contained within the orbiting gas, so the orbital speed should start to drop off as predicted by Kelper's third law $V_{\rm orbital} \sim 1/R$ (Toomre, 1963). This suggests the stars and gas of the Milky Way are embedded in an invisible, nearly spherical, halo of matter that extends to at least 50 kpc from the Galactic centre (Freeman, 1970). Unfortunately, the gravitational potential of the inner ~ 3 kpc of the Milky Way is dominated by the contribution from stars and gas, introducing large uncertainties in the reconstructed dark matter profile of the inner galaxy (Pato et al., 2015). Three popular models of the dark matter density profile are usually considered in the literature. The first is the generalised Navarro-Frenk-White (NFW) (Navarro et al., 1996)

$$\rho_{\rm NFW}(r) = \frac{\rho_0}{\left(\frac{r}{r_s}\right)^{\gamma}\left[1+\left(\frac{r}{r_s}\right)\right]^{(3-\gamma)}}, \tag{1.2}$$

where r is the spherical distance from the Galactic centre, r_s is the scale length, and the index γ is the slope of the density profile in the inner galaxy. The second is the Einasto density profile (Einasto, 1974)

$$\rho_{\rm Einasto}(r) = \rho_0 \exp\left[-\frac{2}{\alpha}\left[\left(\frac{r}{r_s}\right)^{\alpha} - 1\right]\right], \tag{1.3}$$

where α is the shape parameter, and r and r_s are defined similarly as the NFW profile in Eq. 1.2. The third is the observationally motivated pseudo-isothermal sphere

$$\rho_{\rm Iso}(r) = \frac{\rho_0}{1+\left(\frac{r}{r_c}\right)^2}, \tag{1.4}$$

which, unlike the previous two density distributions, has a cored centre with core radius r_c. Cosmological N-body simulation of cold dark matter find that dark halos form with either NFW or Einasto density profiles (Navarro et al., 1996; Merritt et al., 2006). Whereas, observations of nearby galaxies find that spiral galaxies, like the Milky Way, tend to be well described by either a cuspy NFW/Einasto profile or a cored pseudo-isothermal profile. However, low surface brightness galaxies are only well described by cored profiles (de Blok et al., 2008). Early studies of the GCE found that the spatial morphology is consistent with the expected annihilation of dark matter

particles that are distributed with a NFW profile with inner slope $\gamma = 1.2$ (Abazajian et al., 2014; Gordon et al., 2013).

N-body simulations of cold dark matter also predict the formation of smaller subhaloes within the main dark halo that contain satellite galaxies (Zavala et al., 2019). In the Milky Way, the smallest of these that have been observed are the high mass-to-light ratio dwarf spheroidal galaxies. These smaller simulated subhaloes have shallower gravitational potentials than the main halo and have often been stripped of gas by interactions with baryons in the main halo (Kim et al., 2017). Without a significant gas or stellar population, dwarf spheroidal galaxies have significantly fewer gamma rays being produced by cosmic ray interactions than in the Milky Way. Considering the fainter local production of astrophysical gamma rays, and their positions on the sky away from the plane of the Milky Way, the satellite dwarf spheroidals are a good target for indirectly observing dark matter annihilation in gamma rays. Even so, there has been no significant evidence of dark matter annihilation above the expected astrophysical background in any of the Milky Way dwarf spheroidal galaxies, which rules out WIMP dark matter candidates with mass less than 100 GeV/c^2 (Ackermann et al., 2015; Hoof et al., 2018; Oakes, 2019). Since the dark matter in the subhaloes should be the same dark matter as in the main halo, the lack of any significant gamma ray signal from the dwarf spheroidals creates tension with any dark matter explanation of the GCE. One saving grace for the dark matter GCE there are considerable systematic uncertainties due the difficulty in determining the dark matter profiles in the dwarf spheroidal galaxies (Strigari, 2018).

1.3 Cosmic Rays

Cosmic rays are highly energetic charged particles that diffuse through the galaxy at nearly the speed of light. They are composed of mostly protons, electrons, and other heavy nuclei, with a small contribution from anti-matter. Interstellar magnetic fields cause cosmic rays to follow curved trajectories through space, so their observed incidence at Earth does not point back to their source. This makes studying the origin of cosmic rays an interesting challenge. Here we only give a brief overview that is particularly relevant to the nature of the GCE, but a thorough review is presented in Grenier et al., 2015.

As cosmic rays traverse the Milky Way, they lose energy to the environment through a number of processes; cosmic rays interact with protons in the interstellar

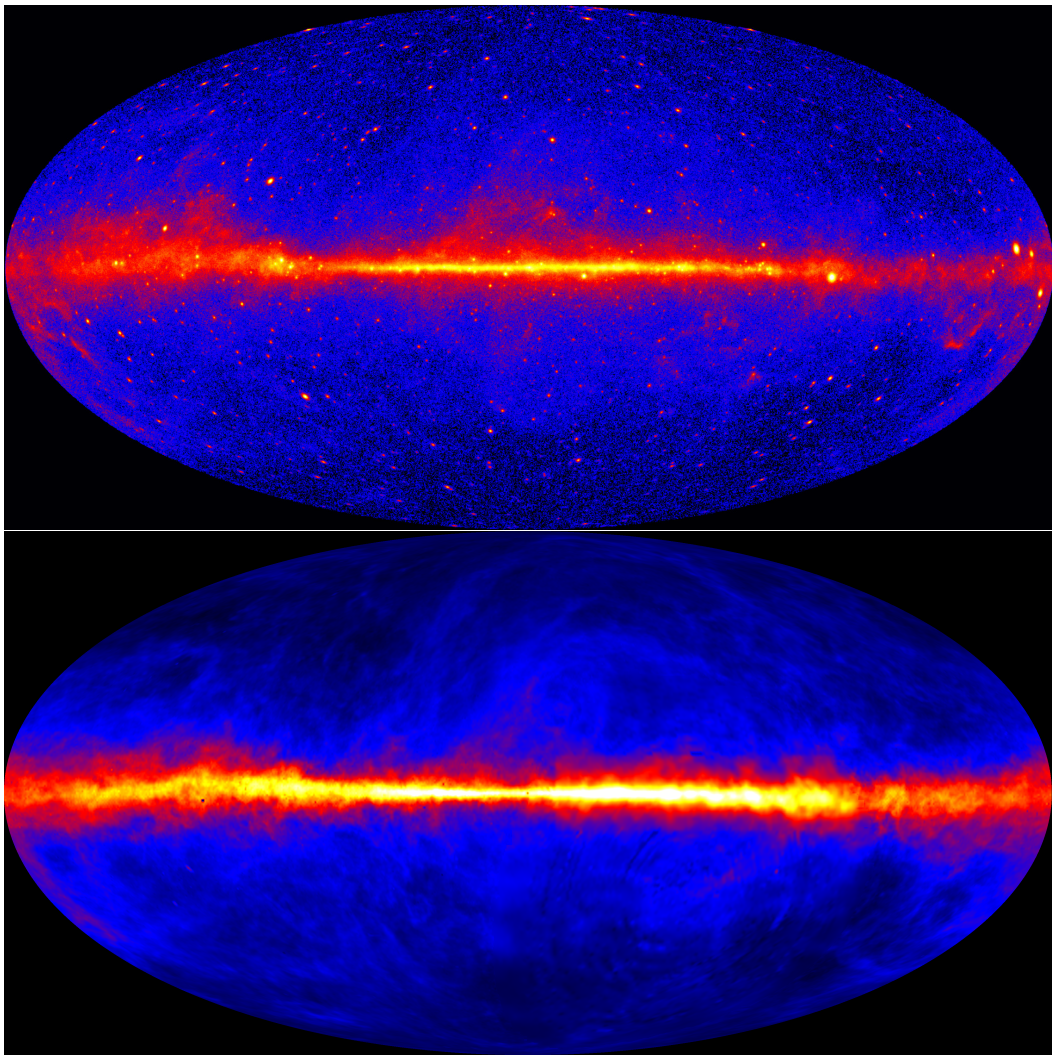

Fig. 1.3 *Fermi*-LAT 5 years combined observations (top) of > 1 GeV gamma rays compared to the atomic hydrogen column density from 21cm observations (bottom).

medium via bremsstrahlung, cosmic-ray protons produce π mesons through hadronic interactions with the interstellar medium, and cosmic-ray electrons radiate synchrotron radiation in magnetic fields or inverse Compton scatter with photons in the interstellar radiation field. All of these processes, except for synchrotron, are sufficiently energetic to produce gamma rays. In fact, interactions between cosmic-ray protons and the interstellar medium dominate the gamma ray sky at the ~ 10 GeV range. This is clearly evident by comparing the atomic hydrogen column density and the *Fermi* 5 year all sky observations as in Fig. 1.3. The combined contribution from these cosmic ray interactions make up the diffuse galactic gamma ray background. This is the subject of Chapter 2 in this thesis, so we defer any further discussion until then.

One explanation for the GCE is the interactions of cosmic rays from a recent outburst from a highly energetic source in the Galactic centre. Cosmic rays that originate in the galaxy are likely to be accelerated in phenomena that exhibit strong magnetic fields, such as supernova remnants (Ackermann et al., 2013) or pulsar wind nebulae (Lemoine et al., 2015). Ultra high energy cosmic rays from extra-galactic sources appear to originate from active galactic nuclei (IceCube Collaboration et al., 2018). A sensible conjecture then is that a burst of cosmic rays emitted from either accretion activity from Sgr A* or a burst of star formation in the nuclear bulge could have interacted with the local interstellar environment in the Galactic centre to produce the GCE. The spherical nature of the GCE rules out a bremsstrahlung/π_0 decay from the interaction of cosmic rays with the interstellar medium, which would be more extended in the plane of the galaxy. Studies of multiple *ad hoc* bursts of cosmic-ray electrons that produce gamma rays via inverse Compton are unable to describe the inner 1° of the GCE (Cholis et al., 2015). This explanation would still require another astrophysical source, such as an unresolved population of millisecond pulsars, to provide a full description of the GCE. Even so, there is evidence that there has been both Seyfert activity from Sgr A* in the last ∼3.5 Myr (Bland-Hawthorn et al., 2013; Bland-Hawthorn et al., 2019) and a recent (1 Gyr ago) burst of star formation in the nuclear bulge (Nogueras-Lara et al., 2019). Additionally, the large gamma ray lobes the *Fermi* bubbles (Su et al., 2010) further suggest a cosmic ray outburst originated from the Galactic centre in the recent past.

In summary, it is likely that a cosmic ray outburst from either Sgr A* or a starburst contributes to the gamma ray landscape in the inner galaxy. We do not, however, consider them as an explanation for the GCE in this thesis, as an additional astrophysical source would still be needed and the burst timings are, at worst, *ad hoc* and, at best, poorly constrained by model dependent observations.

1.4 Millisecond Pulsars

Millisecond pulsars are compact stellar remnants which have a rotation period on the order of 1-10 milliseconds. Strong magnetic fields generated by the rapidly rotating neutron star produce bipolar jets of charged particles. As the charge particles accelerate out from the neutron star, they lose energy in the from of curvature and synchrotron radiation, as they spiral along the curved magnetic fields. The synchrotron radiation is typically in the radio frequencies whereas the curvature radiation is much more

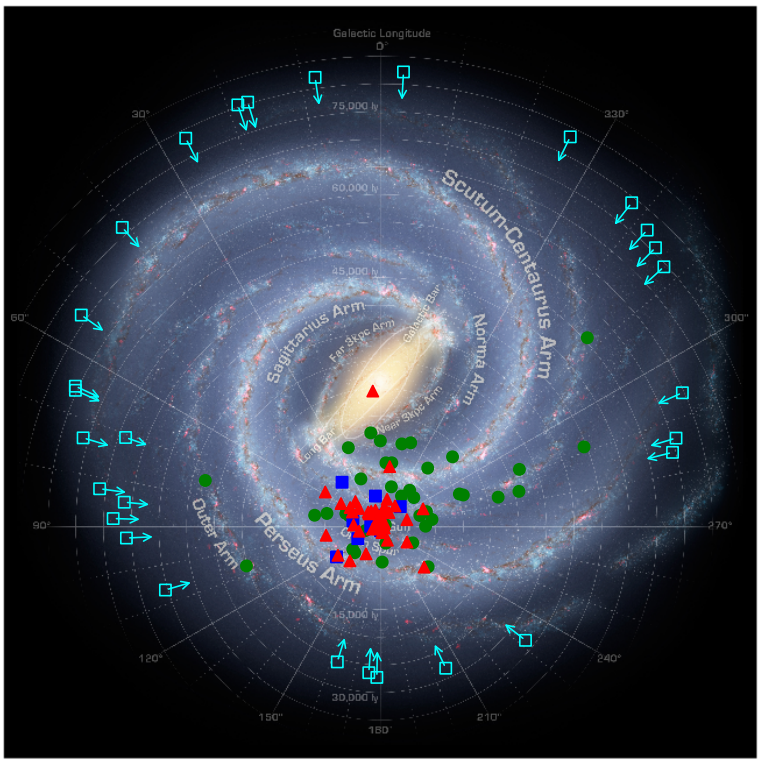

Fig. 1.4 Positions of the Gamma-Ray millisecond pulsars (red triangles) in the *Fermi* Large Area Telescope Pulsar Catalogue (Abdo et al., 2013). The millisecond pulsar which looks as though it is in the bulge is actually in the globular cluster NGC 6624, far above the Galactic midplane. Note that the distances derived from the dispersion measure are highly uncertain.

energetic, usually in the X-ray or gamma ray ranges. The radiation is highly directional, so is only visible when the beam is pointed towards Earth, making the neutron star appear to pulse. The Fermi collaboration maintain a list[1] of confirmed pulsars that have been observed with *Fermi*-LAT. At the time of writing this thesis, 234 pulsars have been detected, 103 of those are millisecond pulsars.

A population of unresolved millisecond pulsars is a popular candidate for an astrophysical explanation for the GCE (Abazajian, 2011; Gordon et al., 2013; Yuan et al., 2014; Brandt et al., 2015; Bartels et al., 2016). This view is further supported by

[1] https://confluence.slac.stanford.edu/display/GLAMCOG/Public+List+of+LAT-Detected+Gamma-Ray+Pulsars

studies of the photon statistics of the GCE, that suggest the clustering of the photons is more consistent with a faint, unresolved collection of point sources, rather than a truly extended source (Bartels et al., 2016; S. K. Lee et al., 2016). However, a more recent reanalysis suggests that the this conclusion does not completely rule out a dark matter explanation (Leane et al., 2019). Typically ∼1000 millisecond pulsars are needed to be consistent with the flux observed from the GCE, yet no millisecond pulsars have been resolved in the Galactic centre, see Fig. 1.4. Assuming the bulge millisecond pulsar luminosity function is the same as for disk millisecond pulsars, it is possible to have not resolved any in the bulge, while having enough unresolved to explain the GCE (Ploeg et al., 2017).

Origins for the population of millisecond pulsars broadly fall into two categories requiring two different formation histories for the bulge. The first, is the millisecond pulsars formed from stars that originated in globular clusters in the Milky Way, which were tidally merged into the bulge in the early history of the galaxy (Brandt et al., 2015). This is the *classical* spheroidal bulge formation model, which is further supported by the apparent spheroidal shape of GCE. Furthermore, the occurrence rate of millisecond pulsars is significantly higher in globular clusters (Camilo et al., 2005) than any of the other stellar populations of the Milky Way. Alternatively, the millisecond pulsars originate from stars that were in the disk population that puffed into a bulge through a buckling instability, via secular evolution (Kormendy et al., 2004). This view is supported by more recent studies, and work in the body of this thesis, which found the GCE is well described by the morphology of the stellar boxy-bulge (Bartels et al., 2018; Macias et al., 2018; Macias et al., 2019). It is currently unknown if the two populations have different pulsar formation efficiencies, and ultimately different millisecond pulsar luminosity functions.

A critical aspect in determining the luminosity function of the population of bulge millisecond puslars is how the stars formed into millisecond pulsars. The canonical model is the "recycled pulsar" (Cook et al., 1994), where an old pulsar, which has already lost most of its angular momentum, accretes material from a binary companion star. The infalling gas from the companion transfers angular momentum to the pulsar, causing it to spin back up to millisecond periods. Low-mass X-ray binaries (LMXB) are believed to be progenitor systems to the millisecond pulsar, and their distribution in the Galactic centre have been used to argue against the unresolved point-source interpretation of the GCE (Haggard et al., 2017).

If millisecond pulsars do not form as recycled pulsars, such as from the collapse of a white dwarf, then they do not necessarily exhibit a LMXB phase. Two theoretical channels exist; accretion induced collapse and merger induced collapse. A white dwarf near the Chandrasekhar limit (1.4 $M_{\odot}$) that is accreting from a low mass companion can undergo accretion induced collapse (Bhattacharya et al., 1991). The resulting neutron star is now significantly more compact than the progenitor white dwarf, so angular momentum conservation results in approximately millisecond period rotation. Alternatively, a binary pair of white dwarfs may initiate merger induced collapse (Ivanova et al., 2008), with a similar argument regarding the conservation of angular momentum allowing millisecond periods.

From the above considerations, an unresolved population of millisecond pulsars interpretation of the GCE a is plausibly suitable candidate. Differing formation histories of the stellar bulge, different possible formation channels for millisecond pulsars, and the unknown effects on the stellar environments on the formation efficiencies and resulting pulsar luminosity function makes it difficult to effectively constrain the properties of the Galactic centre millisecond pulsar population with current observations. Future missions with increased sensitivity will allow millisecond pulsars to be observed directly in the Galactic centre, hopefully giving further insight to the properties of this elusive population of stellar remnants. The millisecond pulsar interpretation of the GCE will be the focus of Chapter 3, where we generate a description of the expected spatial distribution of gamma ray emission on the sky from a population of millisecond pulsars using the stellar bulge as a tracer.

Chapter 2

Diffuse Galactic Gamma Ray Background

2.1 Introduction

An anomalous gamma ray signal has been observed by the *Fermi*-LAT coming from the Galactic centre region. The first report of this Galactic centre excess (GCE) was by Goodenough et al., 2009, whose preliminary analysis showed the anomalous signal was morphologically and spectrally consistent with the annihilation of WIMP dark matter. While this might be the first indirect detection of dark matter with *Fermi*, Goodenough et al., 2009 were not able to rule out the possibility that another astrophysical phenomena might be responsible.

For an astrophysical source to be able to mimic the dark matter model in Goodenough et al., 2009, it needed to be a spherically symmetric extended source with angular diameter $\sim 2^{\circ}$, with a gamma-ray spectrum that peaked at ~ 2 GeV. In subsequent studies, a variety of astrophysical sources have been tested, including an unresolved population of millisecond pulsars or young pulsars (Abazajian, 2011; O'Leary et al., 2015), a burst of cosmic-ray protons impinging on the surrounding molecular gas (Chernyakova et al., 2011; Linden et al., 2012), or a burst of cosmic-ray electrons interacting with the interstellar radiation field (Cholis et al., 2015). As with the annihilation of dark matter interpretation of the GCE, any astrophysical interpretation of the GCE had no detectable, unique signature that could be used to definitely confirm the source.

The cosmic ray burst models are fine-tuned to match the gamma ray observations (Cholis et al., 2015), so without constraints on origin of the burst, it is difficult to

demarcate from the dark matter interpretation. The morphological degeneracy between a dark matter signal and an unresolved millisecond pulsar population could be broken by assuming pulsars are well traced by the Galactic bulge stellar content. A major challenge to the millisecond pulsar interpretation of the GCE is the number of low luminosity bulge millisecond pulsars required to have sufficient combined flux to match the GCE. No millisecond pulsars have been resolved by *Fermi* in the bulge. This apparent lack of pulsars was solved by Ploeg et al., 2017, who found that the probability to resolve zero pulsars, from a population numerous enough the explain the GCE, was $\sim 40\%$.

The *Fermi*-LAT Collaboration recommends a templated approach (Casandjian, 2015) to modelling gamma ray observations, where the predicted counts in a particular energy bin are

$$N_{pred}(E) = \sum_{i=H \ templates} q_i(E)\widetilde{I}_{H_i} + N_{IC}(E)\widetilde{I}_{IC_p}(E) + N_{iso}(E)\widetilde{I}_{iso} + N_{LoopI}(E)\widetilde{I}_{LoopI}$$
$$+N_{FB}(E)\widetilde{I}_{FB} + N_{limb}(E)\widetilde{I}_{limb} + \sum_{i=ps} N_{pt_i}(E)\widetilde{\delta}(i) + \sum_{i=es} N_{ext_i}(E)\widetilde{I}_{ext_i} + \widetilde{I}_{sun\_moon}(E). \tag{2.1}$$

All sources except point sources or extended sources ($\widetilde{\delta}(i)$ or $\widetilde{I}_{ext_i}$ in Eq. 2.1) make up the Interstellar Emission Model (IEM). Diffuse and extended sources of gamma rays are modelled by a template, $\widetilde{I}$, which describes the spatial distribution of the source intensity. The templates are modelled *a priori* from observations of a different region of the electromagnetic spectrum, or, in the case of inverse Compton, cosmic ray model predictions. A relatively small component of the total gamma-ray flux comes from the Sun and Moon ($\widetilde{I}_{sun\_moon}$).

Cosmic-ray electrons produce gamma rays by inverse Compton scattering of photons in the interstellar radiation field (ISRF) (Moskalenko et al., 2000). The template for inverse Compton, $\widetilde{I}_{IC}$ in Eq. 2.1, is strongly dependent on the environment in the Milky Way. The distribution of the gas, dust, stars and magnetic fields in the galaxy all affect the energy losses as the cosmic rays propagate (Ackermann et al., 2012). The morphology of the emission from inverse Compton scattering is not simply correlated to either the cosmic ray density or the interstellar radiation field. Instead, the emission must be predicted via numerically solving the cosmic ray transport equations e.g with GALPROP (Strong et al., 1998; Moskalenko et al., 1998) or DRAGON (Maccione et al., 2011)

The Fermi Bubbles (FB) are large lobes of gamma rays that extend exactly above and below the Galactic centre (Su et al., 2010). While the exact source of the FB is still unresolved, the leading theories suggest the gamma rays were produced by a burst of cosmic rays from the Galactic centre interacting with the coronal ISM or interstellar radiation field. Two sources of the cosmic ray burst have been explored in the literature; accretion activity from Sgr-A* (Bland-Hawthorn et al., 2013; Bland-Hawthorn et al., 2019) or a burst of recent star formation in the nuclear bulge and subsequent supernovae wind (Nogueras-Lara et al., 2019). Templates for the FB ($\widetilde{I}_{FB}$) are difficult to produce *a priori*, as they are very faint in other energy regimes e.g. in X-rays with *Röntgensatellit* (Bland-Hawthorn et al., 2003; Su et al., 2010) or *Suzaku* (Kataoka et al., 2013; Tahara et al., 2015). A template can be extracted from the *Fermi* observations using spectral component analysis, as the spectrum of the FB is harder than the other diffuse emission near the Galactic midplane (Ackermann et al., 2014). The spectral component analysis method does not perform well close to the Galactic midplane, where the point sources are densely concentrated. Alternatively, the FB template can be simply described by a catenary function (Acero et al., 2016).

Diffuse gamma rays have been observed in the direction of Loop I, a large scale radio loop coincident with the Sco-Cen OB association. (Casandjian et al., 2009). The source of the radio loop is not known, several possibilities have been suggested in the literature, such as nearby supernova winds from Sco-Cen OB association (Wolleben, 2007), or a similar origin to the FB (Kataoka et al., 2015). Even though the gamma ray emission is not exactly correlated with the radio loop, the recommended template for Loop I ($\widetilde{I}_{LoopI}$) is the analytic description derived from the DRAO 1.4 GHz polarization survey (Wolleben, 2007).

Cosmic rays produce gamma rays, via bremsstrahlung or spontaneous π_0 production and decay, with hydrogen atoms in the ISM. Interactions between cosmic rays and the ISM are accounted for by the first term of Eq. 2.1, where $\widetilde{I_H}$ is the ISM column density and $q(E)$, the gamma ray emissivity, is a free parameter. To account for differing gamma ray emissivities throughout the Milky Way, the ISM column density is separated into annular regions, each with its own free emissivity parameter.

Towards the Galactic centre, low energy (E $<$ 10 GeV) gamma ray emission is dominated by photons from the interactions of high energy cosmic rays with the interstellar environment (Ackermann et al., 2012). To study the GCE, which has a spectrum that peaks at $\sim$ 2 GeV, an accurate description of the 3-D distribution of the ISM is needed.

The majority of the gas in the ISM is hydrogen or helium, with heavier elements making up only $< 1\%$ of the total mass (Ferrière, 2001). The distribution of helium is largely unknown, as only one of its ionization states is observable. We have to assume that the ISM is traced by the distribution of hydrogen, which does make up $\sim 90\%$ of the mass in the ISM. Hydrogen is found in three distinct states in the ISM; atomic (HI), molecular (H_2) or ionised hydrogen (H_{II}). Ionized hydrogen only makes up about $\sim 15\%$ of the hydrogen mass budget, and most of that is concentrated in star formation regions, so for the ISM template, we use the column density of HI and H_2.

Nearly everything we understand about HI comes from observing the emission or absorption of 21cm line (Kalberla et al., 2009). To determine the column density of atomic hydrogen from 21cm emission, the spin temperature, T_s, must be known. Studies of the absorption of 21cm in the Milky Way, and the inferred T_s, have found that HI exists in two different phases (Dickey et al., 2009; Heiles et al., 2003). The warm neutral medium (WNM) has $T_s \sim 1000\ K$ and is diffusely spread through the Milky Way. The cold neutral medium has $T_s \sim 10\ K$ and is more clumped into clouds than the WNM. No large scale estimation for the distribution of T_s in the galaxy is available, so it is usually assumed that T_s is a uniform $100 - 200$ K throughout the Milky Way(Kalberla et al., 2009).

Molecular hydrogen does not have any radio emission lines considering the usual cold ISM conditions. Instead, H_2 is traced by the rotational transition 2.6mm emission from carbon monoxide (CO). Observations of the integrated line intensity of CO (W(CO)) have found it to be linearly correlated to H_2 column density (Dame et al., 2001; Solomon et al., 1987).

The Doppler shift in the line emission of the aforementioned tracer elements is used in this chapter to construct the 3-D gas distribution. It is common in the literature to assume that the gas clouds are on circular orbits about the Galactic centre (Kalberla et al., 2009). Non-circular streaming motions near the Galactic bar and spiral arm overdensities, expected to be up to ~ 30 kms^{-1} from simulations (Chemin et al., 2015), affect the observed emission line profile. One way to properly account for the streaming motion is to determine gas velocities in the Milky Way by hydrodynamical simulation (Pohl et al., 2008). Gas maps used in the generation of the Fermi IEM assume circular orbits, so that is the method used in this chapter (Casandjian, 2015; Ackermann et al., 2012).

In this chapter, we construct hydrogen column density maps using the method recommended for standard point source analysis by the Fermi Collaboration (Casand-

jian, 2015). We also construct gas maps using the hydrodynamical method of Pohl et al., 2008. Both gas maps are fitted to *Fermi* observations, where we show that, unsurprisingly, the hydrodynamic maps offer a better fit than the standard Fermi IEM method. In further analysis, we test the inclusion of new extended sources of gamma rays, such as the Galactic bulge, nuclear bulge and dark matter. The nuclear bulge + Galactic bulge offer a significant contribution to the gamma ray emission, while also ruling out the detection of a signal consistent with the annihilation of WIMP dark matter.

2.2 Gas Template Production Method

The template model of diffuse interstellar emission requires column density maps of both HI and H_2, a map for the predicted inverse Compton emission from cosmic ray electrons, and maps for any otherwise unmodelled residual emission (see Eq. 2.1). This method forgoes the need to know the distribution of cosmic rays, by assuming the cosmic ray properties are constant within annular regions of the galaxy. The templates are then fitted directly to the gamma ray data, with the normalization representing the gamma ray emissivity, which can vary between each annular region. The methods used in this analysis are based on those described in Appendix B of (Ackermann et al., 2012).

From the Doppler shift in the tracer particle line emissions (21cm and 2.6mm), the radial velocity can be inferred. Assuming circular orbits, the radial velocity relative to the local standard of rest is given by

$$v_{LSR} = R_\odot \left(\frac{V(R)}{R} - \frac{V_\odot}{R_\odot} \right) \sin(l) \cos(b) \tag{2.2}$$

where v_{LSR} is the radial velocity of the tracer particle for a particular line-of-sight, R is the Galactocentric radius, $V(R)$ is the orbital velocity, and (l, b) are the galactic longitude/latitude defining the line-of-sight. The distance to the Galactic centre, $R_\odot$, and the Sun's orbital velocity, $V_\odot$, were adopted as $R_\odot = 8.5\,\mathrm{kpc}$ and $V_\odot = 220\,\mathrm{km\,s^{-1}}$ to match the rotation curve used to determine $V(R)$ (Clemens, 1985).

The Galactocentric radius of tracer particles can be found by solving Equation 2.2. In the case of circular orbits, $\frac{V(R)}{R}$ is a monotonically decreasing function of R, so Equation 2.2 will have at most one root. It is possible that there are no roots when the observed radial velocity has the wrong sign. The terminal velocity for a particular line

of sight occurs where the radial velocity is tangential to the orbit $R = R_\odot \sin(l)$. The small number of pixels that have velocities exceeding the terminal velocity were assigned to the tangent annulus, under the assumption that the orbit is slightly non-circular. The significance of the circular orbit assumption is assessed in Sec. 2.6 by comparing the predicted terminal velocity from Eq. 2.2 to the observed terminal velocity.

For directions toward the Galactic centre ($l = 0\,^\circ$) and anticentre ($l = 180\,^\circ$), the kinematic resolution of the above technique disappears as v_{LSR} becomes zero. In the regions $|\,l\,| < 10\,^\circ$ and $|\,l - 180\,^\circ\,| < 10\,^\circ$ the gas column density was interpolated across l within each annulus, then renormalised across all annuli to preserve the total column density in each line-of-sight. The boundary values of the interpolation region were found by averaging the region spanning $\Delta l = 5\,^\circ$ at the boundary.

Gas that was found to be high above the Galactic plane was assigned to the local annulus (the one that spans 8.5 kpc). For HI, the height limit used was 1 kpc and for H_2 the height was restricted in latitude to $|\,b\,| < 4°$. In the case of HI, this showcases the near-far ambiguity in using circular obits. A single line of sight has two points on it that have Galactocentric radius R (except where it is tangent to an orbit), one which is near to the observer and one that is far from the observer. This effects the calculation of the height from the plane, as the further point has a greater height than the nearer point. In this work, the height was assumed to be that of the near point.

Through this process the emission was separated into Galactocentric annuli then converted to column density. The method for converting emission line profiles into column density is specific to the tracer particle and is covered in the relevant sections (Section 2.3 for HI and Section 2.4 for H_2).

2.3 Atomic Hydrogen

The distribution of the atomic hydrogen column density was derived from the Leiden-Agentine-Bonn 21 cm Galactic HI composite survey assuming a uniform spin temperature of $T_s = 170\,\mathrm{K}$ (Kalberla et al., 2005). The LAB survey is an all sky map of 21 cm brightness temperature, T_B, in an equirectangular projection with pixel size of $0.5° \times 0.5°$, in slices of observed radial velocity. Each pixel is thus uniquely described by a (l, b, v_{LSR}) value and contains a T_B value. The atomic hydrogen column density is given by

$$N(HI) = -C\,T_s \int dv \ln\left(1 - \frac{T_B(v)}{T_s - T_{\mathrm{bg}}}\right) \tag{2.3}$$

where $N(H\textsc{i})$ is the atomic hydrogen column density, $C = 1.83 \times 10^{18}\,\mathrm{cm}^{-2}$ and $T_{\mathrm{bg}} = 2.66\,\mathrm{K}$.

The procedure to generate the Galactocentric annuli of gas column density was broken into two parts. First the Galactocentric radius of the emission in each pixel of the survey data was calculated from Equation 2.2 and the pixel was assigned to the appropriate annulus. Each annulus was then integrated according to Eq. 2.3 to give the final column density. In this step the interpolation and renormalisation of the Galactic centre was performed.

Decomposing the annuli using a firm limit on the Galactocentric radius has the undesirable effect of occasionally splitting a single gas cloud across multiple annuli, as is seen in Fig. 2.1. A more elegant solution would be to perform a full spectral decomposition, by fitting a collection of Gaussian or similar functions to the emission line profiles, as was done in Chemin et al., 2009. We did not implement such an improvement at this stage, as the goal was to produce gas maps that were as similar as possible to those used in the standard *Fermi* IEM.

Shown in Fig. 2.2 are the atomic hydrogen column densities for nine annular regions in the Milky Way, assuming a spin temperature of 140K. All of the annuli compare well to the gas maps included in GALPROP (Strong et al., 1998; Moskalenko et al., 1998), which have been produced with a similar method. For the analysis of the *Fermi* observations in Sec. 2.7, only four broader annuli are used (shown in Fig. 2.11), as the small region of the sky we are fitting to offers less constraint on the diffuse galactic background compared to analyses that use a large sky coverage (Ackermann et al., 2012; Casandjian, 2015; Acero et al., 2016).

2.4 Molecular Hydrogen

The distribution of H_2 was derived from the Centre for Astrophysics 2.6mm CO composite survey, which offers a coverage of $|\,b\,| < 30\,^\circ$ over all galactic longitudes with a pixel size of $0.125^\circ \times 0.125\,^\circ$ (Dame et al., 2001). Similar to the LAB survey, the CO composite survey is in an equirectangular projection, sliced into observed v_{LSR} values with a radial velocity pixel spacing of $1.3\,\mathrm{km\,s}^{-1}$. Each pixel is uniquely defined by (l, b, v_{LSR}) values and contains a CO brightness temperature. To determine the molecular hydrogen column density from the CO brightness the following relation was used:

$$N(H_2) = X_{CO} \times W(CO) = X_{CO} \times \int dv\, T_B(v) \tag{2.4}$$

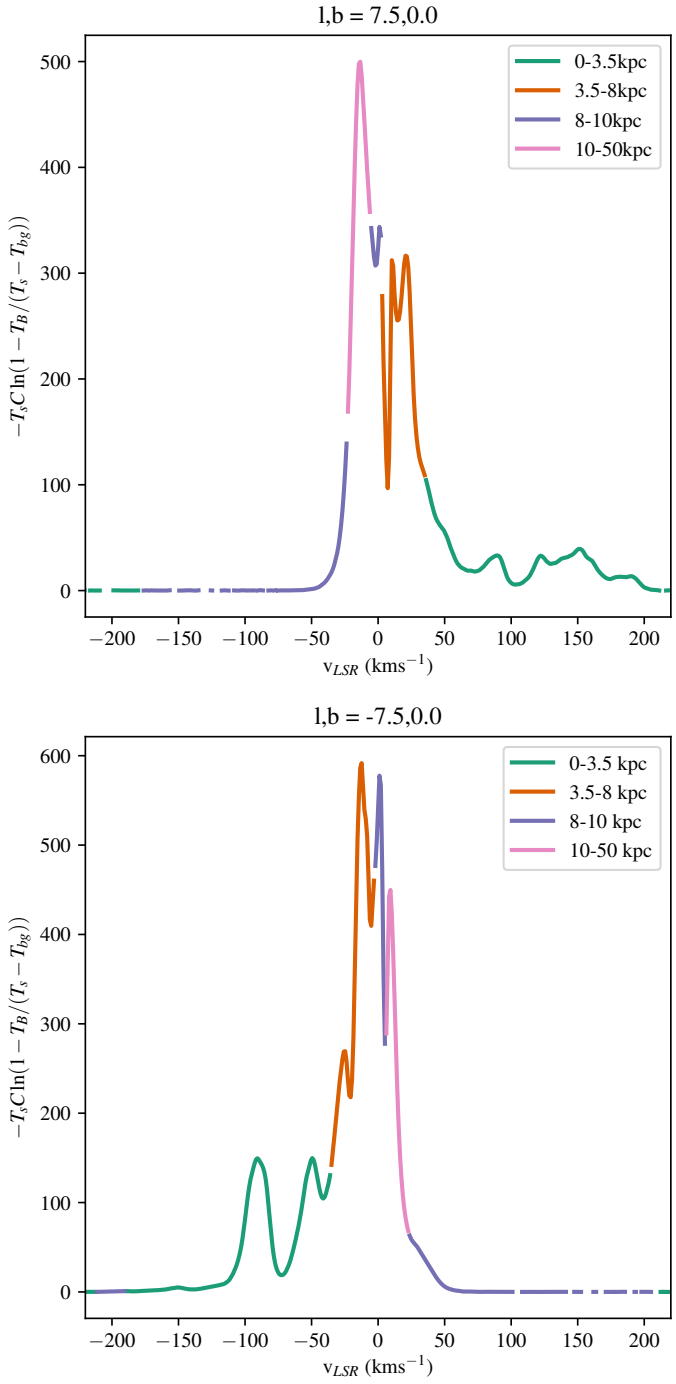

Fig. 2.1 Decomposition of the 21cm HI brightness temperature profile into galactocentric annuli. Not all of the emission from a single cloud is assigned to a single annuli, such as the emission that has been assigned to the $8-10$ kpc annulus at $l = 7.5°$

where X_{CO} is the molecular hydrogen to carbon monoxide density ratio and $W(CO)$ is the carbon monoxide velocity integrated 2.6mm line intensity. For the purpose of

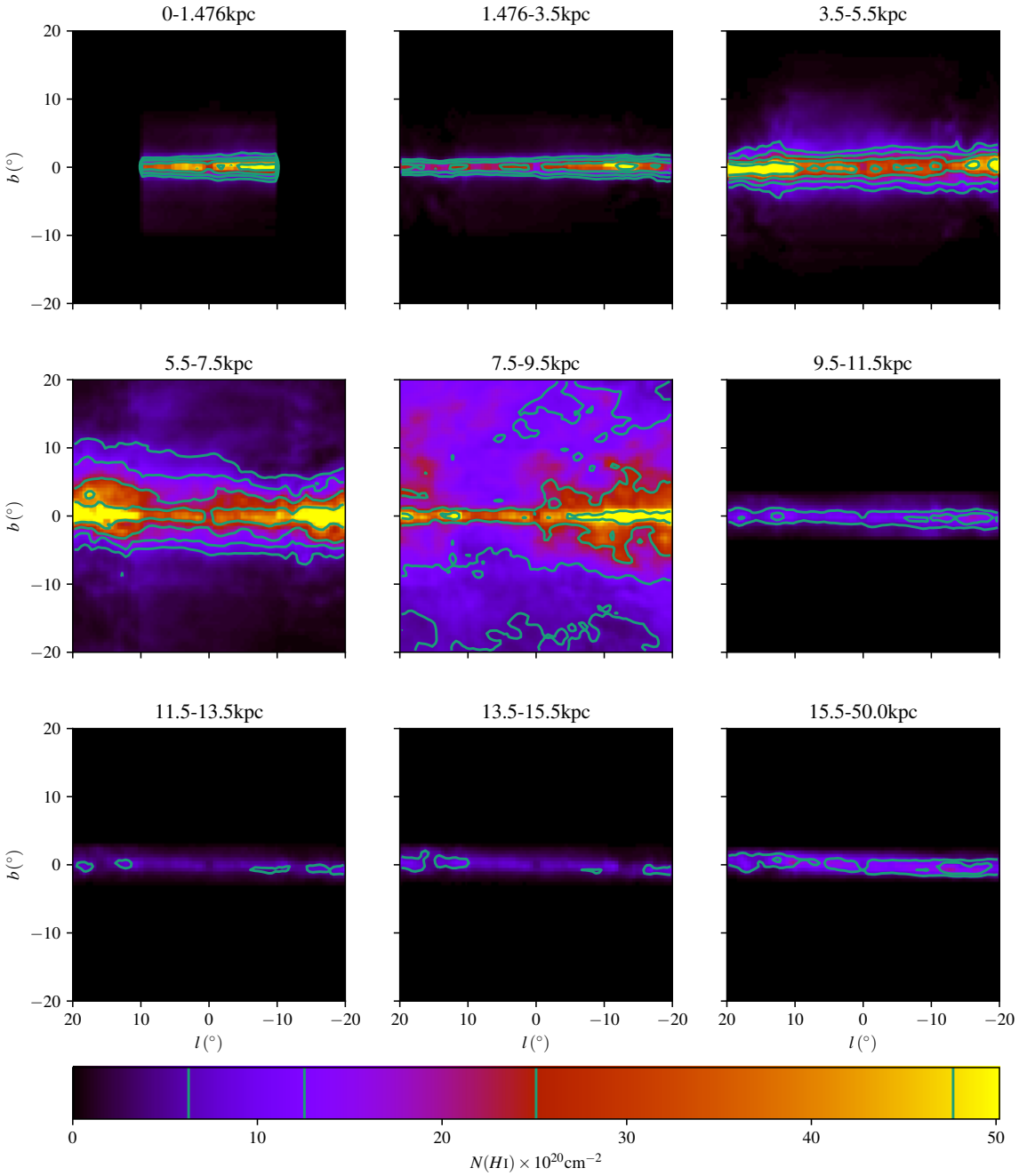

Fig. 2.2 Atomic hydrogen column density into nine annular regions within the Milky Way. Overlaid in green contours is the density maps included in GALPROP.

template production, it is sufficient to use simply the $W(CO)$ map as the X_{CO} value is absorbed into the gamma ray emissivity when fitting to the gamma ray data.

The procedure for generating the $W(CO)$ map was similar the $N(H\text{I})$ map in Section 2.3 with only three differences. The first difference is $W(CO)$ was calculated

from Equation 2.4. Secondly, the emission at $|b| > 4^\circ$ was assumed to be from the local annulus. Thirdly, the innermost annulus is assigned all emission observed with a high radial velocity. The high velocity bounds were chosen by inspection in Ackermann et al., 2012 as

$$v_{LSR} < (-50 + 3l)\,\mathrm{km\ s^{-1}} \tag{2.5}$$

$$v_{LSR} > \begin{cases} 25\,\mathrm{km\ s^{-1}} & l < 0^\circ \\ (10 + 3l)\,\mathrm{km\ s^{-1}} & l \geq 0^\circ \end{cases} \tag{2.6}$$

As in the atomic hydrogen case, the carbon monoxide clouds were sometimes split across multiple annuli as seen in Fig. 2.3. The carbon monoxide integrated intensity maps in Fig. 2.4 appear to show small overestimation in the outer (R > 9.5kpc) compared to the maps available in GALPROP. The method used to determine the carbon monoxide maps and atomic hydrogen are nearly identical, except for the treatment of the inner most annulus. For carbon monoxide, the inner most annulus contains the central molecular zone (CMZ), a dense, hot and turbulent cloud complex (Mills, 2017), which was specially placed in the inner annulus using the velocity cuts in Eq. 2.6. Since the outer annuli overdensity is only contained within the region that was interpolated, and the overdensity is not significantly present in the atomic hydrogen maps, the cause must be related to a combination of treatment of the CMZ and the interpolation and renormalisation at $|l| < 10^\circ$.

2.5 Dark Neutral Medium

Dark neutral matter (DNM) is hydrogen gas that is not traced by its respective tracer emission (21cm for HI and 2.6mm CO emission for H_2). Assuming that the gas is well mixed with dust, a $E(B-V)$ extinction map can be used to trace DNM (Grenier et al., 2005). The (Schlegel et al., 1998) $E(B-V)$ extinction map was used to derive the DNM density distribution by subtracting the components linearly correlated to the $N(HI)$ and $W(CO)$ maps. The residuals from this fit not only account for the DNM, but also for variations in X_{CO} and T_s, assuming the dust to hydrogen ratio is constant throughout the galaxy. The $E(B-V)$ extinction map used in this analysis was constructed from the full-sky 100 μm composite map from *COBE*/DIRBE and *IRAS*/ISSA, with zodiacal foreground and known point sources removed. Regions of high density infrared point sources still contaminate this map with emission that is not from thermal dust sources. Therefore, regions with high $E(B-V)$ extinction,

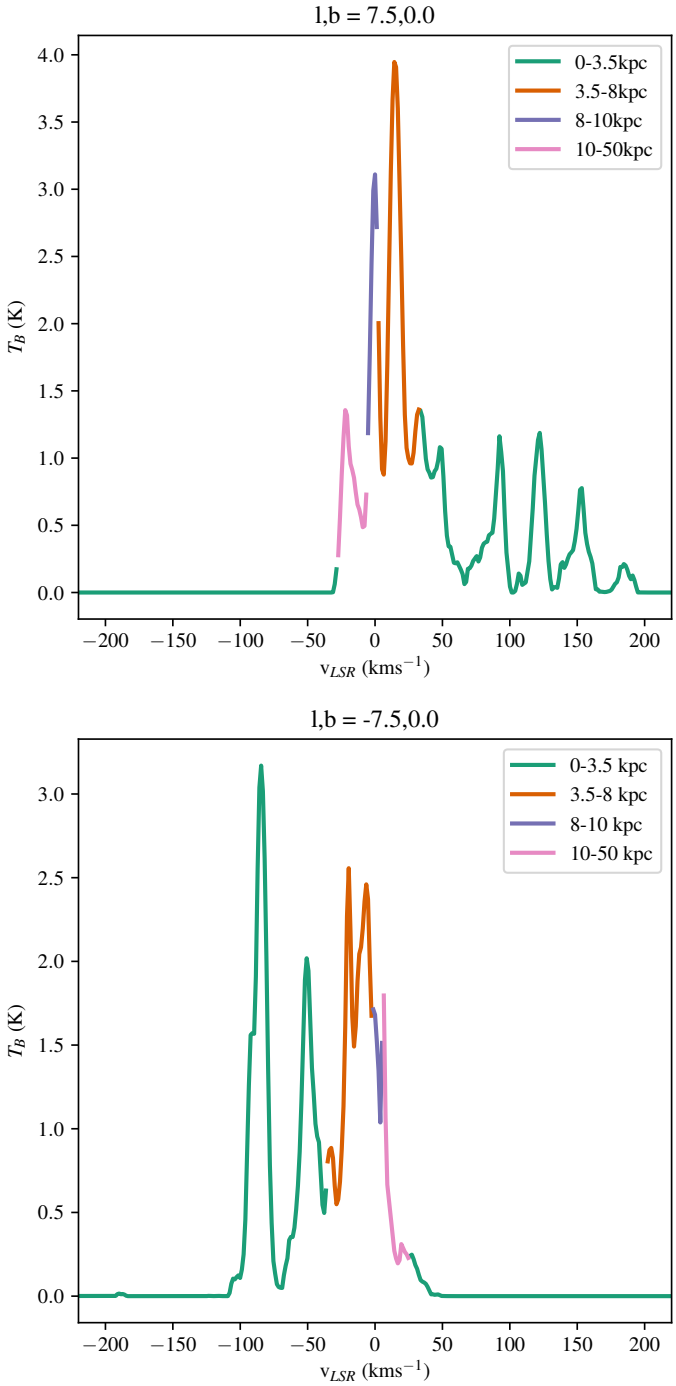

Fig. 2.3 Decomposition of the 2.6mm carbon monoxide brightness temperature profile into the four galactocentric annuli used in the analysis of the *Fermi* observations.

such as in the inner Galactic plane, can not be reliably used to determine the dust column density. Magnitude cuts of 5mag and 2mag were used to exclude regions of

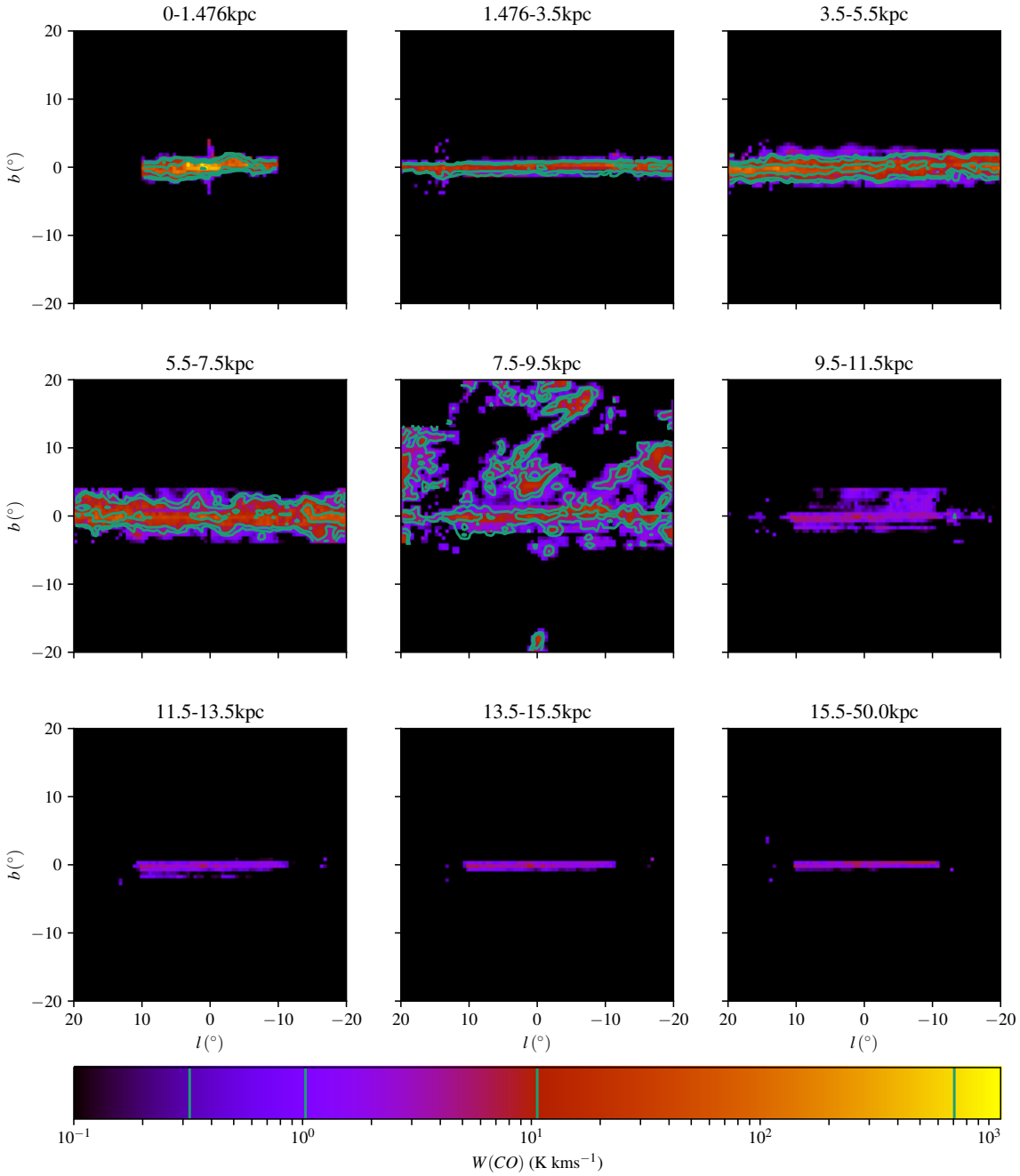

Fig. 2.4 Integrated carbon monoxide line intensity into nine annular regions within the Milky Way. Overlaid in green contours is the corresponding map included in GALPROP.

high $E(B-V)$ extinction, with the 2mag cut being the conservative limit and 5mag being the minimum limit.

A least squares fit was performed on the E(B-V) extinction map to a linear combination of the $N(H\textsc{i})$ and $W(CO)$ of the form

$$LS = \sum_{i=\text{pixels}} (E(B-V)_i - (a\,N(H\textsc{i})_i + b\,W(CO)_i))^2 \tag{2.7}$$

where a and b are the linear fit coefficients. Pixels with magnitudes higher than the $E(B-V)$ magnitude cut were excluded from the fit. The best fit coefficients were found by minimizing LS using Minuit[1]. The best fit combination of $N(H\textsc{i})$ and $W(CO)$ were subtracted from the $E(B-V)$ map to give the residual maps shown in Figure 2.5, with all pixels excluded from the fit by the magnitude cut set to zero. The residuals were split into two components, as they have different physical interpretations. Negative residuals can not be tracing DNM, so they were then interpreted as regions where T_s and X_{CO} are overestimated (the $N(H\textsc{i})$ and $W(CO)$ are too large in these regions). The positive residuals could be DNM, but also regions where T_s and X_{CO} have been underestimated.

2.6 Terminal Velocity Wavelet Analysis

Assuming that the terminal velocity occurs at the tangent point of a circular orbit, the rotation curve can be calculated from Eq. 2.2 by measuring the terminal velocity at every longitude. This method is called the tangent-point method, and is widely used, including by Clemens, 1985. In this section, the terminal velocity of the HI and CO surveys used in the preceding sections are measured using a wavelet method.

A variety of methods have been used in the literature to find the line with the largest radial velocity, ranging from a simple continuous signal-to-noise ratio threshold in Clemens, 1985, to a thorough spectral decomposition into multiple Gaussian components such as in Chemin et al., 2009. We take advantage of some properties of the continuous wavelet transform to identify the location and scale of the terminal velocity line.

The one dimensional wavelet transform of an emission line profile in a single line of sight is given by

$$\Psi(v,a) = \frac{1}{\sqrt{a}} \int_{-\infty}^{\infty} T_B\,(v')\psi(v-v',a)\,dv' \tag{2.8}$$

where a is the scale of the wavelet, v the radial velocity, T_B the emission line profile and ψ is the mother wavelet. For this convolution the Ricker wavelet (Ricker, 1943) is

[1] http://lcgapp.cern.ch/project/cls/work-packages/mathlibs/minuit/home.html

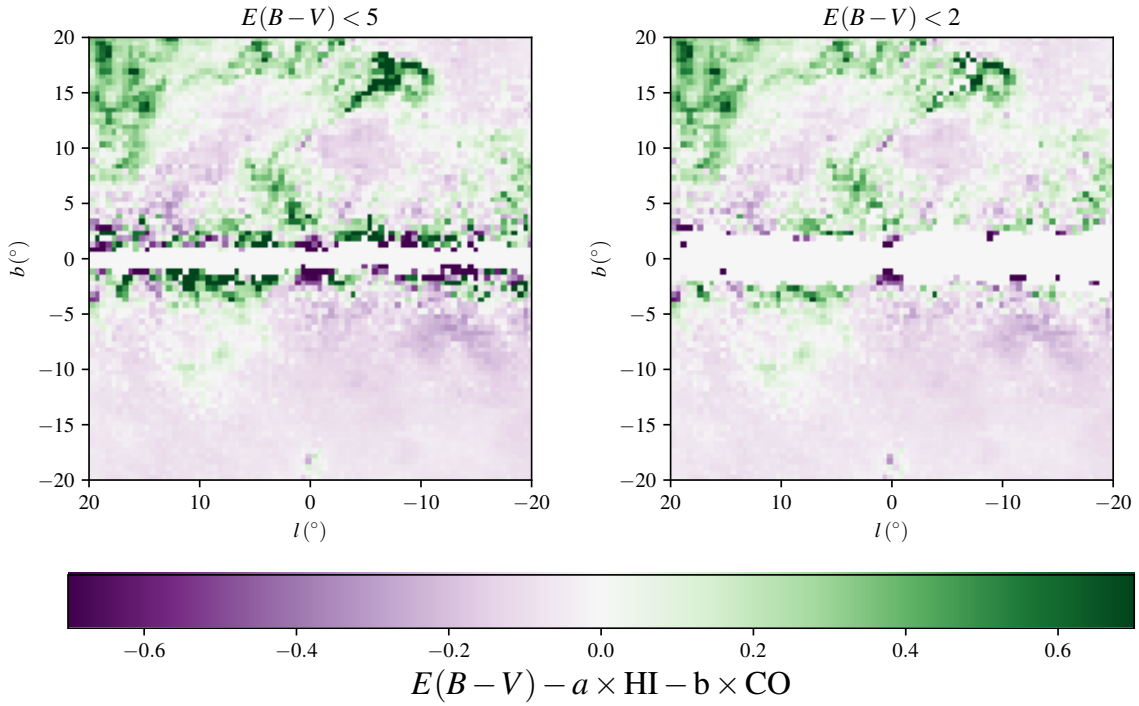

Fig. 2.5 Residuals from fitting a linear combination of atomic hydrogen column density and the carbon monoxide integrated line intensity to the $E(B-V)$ colour excess. Positive residuals represent hydrogen that is not traced by either of the 21cm or 2.6mm tracer emission. Negative residuals represent regions where the spin temperature or carbon monoxide-to-hydrogen ratio has been overestimated.

used:

$$\psi(v,a) = \frac{2}{\sqrt{3a}\pi^{1/4}}\left[1-\left(\frac{v}{a}\right)^2\right]e^{-\frac{1}{2}\left(\frac{v}{a}\right)^2} \tag{2.9}$$

Assuming the peaks in line profiles are Gaussian with mean μ and standard deviation σ, the wavelet transform has two useful properties (Damiani et al., 1997):

- Ψ will have a local maximum at $v = \mu$.
- The scale of wavelet, a, which gives the maximal $\frac{\Psi}{a}$ is related to the width of the peak by $\sigma = \frac{a}{\sqrt{3}}$

The procedure is then as follows;

1. For every longitude calculate the wavelet transform of the average brightness temperature profile for $|b| < 4^\circ$ over a range of wavelet scales.
2. Find the local maximum in the wavelet transform that has a brightness temperature with a signal-to-noise of at least 3.0 and the largest radial velocity.

3. Determine the width of the line by finding the scale that has the largest $\frac{\Psi}{a}$ and substituting into the equation in the second bullet of the above list.

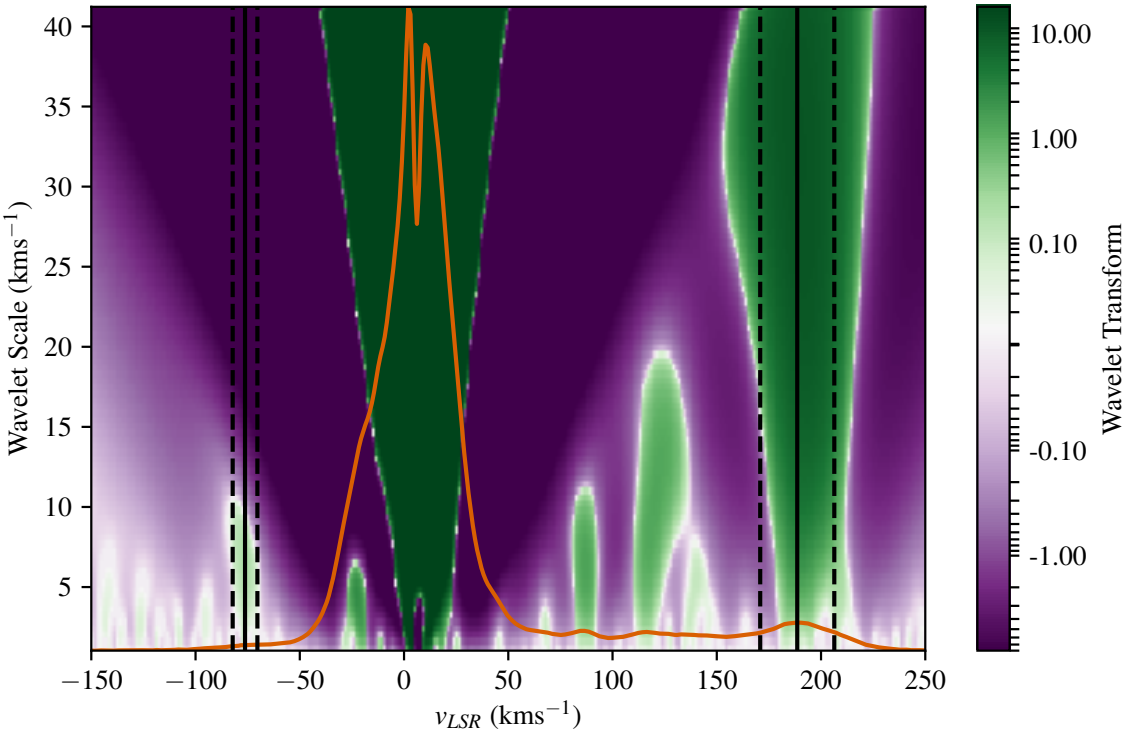

Fig. 2.6 Wavelet transformation matrix of the 21cm brightness temperature profile for $l, b = 5.5, 0.0$. Green lobes signify peaks in the brightness profile, the greater the vertical extent of the lobe, the broader the peak in the brightness profile. The vertical black lines indicate the significant peaks which have the smallest and largest radial velocities. The black dashed lines show the 2σ levels for the width of the emission peaks, determined from the wavelet scale with the maximal wavelet transform within the corresponding lobe.

The wavelet transform for two lines of sight in HI 21cm survey and the 2.6mm CO survey are shown in Fig. 2.6 and Fig. 2.7 respectively. The green lobes indicate local maxima in the wavelet transform, which correspond the the peaks in the line profile, shown in orange. Vertical black lines show the locations of the minimum and maximum radial velocity peaks, where the dotted lines mark the 2σ width of the line. On the l-v diagrams (Fig. 2.8 and Fig. 2.9), the radial velocity extrema follows the outer envelope of emission. The wavelet transform method has successfully identified the peaks at the extreme ends of the profile.

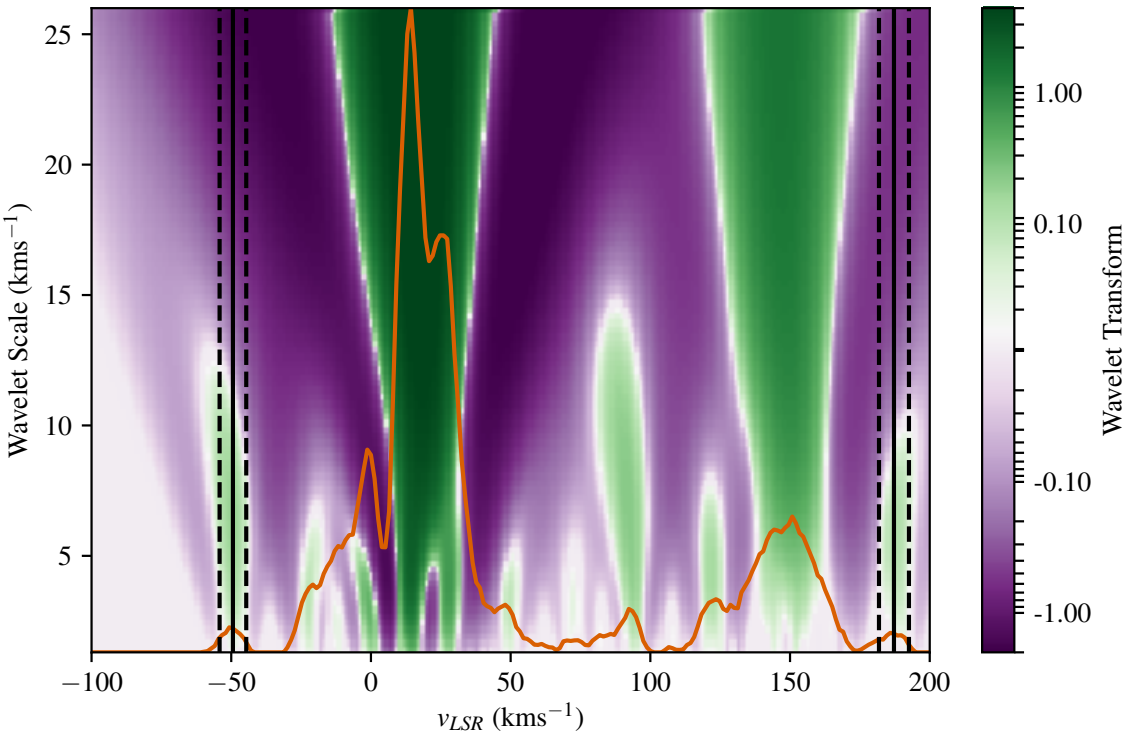

Fig. 2.7 Wavelet transformation matrix of the CO 2.6mm brightness temperature profile for $l, b = 7.5, 0.0$. Green lobes signify peaks in the brightness profile, the greater vertical extent of the green lobe, the broader the peak. The vertical black lines indicate the significant peaks which have the smallest and largest radial velocities, representing the terminal velocities. The black dashed lines show the 2σ levels for the width of the emission peaks, determined from the wavelet scale with the maximal wavelet transform within the corresponding lobe.

A significant asymmetry between the terminal velocity curve for positive and negative longitude is visible in both the 21cm and 2.6mm in Fig. 2.10. The predicted curve fits well at all positive longitudes, especially in the 21cm diagram, but tends to underestimate at negative longitudes. The positive longitudes should fit better as the rotation curve of Clemens, 1985 was fit in the range $13.44 < l < 85.95$. It is clear that a simple tangent point method assuming circular orbits will not be able to accurately describe the rotation curve at $|l| < 10$.

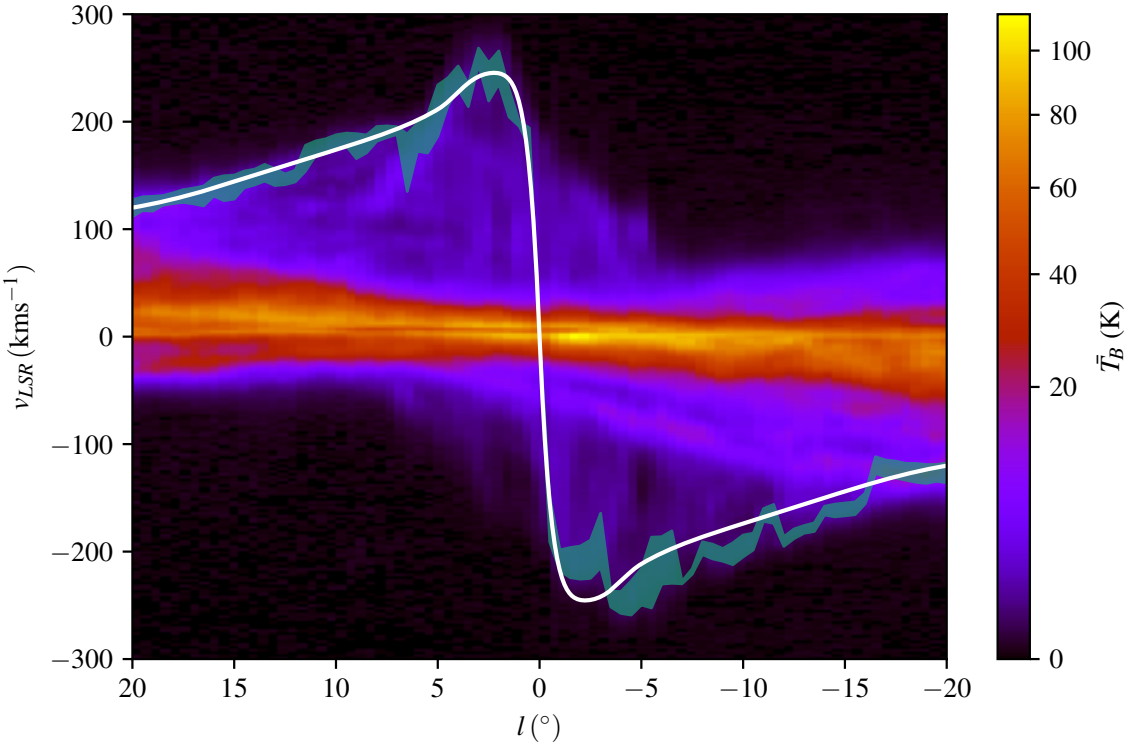

Fig. 2.8 $l - v$ diagram for the average 21cm T_B at $|b| < 4$. Shown in green is the 2σ terminal velocity bounds from the wavelet analysis, which agrees fairly well with the expected terminal velocity from the rotation curve of Clemens, 1985 (white line)

2.7 *Fermi* Analysis of the Galactic Centre Excess

We examined ~ 7 years of Fermi-LAT (Atwood et al., 2009) data (August 4, 2008-September 4, 2015) selecting PASS 8 ULTRACLEANVETO class events. The data was extracted from a square region of $15° \times 15°$ centred at Galactic coordinates $(l, b) = (0, 0)$ and made no distinction between Front and Back events. Furthermore, we restricted our analysis to the 667 MeV to 158 GeV energy range and used the P8R2-ULTRACLEANVETO-V6 instrument response functions. To avoid contamination from terrestrial gamma rays, we used events with zenith angles smaller than 90°. This work made use of the Fermi Science Tools `10r0p5` software package. Employing the `gtmktime` tool we selected the recommended data filters (DATA − QUAL > 0)&&(LAT − CONFIG == 1). Spatial binning was performed with the `gtbin` utility with which we divided the LAT data into 150×150 angular bins of size 0.1°in a CAR sky projection.

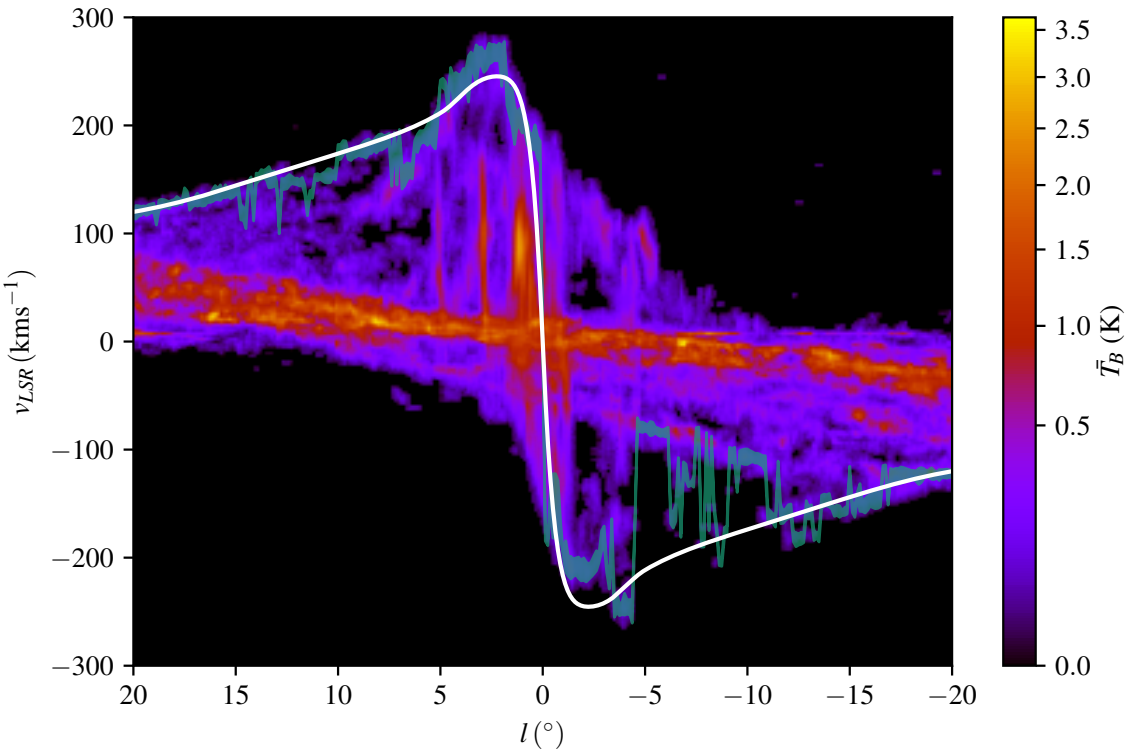

Fig. 2.9 $l - v$ diagram for the average 2.6mm T_B at $|b| < 4$. Shown in green is the 2σ terminal velocity bounds from the wavelet analysis, which agrees fairly well with the expected terminal velocity from the rotation curve of Clemens, 1985 (white line). There is a lack of expected emission between $-10 < l < -5$.

2.7.1 Diffuse Emission Templates

The Galactic diffuse gamma rays resulting from the interaction of cosmic-ray electrons and protons with the interstellar gas and radiation field were modelled with a similar method used for the standard Galactic diffuse emission model(Acero et al., 2016). We fitted a linear combination of atomic and molecular hydrogen gas templates (2.5 and Fig. 2.11), an inverse Compton (IC) energy-dependent spatial template as obtained with GALPROP30, specialized templates for the Sun and the Moon, an isotropic component (`iso-P8R2-ULTRACLEANVETO-V6-v06.txt`), and a model for the gamma ray emission associated with Loop I (See (Macias et al., 2018) Supplementary Fig. 4). The atomic and molecular hydrogen gas column densities were each distributed within four Galactocentric annuli to account for the non-uniform cosmic-ray flux in the Galaxy. The construction of these templates is described in Sec. 2.3 and Sec. 2.4.

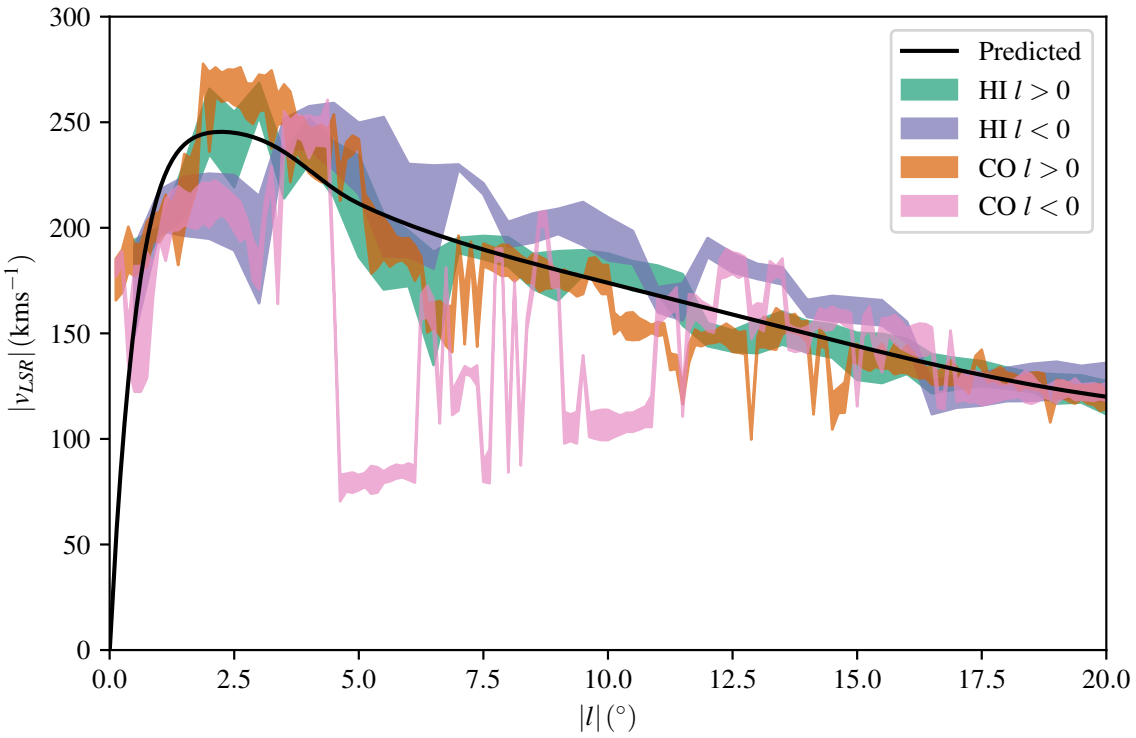

Fig. 2.10 Comparison of the terminal velocity curves for the 21cm and 2.6mm emission to the predicted Clemens, 1985 curve. The independent surveys agree well, except where the 2.6mm does not contain any significant emission near the expected radial velocity at $-11 < l < -5$. The slight longitudinal asymmetry is also visible at $|l| \sim 2$, where the positive longitude lines are on or above predicted curve, and the negative longitudes are definitely below the predicted, in both the HI and CO.

2.7.2 Bin-by-Bin Analysis

Similar to other works (Ackermann et al., 2017; Ajello et al., 2016), we employed a bin-by-bin analysis technique, in which we split the Fermi-LAT data into 19 logarithmically spaced energy bins. Within each energy bin we performed a separate maximum-likelihood fit (Acero et al., 2015) `pyLikelihood` analysis tool. The bin size was chosen to be larger than the LAT energy resolution, but narrow enough that the Galactic emission spectral components can be simply approximated by a power law model. We note that this bin-by-bin method enables us to evaluate the likelihood for a test source with an arbitrary spectral model and significantly reduces the CPU power required to reach convergence as only the flux normalization of the sources are free to vary during the fits. Once the bin-by-bin method had converged, the inferred spectrum of each source was either fitted by a power law or an exponential cut-off model.

2.7.3 Comparing Hydrodynamic and Interpolated Gas Templates

Initially we fit the LAT data with a model comprised of the 3FGL point sources present in our region of interest plus four other spatially extended sources (HESS J1825-137, RX J1713.7-3946, W28 and W30) reported in the 3FGL (Acero et al., 2015). The spatial templates used to model these extended sources correspond to Version 14. To identify the most suitable gas templates for our study, we performed a scan in which we evaluated the improvement of the likelihood fit to the region of interest when the gas maps used were the ones created with the interpolation method (Sec. 2.3 and Sec. 2.4) or the hydrodynamical method (Pohl et al., 2008) . Fig. 2.12 shows that the data preferred the hydrodynamical method. During optimisation, the flux normalisation of the 3FGL sources were left free in each energy bin. We also simultaneously fit the 13 diffuse components' (HI annuli, CO annuli, dust templates, Loop I, inverse Compton, and isotropic) normalisation but kept the Sun and Moon fluxes fixed to their nominal values.

2.7.4 Additional Extended Emission Templates

We also consider the gamma ray emission from the following additional extended sources:

- Boxy Bulge: We assumed the triaxial model for the Galactic bulge derived in Freudenreich, 1998. This was obtained by fitting to COBE/DIRBE near-infrared (1.25 - 4.9 µm) data. We adopted the best-fitting model in that reference, which is Model S. This consists on a sech^2 function on the bar radial spatial profile (top panel of Fig. 2.13).

- Nuclear Bulge: We used a map constructed from a near-infrared stellar density measurement of the central region of our Galaxy ($|l| \geq 3^\circ$ and $|b| \geq 1^\circ$) and subtracted a best fit Galactic disk component (Nishiyama et al., 2013). In order to remove artificial sharp boundaries in the map induced by survey patches, all pixels below 15 stars/arcmin^2 were set to zero. The resulting template is displayed in the middle panel of Fig. 2.13.

- Dark Matter: We modelled the potential annihilating dark matter signal in the Galactic centre as the square of an Navarro-Frenk-White (NFW) density profile

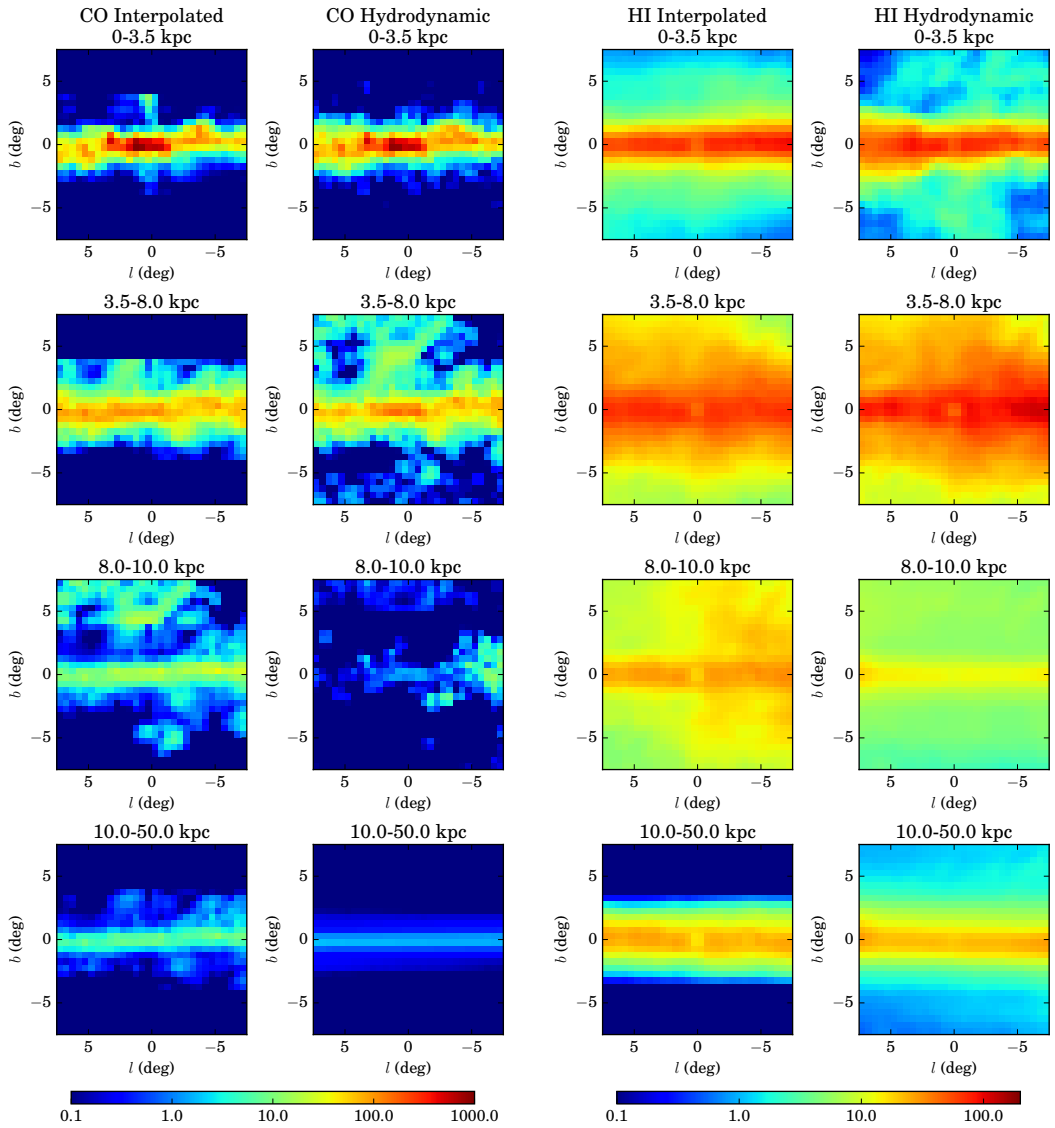

Fig. 2.11 Comparison between the interpolated and hydrodynamic methods. The minimum and maximum radii of each annulus is listed. The units for the H_2 proportional CO maps are K·km/s. The units for the HI maps are $10^{20}\mathrm{cm}^{-2}$.

with an inner slope of 1.2, which had been shown to describe the GCE well in previous works (Hooper et al., 2011b; Abazajian et al., 2014; Daylan et al., 2016). The square of an NFW density profile is representative of a tentative annihilating dark matter signal in the Galactic centre. The resulting template is displayed in the bottom panel of Fig. 2.13

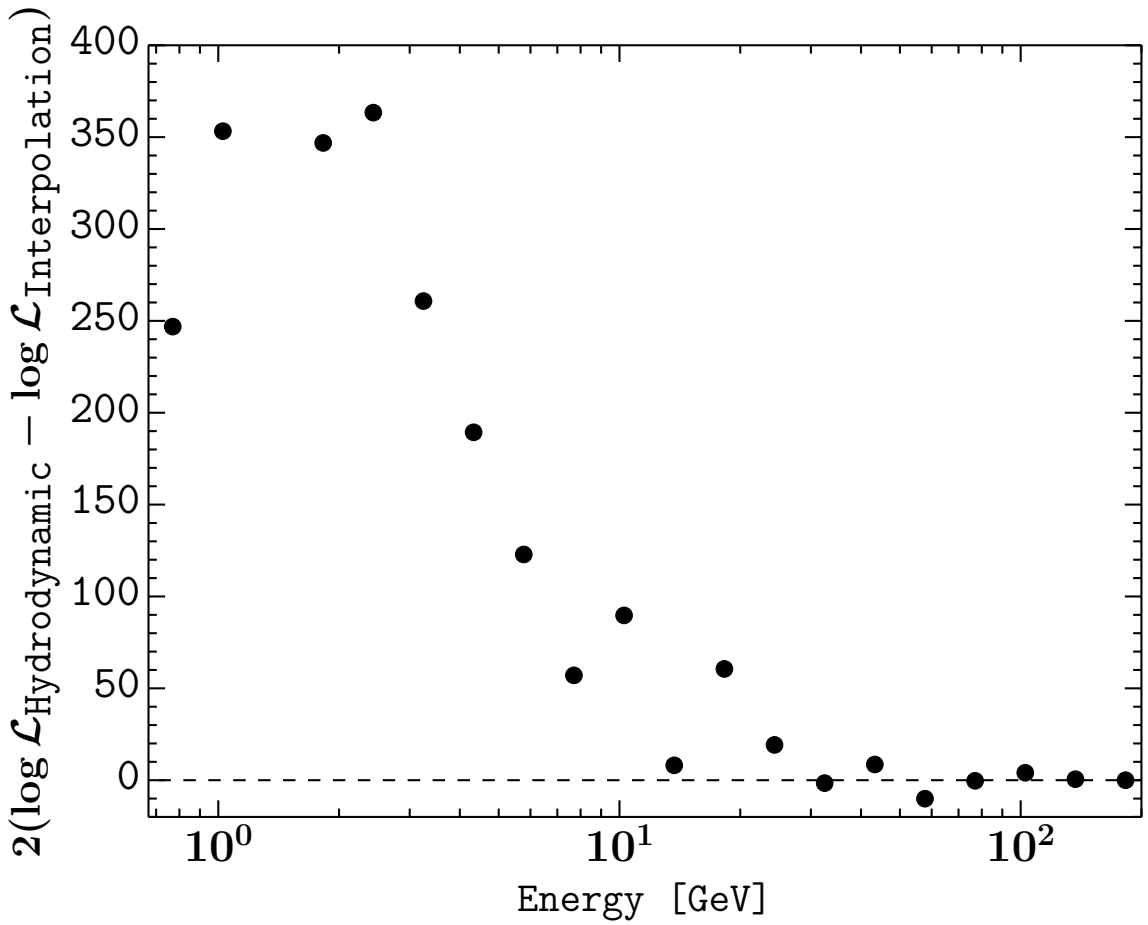

Fig. 2.12 Comparison of the log-likelihood obtained for two different interstellar gas models. The likelihood is compared for hydrodynamic(Pohl et al., 2008) gas maps vs the interpolation maps from Sec. 2.3 and 2.4. Summing over the energy bins gives $\mathrm{TS}_{\mathrm{Hydrodynamic}} = 2 \times 1362$.

- Fermi Bubbles: As found by Acero et al., 2016, we use two catenary curves of the form $10.5^\circ \times (\cosh((l - 1^\circ)/10.5^\circ) - 1^\circ)$ and $8.7^\circ \times (\cosh((l + 1.7^\circ)/8.7^\circ) - 1^\circ)$ for the Northern and the Southern bubbles, respectively.

2.7.5 Results

We fitted the gamma ray emission with our bin-by-bin method to derive fluxes that are independent of the choice of spectral model. Within each bin, the spectrum of the included point and extended sources were modelled as power laws with fixed spectral index of two. Due to the small size of the bins, our results were not sensitive to the

precise spectral index used. In each energy bin, the amplitudes of all included point sources and all included extended templates were simultaneously fit. This allowed us to effectively marginalise over the statistical uncertainties. Table 1 shows the steps we took to evaluate whether a template was significantly detected. We started with the baseline model and then evaluated the TS of each new template. We then added the template with the highest TS to our model and repeated the procedure with this appended to the Base model. We iterated through these steps until the highest TS-value of a new template was below our 4σ threshold. For each new template there are n $\times$ 19 new parameters, where n is an integer. For one new template being considered (i.e. 19 new parameters), our 4σ detection threshold corresponded to $TS \geq 38.4$ (See Macias et al., 2018 for full details).

Table 2.1 Summary of the Likelihood analysis results

Base	Source	$\log(\mathcal{L}_{\rm Base})$	$\log(\mathcal{L}_{\rm Base+Source})$	$\rm TS_{Source}$	σ	Number of source parameters
baseline	FB	-172461.4	-172422.3	78	6.9	19
baseline	NFW-s	-172461.4	-172265.3	392	18.4	19
baseline	Boxy bulge	-172461.4	-172238.7	445	19.7	19
baseline	NFW	-172461.4	-172167.9	587	23.0	19
baseline	NB	-172461.4	-171991.8	939	29.5	19
baseline	NP	-172461.4	-169804.1	5315	55.7	64 × 19
baseline+NP	FB	-169804.1	-169773.6	61	5.8	19
baseline+NP	NB	-169804.1	-169697.2	214	13.0	19
baseline+NP	Boxy bulge	-169804.1	-169663.7	281	15.3	19
baseline+NP	NFW	-169804.1	-169623.3	362	17.6	19
baseline+NP+NB	Boxy bulge	-169697.2	-169566.0	262	14.6	19
baseline+NP+Boxy bulge+NB	NFW	-169566.0	-169553.3	25	2.7	19

The *baseline* model consists of all 3FGL point sources in the region of interest, Loop I, an IC template predicted by GALPROP, the hydrodynamic based gas maps, the recommended isotropic emission map, and a model for the Sun and the Moon. Other model templates considered are: the 64 new point sources (NP), the square of a generalised NFW profile with an inner slope $\gamma = 1.2$ or the square of a "standard NFW" (NFW-s) with inner slope $\gamma = 1$, an infrared Boxy bulge template tracing old stars in the Galactic bulge, a nuclear bulge (NB) template and a template accounting for the Fermi Bubbles (FB). The maximized likelihoods ($\mathcal{L}$) are given for the Base and Base+Source models and the significance of the new source is given by $\rm TS_{Source} \equiv 2(\log(\mathcal{L}_{Base+Source}) - \log(\mathcal{L}_{Base}))$. Note that for both likelihoods all parameters are maximized and so the $\mathcal{L}_{\rm Base+Source}$ will have additional parameters whose number is given in the last column of the table. The conversion between $\rm TS_{Source}$ and σ is discussed in Macias et al., 2018 Methods Section.

Best-fit spectral parameters were found using χ^2 fitting to the inferred flux points for the energy bins. Relative to a power-law spectrum, the preferred spectral model (at 3.5σ and 5.1σ respectively) for both the boxy-bulge and nuclear bulge templates was a power law with an exponential cut-off ($dN/dE \propto E^{-\Gamma} \exp(-E/E_{\rm cut})$, where N is the photon flux). The boxy-bulge had a spectral slope of $\Gamma = 1.9 \pm 0.1$, an energy cut-off $E_{\rm cut} = 10 \pm 5$ GeV and a luminosity $L = (4.5 \pm 0.3) \times 10^{36}$ erg/s for $E \geq 100$ MeV. Similarly, the fit for the nuclear bulge yielded $\Gamma = 1.9 \pm 0.1$, $E_{\rm cut} = 13 \pm 4$ GeV and $L = (3.3 \pm 0.3) \times 10^{36}$ erg/s.

2.8 Discussion

The 21cm emission line profiles in Fig. 2.1 show thermal broadening of the emission lines, caused by turbulent motion within the gas clouds. Thermal broadening of the 21cm emission profile is also seen in the wavelet transform in Fig. 2.6, where the green lobes extend higher than the wavelet transform for the 2.6mm emission in Fig. 2.7. This line broadening effectively lowers the maximum spatial resolution available when using Doppler methods to reconstruct the gas distribution. Clouds of gas appear to be stretched along the line-of-sight, in so called "finger-to-the-sun" artefacts (Nakanishi et al., 2003), even when non-circular motion is accounted for with hydrodynamical models (Pohl et al., 2008). This effect is minimised in our application as we have used broad annular regions to describe the 3-D distribution of the ISM.

Based on the likelihood ratios in Fig. 2.12, the hydrodynamic gas maps provide a significantly improved fit to the diffuse gamma ray data compared to the interpolated gas maps produced in Sec. 2.3 and Sec. 2.4. Hydrodynamical modelling of the gas accounts for the non-circular orbits of gas in the bar, which gives a more accurate reconstruction of the gas density in the inner galaxy. This view was hinted at in the wavelet analysis in Sec. 2.6, which found that the terminal velocity curve in the inner galaxy is not symmetric in galactic longitude, consistent with other studies in the literature (Chemin et al., 2015).

Many analyses in the past considering the millisecond pulsar interpretation had assumed that the population was spherically distributed, to match the profile of the observed GCE (Abazajian et al., 2012; Gordon et al., 2013; Abazajian, 2011; Yuan et al., 2014). In this analysis we have shown that the inclusion of a boxy stellar bulge component representing an unresolved population of millisecond pulsars is significantly preferred by the data over a NFW dark matter profile. Including a boxy bulge also ruled out the detection of a signal associated with an NFW dark matter profile, with the dark matter signal having only a 2.7σ significance. An exponential cut-off spectrum for the fitted boxy-bulge and nuclear bulge with $\Gamma = 2.0$ and $E_{cut} = 13$ GeV were also consistent with previous observations of the GCE (e.g Macias et al., 2014), further supporting the millisecond pulsar explanation. Our results have been confirmed by Bartels et al., 2018, who find the boxy bulge is preferred over an X-shaped bulge when a larger area of the sky is examined.

2.9 Conclusions

We analysed ~ 7 years of GeV gamma ray observations from the inner $15^\circ \times 15^\circ$ of the galaxy using the *Fermi*-LAT. New hydrodynamical maps for the ISM provided a better model for the diffuse galactic background compared to the standard interpolated gas maps recommended for use in point source analyses. These findings are consistent with the flawed rotation curves in the inner region of the Milky Way assuming circular orbits and using the tangent point method.

Including a diffuse emission template with a morphology matching a boxy bulge was significantly preferred by the gamma ray data over a NFW dark matter like morphology. Spectral properties of the fitted templates are consistent with previous studies of a millisecond pulsar population as an explanation of the GCE. From these considerations, the favoured explanation of the GCE is an unresolved population of millisecond pulsars, with a distribution in the inner galaxy consistent with the stellar component of the Galactic bulge.

Following the success of including the boxy bulge template in our gamma ray analysis, in the next Chapter we look into improving the bulge stellar template using red clump stars in the Vista Variables in Via Lactea survey.

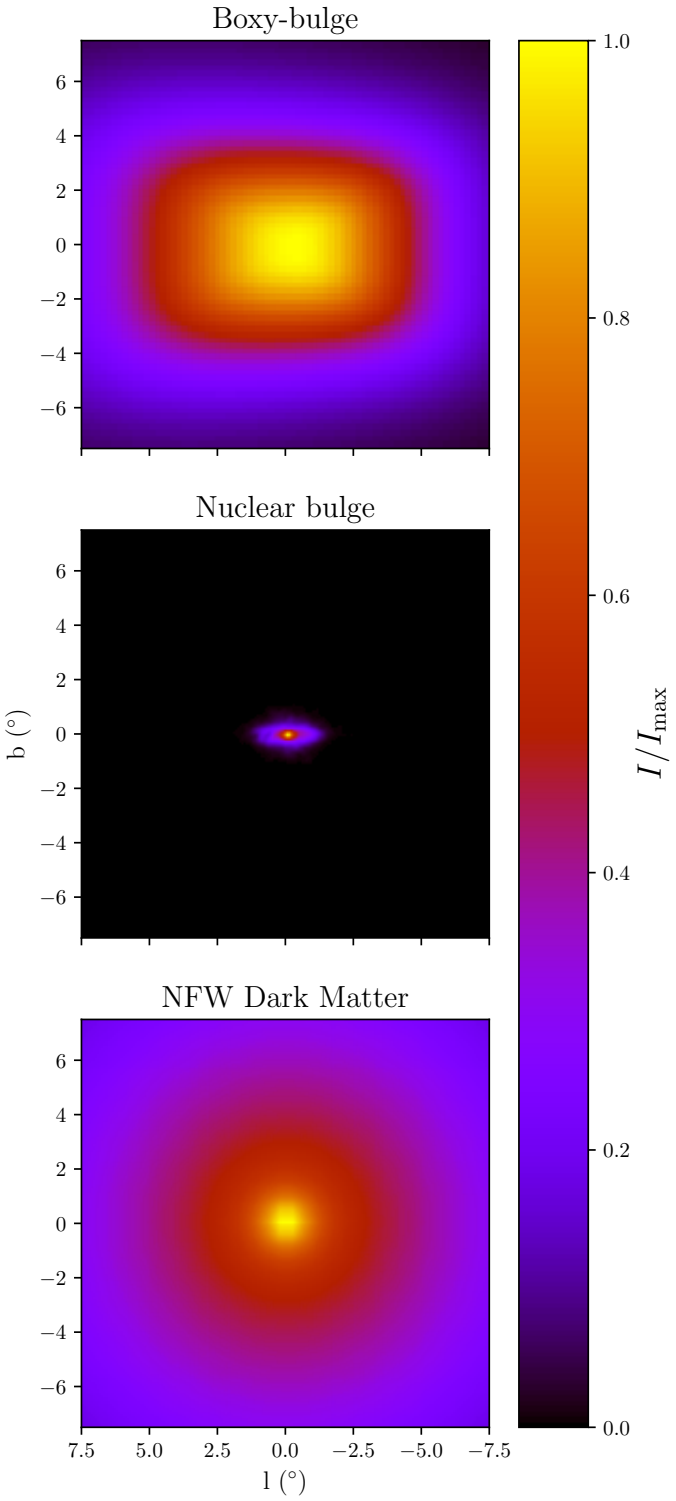

Fig. 2.13 Comparison of the stellar component templates with the NFW dark matter template. Each template contributes a morphologically distinct component to the GCE. Note that the baryon/dark matter ratio in the inner Milky Way rules out a strictly NFW dark matter profile (see Fig. 17 in Bland-Hawthorn et al., 2016)

Chapter 3

Milky Way Bulge Stellar Morphology

3.1 Introduction

Stars in the Milky Way bulge offer astronomers a rare insight into the conditions and scenarios in which bars form in the inner regions of galaxies. Many other galaxies have been observed to contain a bar or bulge, but only the Milky Way can be studied with sufficient precision to discern the positions, motions and chemical compositions of individual stars. Unfortunately, the Sun's position in the disk of the Milky Way means that the bulge is viewed edge on, with a significant amount of intervening dust, gas and stars. Considerable effort goes into overcoming the variety of observational challenges, including but not limited to, extinction and reddening due to dust, source blending and confusion due to significant crowding and deprojection due to our viewing angle. As the technology and techniques improve, a consistent understanding of the composition and formation history of the bulge is becoming apparent. For our application we are mostly concerned with the morphology of the bulge stars.

A significant window through the dusty disk into the bulge was opened with the advent of large scale near infrared surveys. Even though the stars in the bulge were not resolved, the observations with the DIRBE instrument aboard the COBE satellite were able to show that the Galactic bulge is actually a bar (Binney et al., 1991; Weiland et al., 1994). Parametric models fitted to the diffuse emission observed by DIRBE found a triaxial bar that was angled at 10-45° (Dwek et al., 1995; Bissantz et al., 1997; Freudenreich, 1998; Bissantz et al., 2002).

Since the late 1990s, there have been a number of ground based optical or near-infrared surveys with with sufficient precision to individually resolve bulge stars over a reasonable fraction of the bulge e.g OGLE (Udalski et al., 1992), 2MASS (Skrutskie et al., 2006) or Vista Variables in Via Lactea (VVV) (Minniti et al., 2010). A useful feature in the star counts is the red clump (RC), at an apparent magnitude $K_s \sim 13$ for the bulge. RC stars are helium core burning red giant stars, which is a short lived stage of stellar evolution. As a result, most RC stars in the bulge have a similar mass,~ 1 $M_{\odot}$, and thus a similar luminosity (Girardi, 2016), with small intrinsic dispersion from differences in age and metallicity. Since the luminosity function is intrinsically narrow, the apparent magnitude can be used to infer distances for RC stars.

Using observations of the bulge from OGLE, Stanek et al., 1997 were the first to exploit the apparently narrow magnitude distribution of the RC by fitting a parametric model to 12 fields in the bulge. Many of the methods used by Stanek et al., 1997, or variations of them, are still widely used in bulge RC studies. In particular, the luminosity function was modelled as a smooth power-law background with a Gaussian to represent the RC. The fitted parametric models all had bar angles in the range $20-30°$, a significant reduction to the parameter space compared to the COBE/DIRBE era models. Following subsequent data releases from OGLE, these models have been revisited; for OGLE-II (Rattenbury et al., 2007) and OGLE-III (Cao et al., 2013) with similar parametric density models but slightly different models for the luminosity function. The bar angles were found to be in the ranges 24-27° for Rattenbury et al., 2007 and 27-32° in Cao et al., 2013.

Analysis of the RC in OGLE-III (Nataf et al., 2010) and 2MASS (McWilliam et al., 2010) observations found a photometric splitting at $|b| > 5°$. The splitting was interpreted as a physical separation of the RC, into two X-shaped arms, where one arm appears brighter as it is closer to the observer. The X-bulge interpretation was supported by a non-parametric deconvolution of the VVV star counts (Wegg et al., 2013 hereafter WG13). An alternative explanation to the split RC is a secondary peak in the luminosity function from a second population of α enhanced stars. The difference in mean absolute magnitude for the RC compared to an α enhanced RC is predicted to be 0.4 mag (Girardi, 1999). Parallaxes from *Gaia* DR2 combined with VVV photometry has recently shown a difference in absolute magnitude between the clumps similar to the expected 0.4 mag (López-Corredoira et al., 2019), but a multi-population that could also explain the longitudinal variations in the RC requires a classical bulge component (Joo et al., 2017). A direct observation of the X-bulge was

reported in a processed version of the WISE (Wright et al., 2010; Lang, 2014) 3.4 and 4.6 μm observations (Ness et al., 2016). The robustness of the claim has been called into question (Han et al., 2018), though the result itself offers little to explain the split RC.

Other stellar tracers of the bulge density do not clearly exhibit the X-bulge. The young F0-F5 main sequence stars (López-Corredoira, 2016) and Mira variables (López-Corredoira, 2017) disfavour an X-shaped interpretation. While Catchpole et al., 2016 find Mira variables effectively trace either an ellipsoidal bar if younger or spheroid if older. In addition, the study of Y.-W. Lee et al., 2019 looked into differences in sodium content between the proposed chemically different population explanation. They found no interesting kinematic differences between the populations when cross matching with Gaia proper motions as opposed to the distinct kinematics of Sanders et al., 2019 where the results demonstrated a necessary spatial separation.

Studies of metallicity with kinematics such as Babusiaux et al., 2010; Ness et al., 2013 found more metal rich stars tended to follow bar like orbits and metal poor stars following more spheroidal shaped orbits. The notable conflicting conclusion in Vásquez et al., 2013 was later suggested as having been a result of foreground contamination (Rojas-Arriagada et al., 2014; Babusiaux, 2016). Relating to this observation, the morphology of the bulge can depend heavily on the choice of tracer. While the RC traces a more peanut like or x-shaped bulge in the literature, as discussed above, old variable stars RR-Lyrae provide a different picture of the Galactic bulge to RC stars, tracing out a spheroidal shape of the galaxy (Dékány et al., 2013). Young main sequence stars do not exhibit a split clump effect, which may be a different distribution to the RC, contingent on if the RC is a physical separation (López-Corredoira, 2016). However, this young star population may be of negligible impact in this study as the proportion of stars in the bulge younger than 5 Gyr appears to be bounded around 3.4% (Clarkson et al., 2011). This may further constrain the importance of the faint peak in the population scenario of the split RC as those stars are predicted in Girardi, 1999 to be predominantly around 1 Gyr old.

Several works have incorporated kinematic data into their models, refining VVV split clump predictions. By combining Bulge Radial Velocity Assay (BRAVA) measurements with the split RC model of WG13, Portail et al., 2015 further constrains the clump properties such as mass estimates and rotation speeds. This was later adapted to accommodate metallicity variations with ARGOS and APOGEE surveys, obtaining similar conclusions on the barred nature of metal rich populations as prior metallicity

kinematic studies (Portail et al., 2017). In Sanders et al., 2019 and Clarke et al., 2019, VVV stars with proper motions in the RC are given an absolute reference frame through Gaia cross matching. Both find kinematic properties of the peaks in the split clump that necessitate a spatial separation. Recent objections to these kinematic results by Y.-W. Lee et al., 2019 and López-Corredoira et al., 2019 point to the composite bulge model as an explanation while finding discrepancies in the $(l, b) = (0, -8)$ deg field in Fig. 13 of Sanders et al., 2019. Due to likely differences in preparation of their results, in particular the maximally eight fold symmetric frame assumption in symmetrising their model in Sanders et al., 2019, and complications involving the importance of a classical bulge, we avoid ruling on which kinematic characteristics are the most accurate representation of the RC bulge.

Triaxial symmetry (eight fold symmetry) has often been assumed in morphological studies that don't rely on dynamic constraints such as the analytic models in Simion et al., 2017, from here on S17, and non-parametric cases like WG13. We develop and apply our fully non-parametric deprojection of the Galactic bulge relying only on choice of luminosity function and algorithmic smoothness regularisation. In applying the principle of maximum entropy for statistical inference (Jaynes, 1957a; Jaynes, 1957b) we aim to provide an estimate of the bulge density distribution with minimal bias, building on a best fitting eight fold symmetric distribution motivated from previous bar modelling works.

3.2 VVV Data

We used data from the MW-BULGE-PSFPHOT compilation (Surot et al., 2019), an ultra deep, infrared, photometric catalogue of almost 600 million stars in the Milky Way bulge. Included in the catalogue are K_s and J apparent magnitudes from PSF fitting VVV images (Minniti et al., 2010), completeness for most stars from artificial star tests, extinction corrected K_s and J magnitudes, combined photometric + systematic uncertainties for K_s and J, and a variety of quality metrics.

From this catalogue we constructed binned star counts on a $(80 \times 100 \times 75)$ linear grid in extinction corrected magnitude (K_s), Galactic latitude (l), and Galactic longitude (b). The range of the grid was $11 < K_s < 15$, $-10^\circ < l < 10^\circ$, and $-10^\circ < b < 5^\circ$. To select mainly the red giant stars, we excluded sources with $0.4 < J - K_s < 1.0$. A few sources in the catalogue do not have completeness values, as the detectors on which they were observed were excluded from the completeness analysis, so we were unable to

completeness correct our star counts on a star-by-star basis. Instead, we calculated the mean completeness in each (K_s, l, b) voxel. We corrected for completeness by dividing the number count of stars in a voxel by the estimated completeness of that voxel.

The photometry in the MW-BULGE-PSFPHOT compilation was calibrated relative to the Cambridge Astronomical Survey Unit (CASU) aperture photometry catalogues (Saito et al., 2012), which are known to have field-to-field variations in K_s zero-point of up to 0.1 mag. We corrected for this variation in zero-point by adding to the Ks magnitudes, within each tile, the median difference between the 2MASS point source catalogue (Skrutskie et al., 2006) K_s magnitude and the non-extinction-corrected MW-BULGE-PSFPHOT K_s magnitude. We limited the cross matching to sources in 2MASS with $12 < K_s < 13$ to ensure good photometric quality in both source catalogues and used a cross matching threshold of $0.1''$. This limit was used to reduce to effect of crowding and source merging in the 2MASS catalogue (Hajdu et al., 2019). The photometric offsets are shown on the left panel of Fig. 3.1.

Even after extinction correction and completeness correction, some regions on the sky had residual effects in their star counts. We chose to exclude these regions from our analysis by masking where the crowding and extinction is high, using the combined systematic + photometric K_s magnitude error as a proxy. Shown in Fig. 3.1 in the right panel is the mean K_s magnitude error ($\langle\sigma_{K_s}\rangle$) of stars with $12.975 < K_s < 13.025$. The value of the exclusion boundary, $\langle\sigma_{K_s}\rangle = 0.06$, was chosen to visually match the $E(J-K) = 0.9$ boundary in the less crowded $|l| > 5°$ region. We can see that in the left panel of Fig. 3.1, the crowding + extinction mask excluded from the analysis nearly all the tiles with a significant positive photometric correction. Pixels that contain globular clusters in the GLOBCLUST (Harris, 2010) globular cluster catalogue were also excluded from the analysis.

3.3 Isochrones, Bulge Metallicity and Luminosity Functions

Previous studies (e.g. WG13 and S17) have produced luminosity functions by fitting a parametric model to simulated populations of stars, with masses randomly drawn from initial mass functions (IMF) and absolute magnitudes assigned by interpolation of mass-absolute magnitude relations from isochrones. In this framework, the absolute magnitude and mass are treated as random variables, where the luminosity function is

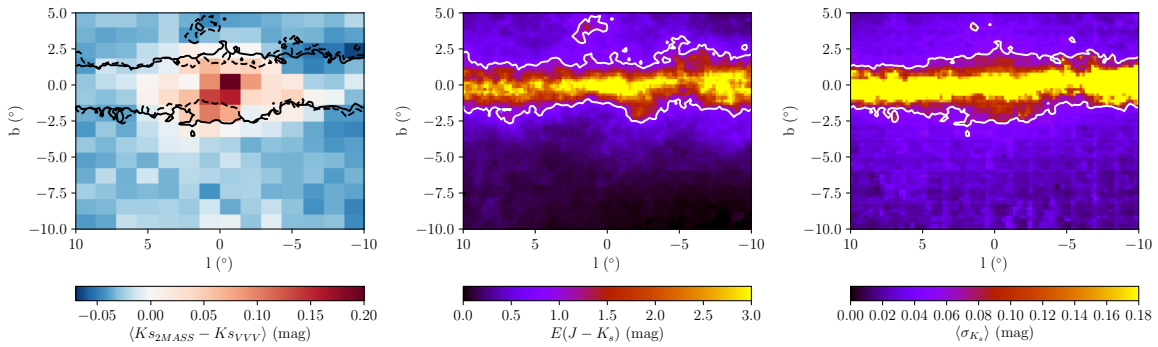

Fig. 3.1 *Left:* Median difference in K_s between cross matched 2MASS and VVV sources. We used this difference to correct the photometric zero-point within each tile. The solid line is the $\langle \sigma_{K_s} \rangle = 0.06$ mask boundary and the dashed line is the $E(J-K_s) = 0.9$ mask boundary. *Middle:* Colour excess used in the extinction correcting the MW-BULGE-PSFPHOT photometry. Inside the white boundary, $E(J-K_s) > 0.9$, extinction severely degrades the quality of the VVV photometry. *Right:* Mean over $12.975 < K_s < 13.025$ of the combined photometric and systematic K_s uncertainty from the PSF fitting procedure used in compiling the MW-BULGE-PSFPHOT catalogue. Inside the white boundary, $\langle \sigma_{K_s} \rangle > 0.06$, the photometry is affected by the increased crowding, causing blending and source confusion.

the probability density function of absolute magnitude, and the IMF is the probability density function of mass. Instead of simulating the luminosity function, we adopted a more analytic approach. The luminosity function for a specific age τ and metallicity z is determined by

$$\phi\left(M_{K_s}, z, \tau\right) = \sum_i \xi\left(\theta_i^{-1}\left(M_{K_s}, z, \tau\right)\right) \left| \frac{d\theta_i^{-1}\left(M_{K_s}, z, \tau\right)}{dM_{K_s}} \right|, \tag{3.1}$$

where ξ is the IMF and θ is the mass-absolute magnitude relation

$$M_{K_s} = \theta\left(m, z, \tau\right). \tag{3.2}$$

In mass ranges where θ is not uniquely invertible, the luminosity function is summed over all possible solutions to the inversion of θ. An example of the mass to absolute magnitude relation for a 10 Gyr bulge is shown in Fig. 3.2, where each different colour represents a branch that needs to be inverted separately then summed to produce the final luminosity function as in Eq. (3.2). For a specific example of the non-uniqueness of θ, a star that has an absolute magnitude (θ) of -2.0, could be either a red giant star (green branch) with mass $m \sim 1.055 M_\odot$ or an asymptotic giant branch star (pink branch) with mass $m \sim 1.059 M_\odot$. To get the luminosity function for the full

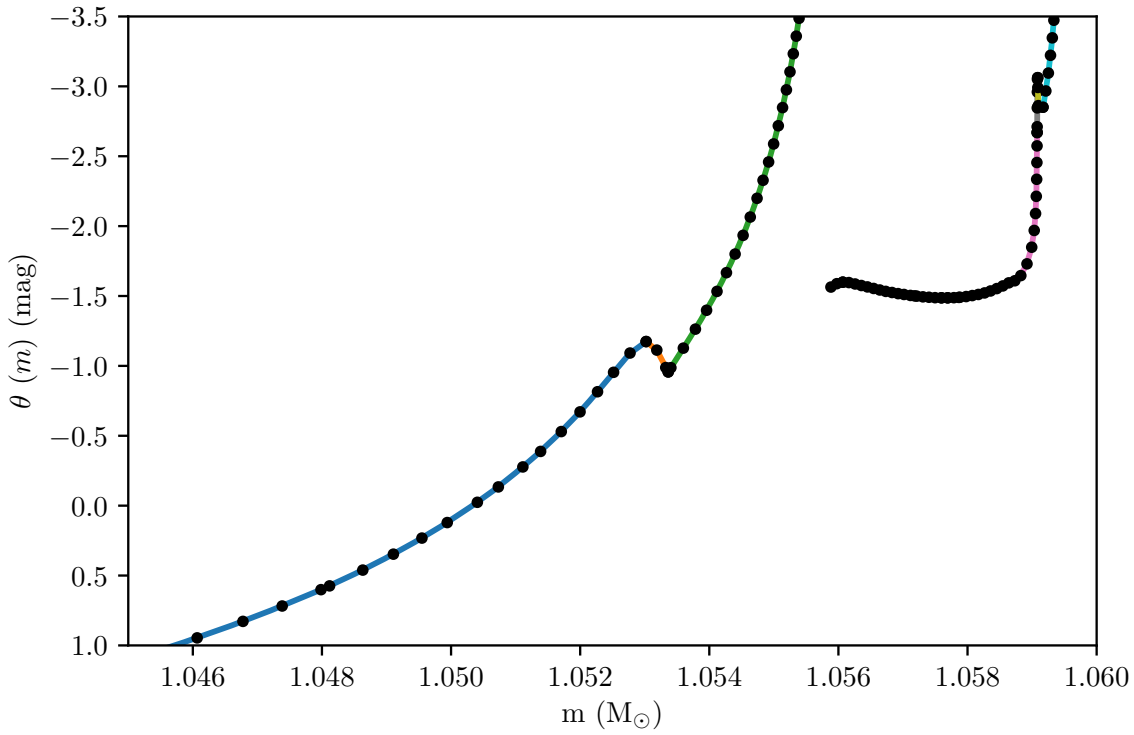

Fig. 3.2 Mass to absolute magnitude relation for the PARSEC+COLIBRI 10 Gyr solar metallicity isochrone. For a single isochrone the values are tabulated at fixed points (black), so we interpolate between them with a linear spline (coloured lines). The different colours represent branches of θ that are uniquely invertible, though θ itself is not (see text for details).

population, we took the expected value of Eq. (3.1)

$$\Phi\left(M_{K_s}\right) = \int_{-\infty}^{\infty}\int_{-\infty}^{\infty} \phi\left(M_{K_s}, z, \tau\right) f\left(z, \tau\right) dz d\tau, \tag{3.3}$$

where f is the metallicity distribution function. We assumed a bulge age of 10 Gyr with metallicity normally distributed with solar mean metallicity $\mu_{[\mathrm{Fe/H}\,]} = 0.0$ and metallicity dispersion $\sigma_{[\mathrm{Fe/H}]} = 0.4$ (Zoccali et al., 2008).

We constructed our bulge luminosity function using mass-absolute magnitude relations from the PARSEC+COLIBRI 10 Gyr isochrone sets Marigo et al., 2017 using 39 metallicity bins linearly spaced in the range -2.279 < [Fe/H] < 0.198. These isochrones are tabulated at fixed mass and metallicity values. The magnitude values between the fixed points were interpolated using a linear univariate spline in mass along a single metallicity isochrone. Attempting to interpolate between evolutionary stages where there are large changes in luminosity, e.g. first ascent red giant to helium core burning giant, introduced artefacts in the resulting luminosity function, so we used the evolutionary stage flags in the isochrones to separate them; 0-3 red giant branch, 4-6 RC and > 6 asymptotic giant branch. Fig. 3.3 shows the luminosity function calculated using Eq. (3.3) with mass-absolute magnitude relations from PARSEC+COLIBRI isochrones and a Chabrier, 2003 log-normal IMF. Fitting a Gaussian to the RC component gave a mean absolute magnitude $\mu_{M_{K_s}} = -1.53$ with standard deviation $\sigma_{RC} = 0.06$ which is consistent with the luminosity function of S17.

Observational effects such as residual extinction and crowding introduce uncertainty in measuring the K_s apparent magnitude, which effectively broadens the observed luminosity function. We accounted for this by convolving our semi-analytic luminosity, described above, with a Gaussian with dispersion σ_{K_s}. As σ_{K_s} was different for each voxel, effectively every voxel had a slightly different luminosity function.

3.4 Deconvolution Method

The RC+RGBB (red giant branch bump) stellar density (ρ) of the Galactic bulge can be reconstructed by inverting the equation of stellar statistics

$$N\left(K_s, l, b\right) = B\left(K_s, l, b\right) + \Delta\Omega\Delta K_s \int_4^{13} \rho\left(s, l, b\right) \Phi\left(K_s - 5\log s - 10\right) s^2 \,\mathrm{d}s, \tag{3.4}$$

where N is the predicted number of stars in a voxel centred at (K_s, l, b) and B is the number of smooth background stars in the voxel that are neither RC or RGBB stars.

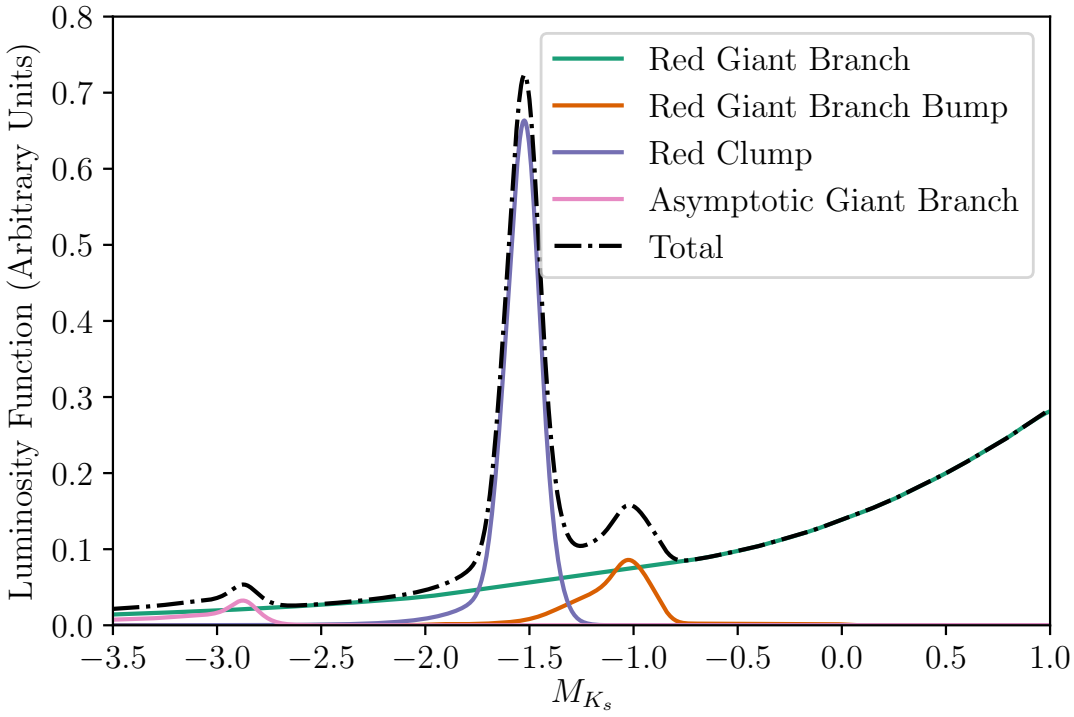

Fig. 3.3 Luminosity function of a 10 Gyr old population with $\langle$[Fe/H]$\rangle$ = 0.0 and $\sigma_{\text{[Fe/H]}} = 0.4$ using PARSEC+COLIBRI isochrones and Chabrier, 2003 log-normal IMF. We convolved the luminosity function by a Gaussian with standard deviation equal to the combined photometric and systematic uncertainty in K_s. For display purposes, the luminosity function, in this figure, was convolved with a Gaussian with $\sigma = 0.05$ which is a typical value for the error in K_s.

The $\Delta\Omega$ denotes the solid angle subtended by the line-of-sight, ΔK_s is the width of the K_s magnitude bin, and s (measured in kpc) is the distance from the Sun. The luminosity function, Φ, is the sum of the bulge RC and bulge RGBB luminosity function components. Note that as the RGBB is a much smaller component than the RC, we sometimes refer to our obtained density in terms of the RC only, but more precisely it does contain both the RC and RGBB. As the Galactic bulge density tends to become negligible beyond several kpc, we only integrate the range 4 kpc $\leq s \leq$ 13 kpc when computing the bulge contribution in modelling stellar counts.

Our analysis uses penalised likelihoods with penalties, which come in two general forms: the first is maximum entropy regularisation, which is defined for a field q,

$$-2\ln\mathcal{L}_{MEM} = 2\lambda\sum_{i,j,k}\left(1 - q_{i,j,k} + q_{i,j,k}\ln q_{i,j,k}\right) \tag{3.5}$$

where i, j, and k are the grid points for K_s, b, and l respectively. The maximum entropy regularisation has a minimum at $q_i = 1$, so for our application, we will use a parameterisation where q is the ratio between a modelled quantity of interest and a smooth prior estimation of the quantity. As shown in Appendix A, the prior relative standard deviation of the reconstructed density from the prior density is of order $1/\sqrt{\lambda}$. So, the larger the value of λ chosen, the smaller the prior uncertainty assumed and so the more regularisation of the solution is applied.

The second form of likelihood penalty we use is the ℓ_2-norm regularisation of the second derivative of the logarithm of some quantity. For a field, F, which varies over one dimension, we use the second order central difference equation approximation of curvature:

$$-2\ln\mathcal{L}_{\text{smooth}} = \eta\sum_{i}\left(\ln F_{i-1} + \ln F_{i+1} - 2\ln F_i\right)^2. \tag{3.6}$$

This penalty has a minimum when F is the exponential of a linear function. As shown in Appendix, the prior relative standard deviation from an exponential of a linear function is approximately $1/\sqrt{6\eta}$. So, the larger the value chosen for η, the more smoothness regularisation is applied.

3.4.1 Background

We modelled the background (B) non-parametrically as a free parameter for each (K_s, l, b) voxel. Without regularisation we would have a Poisson likelihood for data $n_{i,j,k}$ and expected counts $B_{i,j,k}$ where i, j, k are the grid points for (K_s, l, b) respectively.

With maximum entropy and smoothness regularisation, we have the following formula for the natural log of the penalised likelihood ($\mathcal{L}$):

$$\begin{aligned}\ln \mathcal{L} = \sum_{\{i,j,k\}\in\{K_s,l,b\}} \Big[& n_{i,j,k} \ln B_{i,j,k} - B_{i,j,k} \\ & -\lambda \left(1 - q_{i,j,k} + q_{i,j,k} \ln q_{i,j,k}\right) \\ & -\eta_{K_s} \left(\ln B_{i-1,j,k} + \ln B_{i+1,j,k} - 2 \ln B_{i,j,k}\right)^2 /2 \\ & -\eta_{l} \left(\ln B_{i,j-1,k} + \ln B_{i,j+1,k} - 2 \ln B_{i,j,k}\right)^2 /2 \\ & -\eta_{b} \left(\ln B_{i,j,k-1} + \ln B_{i,j,k+1} - 2 \ln B_{i,j,k}\right)^2 /2 \Big] ,\end{aligned} \tag{3.7}$$

where q is the ratio between our background model and a smooth prior estimation of the background:

$$q \equiv \frac{B}{B_{\rm prior}}. \tag{3.8}$$

The first line on the RHS of Eq. 3.7 is from the usual Poisson likelihood distribution. The second line is an entropy regularisation of the form of Eq. 3.5 and the third, fourth, and fifth lines are smoothness regularisations of the form given in Eq. 3.6 for K_s, l, and b respectively. The regularisation parameter values we used are listed in Table 3.6 and we discuss their choice in Section 3.5. We maximised Eq. 3.7 using the magnitude ranges $11 < K_s < 11.7$ and $14.3 < K_s < 15$, see Section 3.5 for more details. This means the behaviour in $11.7 \leq K_s \leq 14.3$ is determined entirely by the prior, maximum entropy, and smoothness regularisation.

The background is mainly composed of red giant stars in the bulge and foreground disc stars, so for the prior background ($B_{\rm prior}$) we used the S-model fitted by S17 with the RC and RGBB components subtracted. Only the asymptotic giant branch and red giant branch (excluding the RGBB) components of the semi-analytic luminosity function are used for the bulge component in determining the background. Included in the S-model are thin and thick disc components of the Besançon galaxy model of Robin et al., 2003, where we have used the updated thin disc parameters from Robin et al., 2012 and the updated thick disc parameters from Robin et al., 2014. The S-model of S17 was fitted to aperture photometry of the VVV DR2 data in the range $12 < K_s < 14$, so the background was underestimated for some lines-of-sight. To compensate for this, we multiplied each pixel (line-of-sight) of the prior background by a constant, so that its mean matched the mean of our data in the range $11 < K_s < 11.5$ mag.

Initial tests of our deconvolution method on the VVV data showed that our method was finding a feature in the density consistent with the structure behind the bar

reported in Gonzalez et al., 2018. As we are trying to determine the bulge component, we decided to add this feature to our background, by first estimating our density using our maximum entropy background, then adding the star counts associated with any density significantly greater than the SX parametric density (see Section 3.4.3) to the maximum entropy background. We considered any density that was beyond the limits

$$\begin{aligned} s &> 10 \text{ kpc} & l &\geq 0^\circ \\ s &> 10 - 0.1818\, l \text{ kpc} & l &< 0^\circ \end{aligned} \tag{3.9}$$

and at least 2.6×10^{-5} stars pc^{-3} sr^{-1} above the parametric model density to be part of the structure behind bar. Displayed in Fig. 3.4 is the density summed over $|\mathrm{b}| < 10^\circ$, where the feature behind the bar is visible in the model fitted using our maximum entropy method. The contribution of the feature behind the bar to the background is visible in the bottom panel of Fig. 3.5 as a bump in the fitted background at $K_s \sim$13.8 mag. When using the updated background, the feature behind the bar is no longer present in the density, as seen in the right panel of Fig. 3.4.

Shown in the top panel of Fig. 3.5 is the fitted background for a $1^\circ \times 1^\circ$ box around $(l, b) = (0.9^\circ, -6.1^\circ)$, where we can see that the fitted background is only slightly deviating from the prior background. In the bottom panel, the background fitted in a $1^\circ \times 1^\circ$ box around $(l, b) = (0.9^\circ, 3.1^\circ)$ fits the data well in the shaded regions. However, the background needs to deviate significantly from the prior background at $K_s > 14.7$ mag, where the data may have residual extinction and completeness issues. In the unshaded region, apart from the added feature behind the bar, the background closely follows the shape of the prior solution. The background also smoothly trends back to passing through the data in the shaded regions.

3.4.2 Maximum Entropy Deconvolution

Maximum entropy methods (MEMs) have been used in applications such as image reconstruction in radio interferometry (Cornwell et al., 1985) and also in foreground/background modelling of diffuse emission processes, e.g. cosmic microwave background studies with WMAP (Bennett et al., 2003) or diffuse gamma ray studies with Fermi-LAT (Storm et al., 2017).

Our maximum entropy method constructs a model for predicting the binned star counts, using a non-parametric description of the density. It maximises the penalised

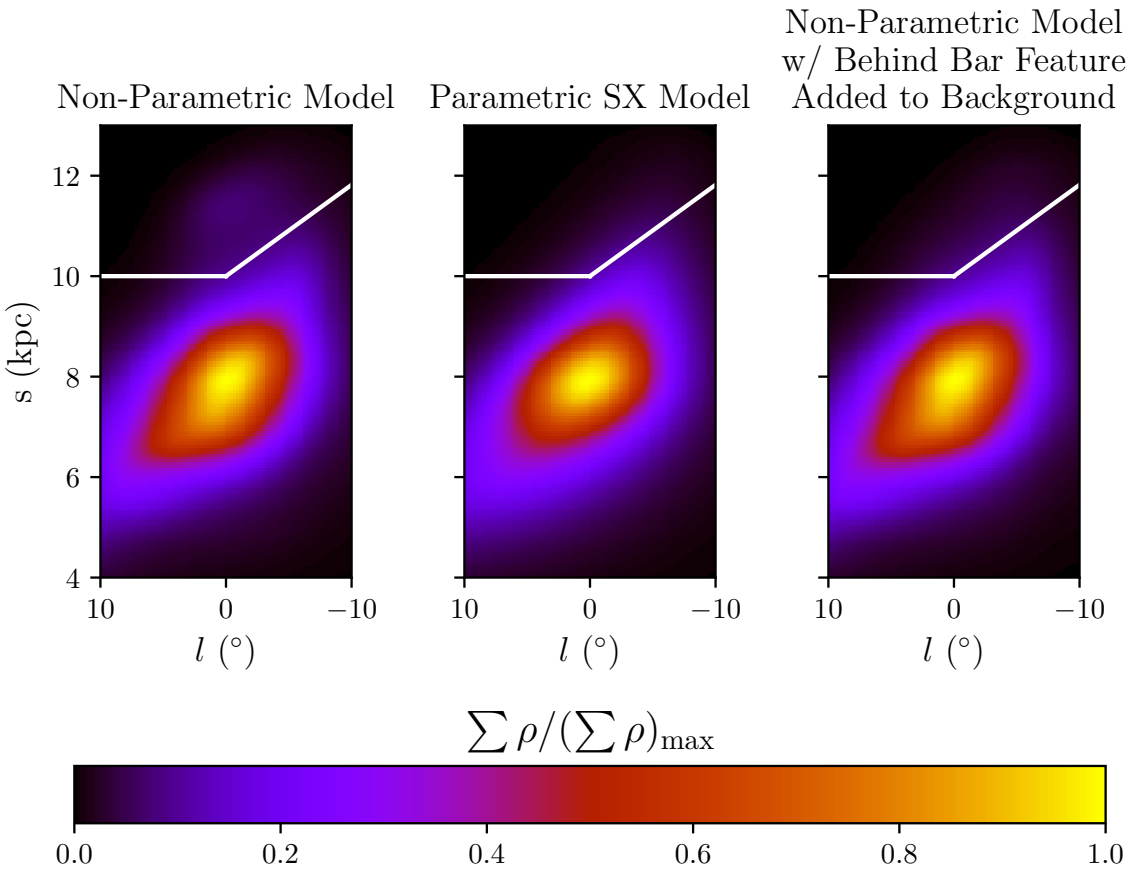

Fig. 3.4 Apparent structure behind the bar in the VVV data, visible in the left panel, was added to the background of our model. We remove any density that is significantly greater than the fitted parametric model (middle panel) and at distances greater than indicated by the white line. In these figures, the density has been summed in the range $|b| < 10°$.

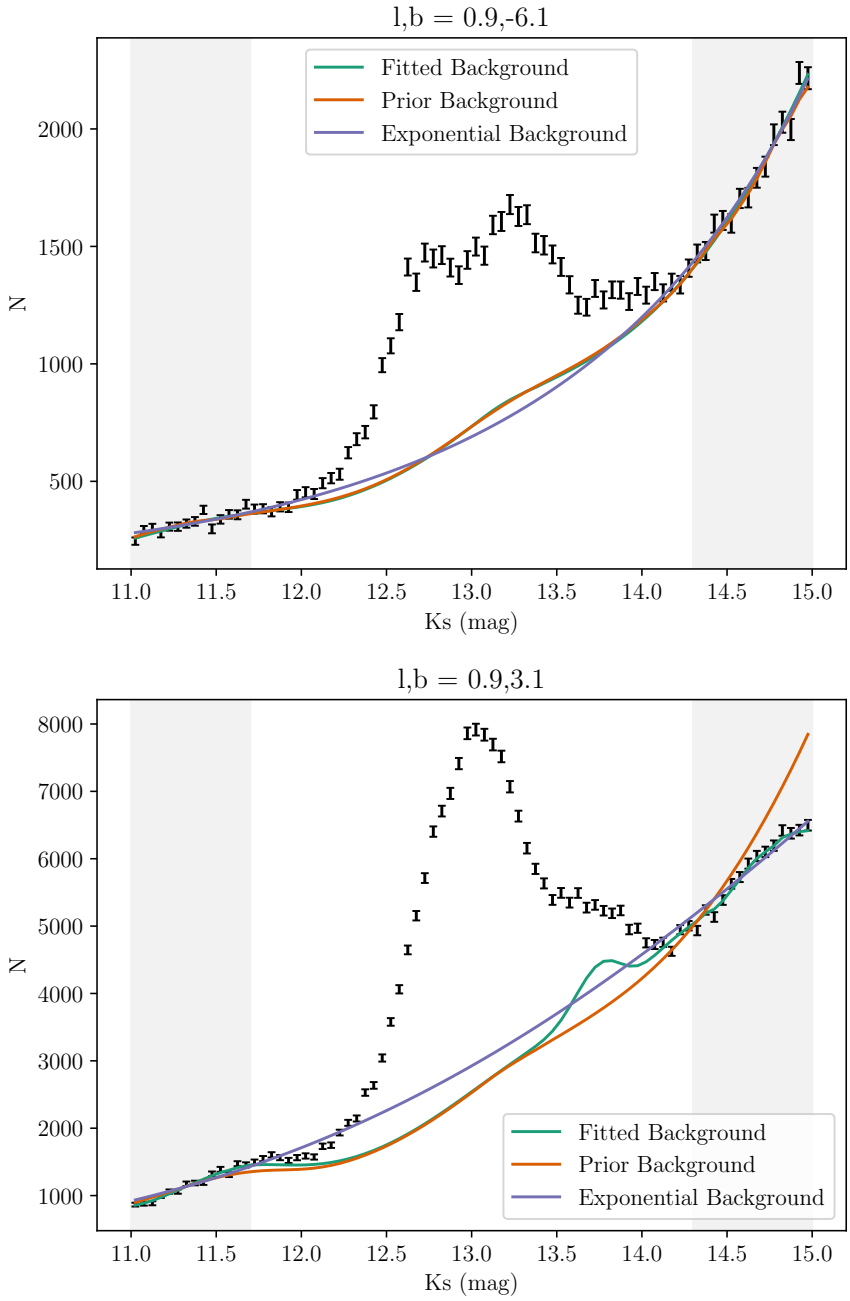

Fig. 3.5 Demonstration of the maximum entropy background fitting in two $1^\circ \times 1^\circ$ regions. The background has been fitted in the grey shaded regions using the maximum entropy method. The prior background was calculated using the S17 S-model, which has been scaled to match the VVV observations between $11.0 < K_s < 11.5$ mag. The bump in the bottom panel "fitted background" at $K_s \sim 13.8$ mag is from a feature behind the bar, see text in Subsection 3.4.1 for more details. The exponential background is described in Section 3.7.7.

$\ln \mathcal{L}$

$$\begin{aligned}\ln \mathcal{L} = & \sum_{\{i,j,k\}\in\{K_s,l,b\}} \left(n_{i,j,k} \ln N_{i,j,k} - N_{i,j,k}\right) \\ & - \sum_{\{i,j,k\}\in\{s,l,b\}} \Big[\lambda \left(1 - \kappa_{i,j,k} + \kappa_{i,j,k} \ln \kappa_{i,j,k}\right) \\ & + \eta_s \left(\ln \rho_{i-1,j,k} + \ln \rho_{i+1,j,k} - 2 \ln \rho_{i,j,k}\right)^2 /2 \\ & + \eta_l \left(\ln \rho_{i,j-1,k} + \ln \rho_{i,j+1,k} - 2 \ln \rho_{i,j,k}\right)^2 /2 \\ & + \eta_b \left(\ln \rho_{i,j,k-1} + \ln \rho_{i,j,k+1} - 2 \ln \rho_{i,j,k}\right)^2 /2\Big] ,\end{aligned} \tag{3.10}$$

where the first term on the RHS is the Poisson likelihood with the observed counts, n, and the predicted counts N. The second line has the maximum entropy regularisation term of the form given in Eq. 3.5, where κ is the ratio between the fitted stellar density, ρ, and a prior estimate of the density, $\rho_{\rm prior}$:

$$\kappa \equiv \frac{\rho}{\rho_{\rm prior}}. \tag{3.11}$$

The last three lines of Eq. 3.10 are the smoothness regularisation for the density field, of the form given in Eq. 3.6, in the s, l, and b directions. Including the maximum entropy term in the likelihood discourages the modelled density from over-fitting to regions of the data that are dominated by noise, where it will instead favour the smooth prior density. Addition of the smoothness terms discourages spurious high frequency variations in the modelled density by minimising curvature in the logarithm of the density. The smoothness term also has the added benefit of inpainting the density in lines of sight which have been masked out. We set $\lambda = 0$ in masked regions so as they are only affected by the smoothness term and the values of the model at the edge of the mask.

3.4.3 Parametric Model of the X-Bulge

In light of the X-shape apparent in the eight fold symmetrised WG13 style deconvolution, we consider a closed form parametric base case that allows for a X-bulge perturbation. We characterise its potential pathologies in fitting to data and simulations. The parametric density models fitted in this section are used as prior estimates for the density ($\rho_{\rm prior}$) with the maximum entropy deconvolution in Section 3.6. Our base case parametric-model fit was subsequently applied in a template fitting analysis of the *Fermi* GCE for comparison with our base non-parametric model result (see Section 3.8.2).

We selected the S-model, which proved successful for bulge modelling in Freudenreich, 1998 and S17, as our base distribution. Inspired by the X-bulge parametric form of López-Corredoira, 2016, we perturb the S-model with a X-like shape. We use a right-handed, Galactic Centre origin, Cartesian grid (X, Y, Z) aligned with the bulge axes of symmetry. The coordinates are chosen so that the X-axis lies along the major axis of the bulge and the Z-axis points towards the north Galactic Pole. We refer to the arms of the X-bulge as the X-arms but these are not necessarily aligned with our X coordinate. The perturbation shape was freed in X and Y to accommodate non-circular X-arm shapes. We also allowed the density of the X-arms to trail off as an exponential of a power-law with exponent n rather than assuming an exponential or Gaussian distribution. We label this parametric form the SX model, with its components defined as follows:

$$\rho_{\rm SX}(X,Y,Z) = \rho_0 {\rm sech}^2(r_1) \times [1 + A \times (\exp(-r_2^n) + \exp(-r_3^n))], \tag{3.12}$$

$$r_1^{c_\parallel} = \left[\left(\frac{|X|}{x_0}\right)^{c_\perp} + \left(\frac{|Y|}{y_0}\right)^{c_\perp}\right]^{\frac{c_\parallel}{c_\perp}} + \left(\frac{|Z|}{z_0}\right)^{c_\parallel},$$

$$r_2 = \left[\left(\frac{|X - CZ|}{x_1}\right)^2 + \left(\frac{|Y|}{y_1}\right)^2\right]^{\frac{1}{2}},$$

$$r_3 = \left[\left(\frac{|X + CZ|}{x_1}\right)^2 + \left(\frac{|Y|}{y_1}\right)^2\right]^{\frac{1}{2}}$$

using a generalised ellipsoid distribution for the bulge and a simple ellipsoidal X-shape aligned with the bulge that tapers off with the the same Z distribution. The parameters $\vartheta = (\rho_0, A, n, x_0, y_0, z_0, c_\perp, c_\parallel, x_1, y_1)$ all need to be fit to the data. We anticipate from the near/far density asymmetry visible above and below the Galactic plane in the unsymmetrised WG13 style deconvolution that the X-bulge will still not be accurately accounted for by an eight fold symmetric model, so we used the parametric fit as a prior ($\rho_{\rm prior}$) for the maximum entropy non-parametric fit which did not enforce eight fold symmetry. This will provide us with an intermediary model between the S and non-parametric models in the *Fermi* template fitting analysis to gauge the correlation between an improved VVV fit and an improved gamma ray distribution fit. If the GCE is tracing a bulge and there are no additional unexpected features, we might expect that a model that increasingly traces the morphological features of the bulge will improve the fit.

Investigating the parting rate of the X-arms by fitting a power-law rather than the simple $X \pm CZ$ form, we found the split was still well approximated as a linear function. To avoid convergence issues from excessive parameters, the RC split was left in the linear form.

A tapering of the density at cylindrical radii greater than a cutoff radius, R_c, was applied to the density distribution via $\exp(-2(R - R_c)^2)$ with R_c fixed to 4.5 kpc in all fits, following the preferred choice in S17. We also fit the deviation from an 8kpc distance from the Sun to the Galactic centre so that the new distance is $8\ \mathrm{kpc} + \Delta \mathrm{R}_0$. Additionally, we fitted α which is the angle between the bulge major axis and the line connecting the Sun to the Galactic centre.

We optimise our parametric models for parameter set ϑ using the SCIPY BFGS routine[1], minimising the Poisson likelihood statistic:

$$\ln \mathcal{L} = \sum_{\{i,j,k\} \in \{K_s,l,b\}} (n_{i,j,k} \ln N_{i,j,k} - N_{i,j,k}) + \text{constant} \tag{3.13}$$

where N_i is the corresponding model, obtained by integrating the equation of stellar statistics (Eq. 3.4) for parametric density ρ_{SX}. Our uncertainties are listed in our tables of results (Tables 3.1 and 3.2). They are derived from the corresponding square root of diagonal elements of the inverse Hessian matrix produced by this routine. The SX model fit was initialised by randomly picking a starting point somewhere between qualitatively different boundaries that produce physically possible densities for the X perturbation parameters and choosing the initial S parameters from within 10% of the best fit values from the S-model.

3.4.4 Parametric Systematics

In this section, we will be checking some of the systematics for our parametric fit. To facilitate this we will also check how the systematics affect our fit to simulated data.

We constructed a simulated Milky Way population comprised of a thin disc, thick disc, and a bulge, as is modelled in S17. The thin and thick discs were generated from the updated Besançon model parameters of Robin et al., 2012 and Robin et al., 2014 respectively. The S-bulge model is given by Eq. 3.12 with $A = 0$. The simulation parameters used for this model are listed in Table 3.5. We generated a mock catalogue

[1] https://www.scipy.org/

Table 3.1 Parametric SX and S-models fitted to VVV data used as priors in Table 3.7. The best fits and 68% errors are given for each case on alternating lines. Labels described in the legends of Figures 3.6 and 3.7. The baseline case's $-2\ln\mathcal{L}$, computed using equation 3.13, is -1.36967790×10^8. In column 2 we subtract this value from the $-2\ln\mathcal{L}$ values.

Label	$-2\ln\mathcal{L}$	$c_\perp$	$c_\parallel$	x_0	y_0	z_0	$\rho_0 \times 10^6$	α	ΔR_0	C	A	x_1	y_1	n
A) Base case	0	1.581	2.359	1.853	0.672	0.4605	0.123	20.12	-0.0968	1.386	0.69	0.731	1.090	2.31
		0.008	0.009	0.006	0.001	0.0004	0.002	0.03	0.0009	0.005	0.02	0.004	0.005	0.09
B) No feature behind the bar	17086	1.856	2.319	1.88	0.664	0.4544	0.119	18.0	-0.198	1.359	0.68	0.781	1.11	2.2
incorporated into background		0.007	0.008	0.02	0.002	0.0007	0.003	0.2	0.001	0.004	0.05	0.007	0.02	0.2
C) Exponential background	65507	1.309	3.177	1.641	0.7105	0.4798	0.1158	23.55	-0.0386	1.346	0.6246	0.621	0.734	1.981
instead of MaxEnt background		0.001	0.002	0.001	0.0007	0.0003	0.0001	0.002	0.0005	0.002	0.0009	0.001	0.001	0.001
D) Broad luminosity function	-1793	1.172	2.124	1.735	0.610	0.4658	0.1788	28.88	-0.0711	1.356	2.13	0.170	1.135	18.0
		0.007	0.009	0.008	0.002	0.0007	0.0009	0.06	0.0009	0.003	0.04	0.003	0.008	0.4
E) Metallicity gradient	266	1.546	2.383	1.884	0.6802	0.4582	0.1193	19.863	-0.1127	1.389	0.727	0.729	1.057	2.244
accounted for		0.002	0.002	0.002	0.0003	0.0002	0.0002	0.001	0.0007	0.001	0.001	0.002	0.001	0.002
F) S-model prior	38934	1.677	2.616	1.3812	0.58753	0.42	0.2322	19.7886	-0.0724	-	-	-	-	-
with $Z_\odot = 15$ pc		0.0003	0.0002	0.0002	0.00012	0.0003	0.0004	0.0003	0.0003	-	-	-	-	-
G) S-model prior and Broad luminosity	21665	1.242	2.779	1.2332	0.4819	0.40921	0.3687	31.945	-0.0698	-	-	-	-	-
function with $Z_\odot = 15$ pc		0.001	0.003	0.0013	0.0004	0.00018	0.0005	0.005	0.0008	-	-	-	-	-
H) S-model prior with $Z_\odot = 0$ pc	19723	1.6734	2.592	1.3921	0.5915	0.4271	0.2269	19.8241	-0.0767	-	-	-	-	-
		0.0008	0.003	0.0009	0.0004	0.0002	0.0002	0.0003	0.0008	-	-	-	-	-
I) S-model prior with $Z_\odot = 0$ pc	15107	1.221	2.733	1.253	0.4884	0.41672	0.3596	31.851	-0.0712	-	-	-	-	-
& Broad luminosity function		0.003	0.004	0.0012	0.0004	0.00016	0.0004	0.006	0.0006	-	-	-	-	-
J) Extinction mask	-23656527	0.970	2.691	26.442	0.7440	0.4786	0.004990	18.768	-0.1018	1.302	38.903	0.815	0.891	0.8855
		0.002	0.001	0.002	0.0007	0.0002	0.000005	0.002	0.0006	0.001	0.002	0.001	0.001	0.0009

Table 3.2 Parametric SX and S-models fitted to S-model simulation. The best fits and 68% errors are given for each case on alternating lines. Labels described in the legends of Figures 3.6 and 3.7. The baseline case's $-2\ln\mathcal{L} = -1.41020150 \times 10^8$. In column 2 we subtract this value from the $-2\ln\mathcal{L}$ values.

Label	$-2\ln\mathcal{L}$	$c_\perp$	$c_\parallel$	x_0	y_0	z_0	$\rho_0 \times 10^6$	α	ΔR_0	C	A	x_1	y_1	n
A) Base case	0	1.864	2.464	1.608	0.6851	0.4845	0.1492	19.414	-0.0031	1.8136	0.42	0.0003	0.409	0.022
		0.004	0.003	0.001	0.0006	0.0002	0.0007	0.006	0.0003	0.0006	0.01	0.0002	0.005	0.001
B) No feature behind the bar	733	1.864	2.467	1.600	0.6846	0.4835	0.1897	19.405	-0.0023	1.092	-0.016	0.050	7.538	0.178
incorporated into background		0.003	0.004	0.001	0.0004	0.0002	0.0003	0.003	0.0006	0.003	0.003	0.001	0.005	0.002
C) Exponential background	55654	1.733	2.481	1.545	0.7116	0.4943	0.1932	21.17	0.0638	0.6724	-0.205	0.020	2.10	0.222
instead of MaxEnt background		0.004	0.005	0.002	0.0006	0.0003	0.0007	0.02	0.0004	0.0006	0.006	0.002	0.04	0.007
D) Broad luminosity function	13797	1.893	2.545	1.377	0.6043	0.4785	0.2386	26.90	0.0460	2.659	0.402	0.011	1.954	0.40
		0.008	0.007	0.002	0.0006	0.0004	0.0005	0.03	0.0007	0.002	0.001	0.001	0.007	0.02
E) Metallicity gradient	109	1.852	2.523	1.601	0.6864	0.4843	0.1817	19.10	-0.0178	7.483	0.019	2.779	4.51	8.308
accounted for		0.004	0.005	0.001	0.0005	0.0003	0.0003	0.01	0.0008	0.005	0.001	0.008	0.01	0.006
F) S-model prior	-5523	1.868	2.506	1.586	0.6790	0.4746	0.1930	19.49	-0.0003	-	-	-	-	-
with $Z_\odot = 15$ pc		0.003	0.004	0.001	0.0004	0.0002	0.0002	0.04	0.0007	-	-	-	-	-
G) S-model prior and Broad luminosity	15475	1.9941	2.6591	1.30221	0.56743	0.4640	0.2677	29.2638	0.0548	-	-	-	-	-
function with $Z_\odot = 15$ pc		0.0002	0.0002	0.00008	0.00005	0.0001	0.0002	0.0001	0.0003	-	-	-	-	-
H) S-model prior with $Z_\odot = 0$ pc	640	1.861	2.476	1.599	0.6841	0.4840	0.1886	19.552	-0.0065	-	-	-	-	-
		0.003	0.003	0.001	0.0005	0.0002	0.0002	0.004	0.0006	-	-	-	-	-
I) S-model prior with $Z_\odot = 0$ pc	22740	1.954	2.604	1.3187	0.5733	0.4740	0.2616	29.2719	0.0514	-	-	-	-	-
& Broad luminosity function		0.001	0.002	0.0006	0.0003	0.0002	0.0002	0.0009	0.0006	-	-	-	-	-
J) Extinction mask	-16226836	1.839	2.513	1.582	0.6844	0.4861	0.1851	19.84	-0.0164	6.76	0.041	0.98	2.23	0.82
		0.005	0.006	0.002	0.0006	0.0004	0.0004	0.02	0.0007	0.05	0.003	0.01	0.07	0.03

of stars by drawing a Poisson random value from the binned simulation model. The simulated population is discussed in more detail in Section 3.5.

The normalisations we used for each of the three components have been multiplied by the same constant chosen so that the total number of stars in the unmasked region and in $12 < K_s < 14$ matches the number of stars in the VVV PSF catalogue. The luminosity function we used for the bulge in the simulation is the same as the one we used in our fitting procedure to the VVV data.

We briefly consider some systematic tests of the SX model in simulations and take a provisional look at the results of fitting this model to the VVV data. Systematic tests of the parametric fits to the data are discussed further in Section 3.7. The results of fitting the SX model to data and simulations are listed in Tables 3.1 and 3.2, and are plotted in Figures 3.6, 3.7, and 3.8. Except where specified, the parametric model has been fitted twice, following the prescription of the deconvolution method in Section 3.4, in which the feature behind the bar is subsumed into the background. By fitting to the S-model simulation generated by the parameters in Table 3.5, we hoped to gauge the impact on the likelihood of different background and parametric model cases used in bulge modelling. Note that in the simulation, we chose $Z_\odot = 15$ pc. As can be seen in Fig. 3.7, the range of fitted model parameters is much greater than the error bars in Table 3.2. This indicates the main cause of the variation is due to model assumptions rather than statistical error.

We used the following test statistic to compare the different cases:

$$\mathrm{TS} \equiv -2\ln(\mathcal{L}/\mathcal{L}_{\mathrm{base}}) \tag{3.14}$$

As most of the variation between cases was due to systematic error rather than statistical error, we did not use Wilks' theorem (Wilks, 1938) which is also only suited for nested models. Instead, we evaluated the range of TSs expected from the general variation in the simulation fits, visualised for reference in Fig. 3.8.

As can be seen in that figure, the simulation has a negligible TS when testing against case B which does not account for a feature behind the bulge. This is to be expected as this feature was not present in the simulation. In contrast the data has a high TS for case B. This indicates that the feature behind the bulge is significant.

Case H is an S-model with $Z_\odot = 0$ pc. As can be seen from Fig. 3.8, both the simulation and data significantly prefer the SX model. The reason why the simulation still disfavours this S-model with respect to the SX model is that the simulation was

generated from an S-model with $Z_\odot = 15$ pc. It is therefore unsurprising that the F case is very slightly favoured over the SX model for the simulation. This follows in that the F case is of the same form as the model used to generate the simulation. However, case F is even more disfavoured by the data than case H. From this we conclude that the data favours the SX model over the S-model and this conclusion is not affected by reasonable changes in $Z_\odot$.

The additional model cases are discussed in Sec. 3.7.

3.5 Testing Deconvolution Against Simulation

In this section we test our maximum entropy deconvolution method (see Section 3.4) against a simulated Milky Way population comprised of a thin disk, thick disk and a bulge, as is modelled in S17. To generate the synthetic population we used the equation of stellar statistics: López-Corredoira et al., 2000

$$N\left(K_s\right) = \sum_i \int_0^\infty \rho_i\left(s\right) \Phi_i\left(K_s - 5\log s + 10\right) s^2 \Delta\Omega ds \tag{3.15}$$

where ρ is the density and Φ is the luminosity function and the sum is over the three model components, to predict the combined star counts in each (K_s, l, b) bin. We then simulated a population of stars by drawing a Poisson random value from the binned simulation model.

Following S17, we modelled the thick and thin discs using the description for the Besançon galaxy model (Robin et al., 2003). The thin disc was constructed from seven sub-populations which have different ages spanning 0-10 Gyr, where the star formation rate was assumed constant for each sub-population. All sub-populations were assumed to have relaxed into isothermal distributions, where the density distribution is a cylindrically symmetric holed ellipsoid, described by an Einasto, 1979 density law

$$\begin{aligned}\rho_{\rm thin}(R, Z_{\rm cyl}) = \rho_0 \Bigg[&\exp\left(-\sqrt{0.25 + \left(\frac{a}{h_t}\right)^2}\right) \\ &- \exp\left(-\sqrt{0.25 + \left(\frac{a}{h_h}\right)^2}\right)\Bigg]\end{aligned} \tag{3.16}$$

with

$$a^2 = R^2 + \left(\frac{Z_{\rm cyl}}{\epsilon}\right)^2 \tag{3.17}$$

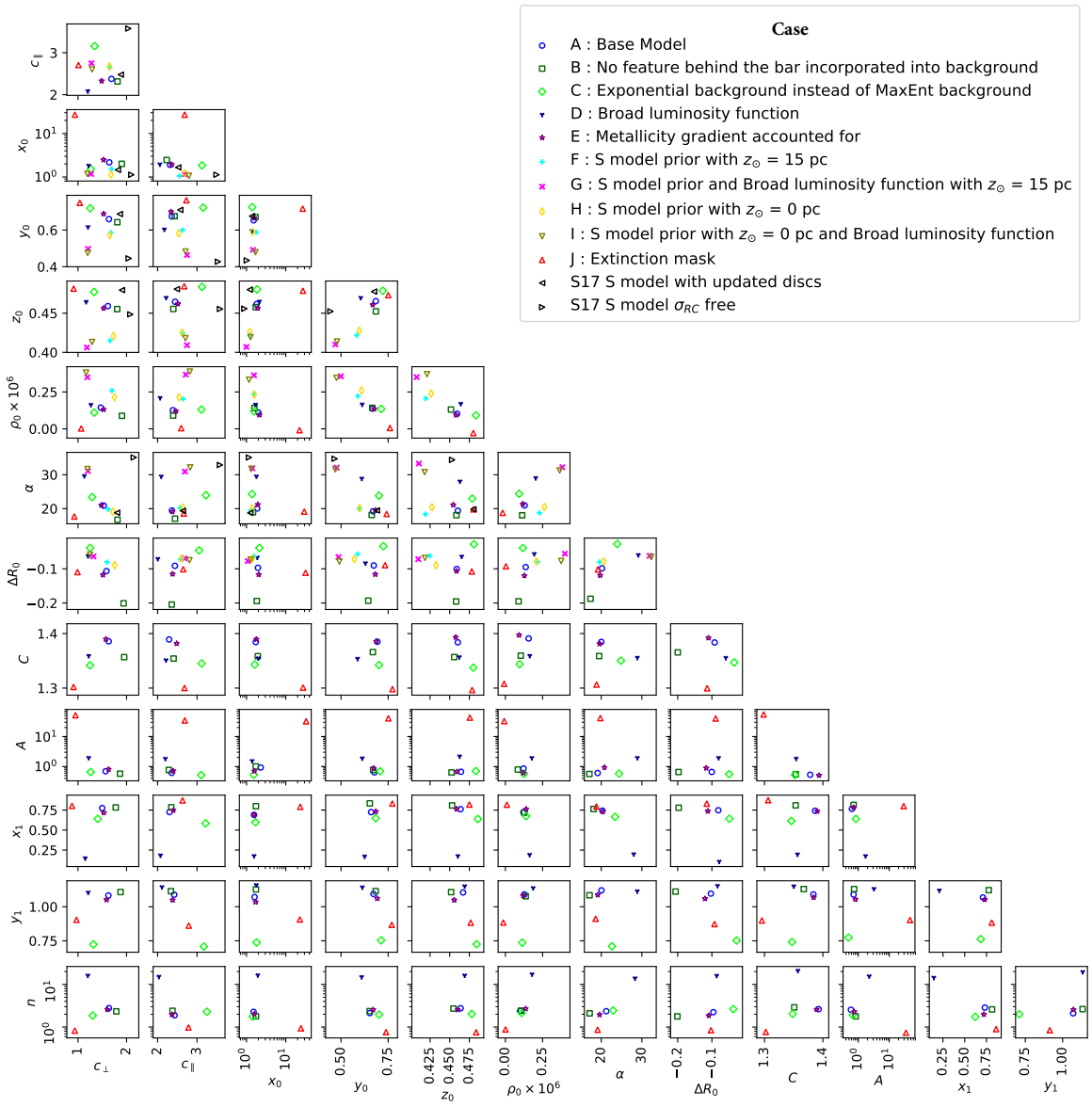

Fig. 3.6 Pair plot of parametric model parameters fitted for the base case and systematics on the VVV data. Note that the axis scaling for parameters x_0, A, and n are logarithmic. See Table 3.1. To reduce overlapping symbols, the plotted points have had a random jitter added to them, which is of order 10% of the corresponding axes range.

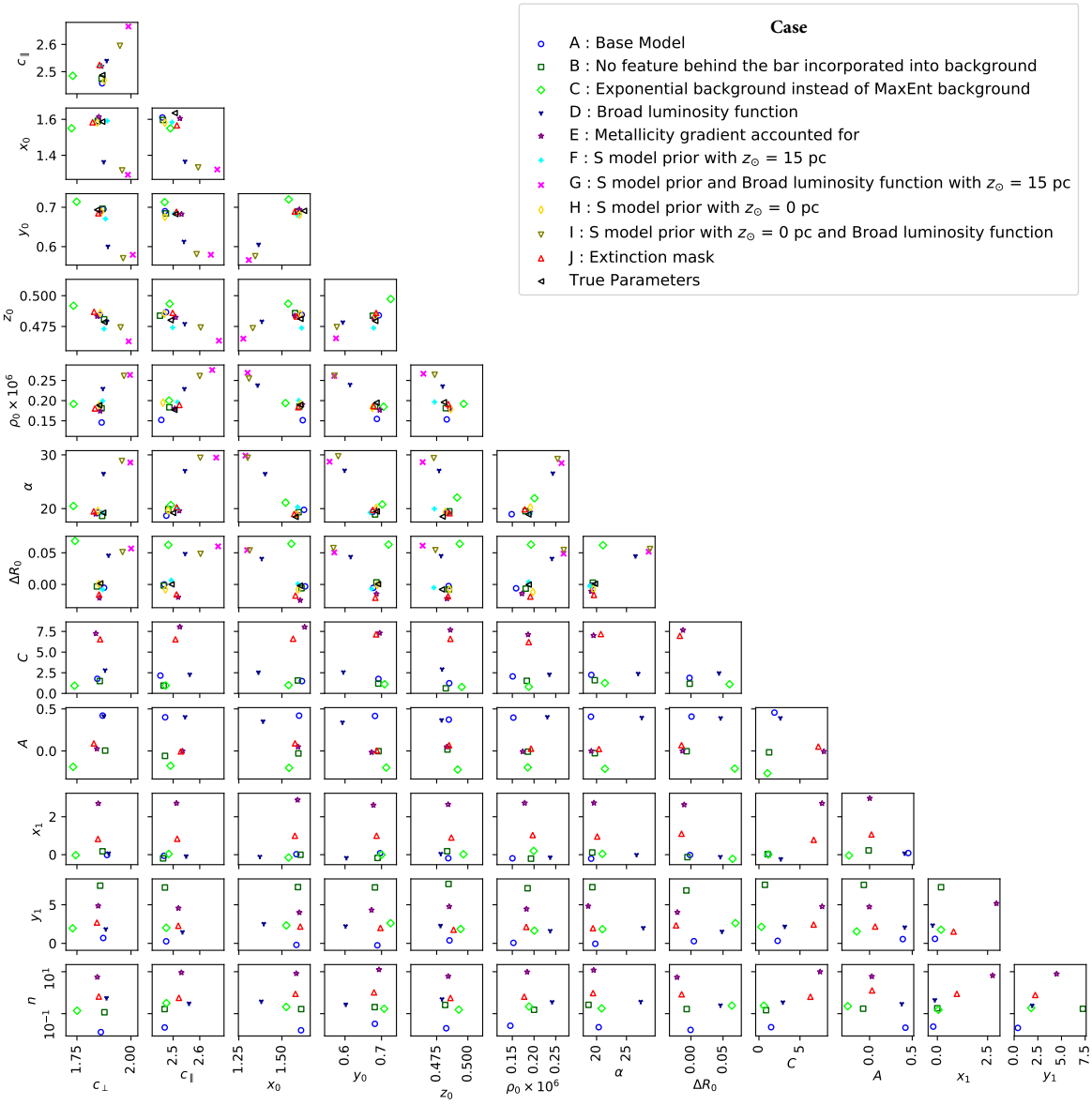

Fig. 3.7 Pair plot of parametric model parameters fitted for the base case and systematics to simulations. See Table 3.2. The n parameter has been plotted on a logarithmic scale. To reduce overlapping symbols, the plotted points have had a random jitter added to them, which is of order 10% of the corresponding axes range.

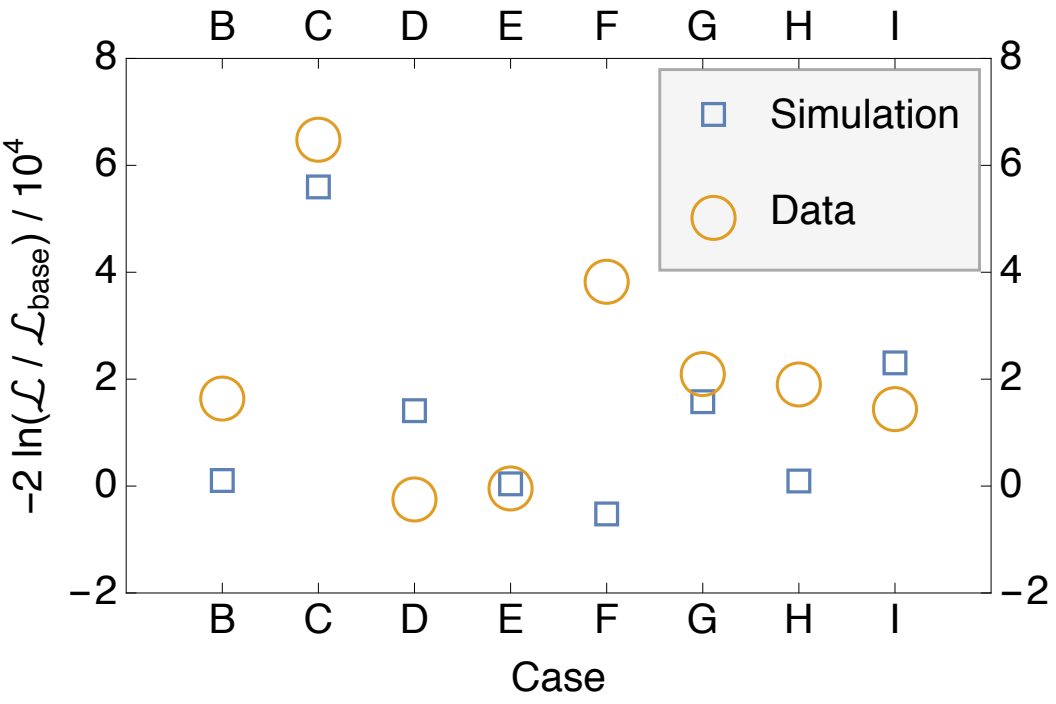

Fig. 3.8 The parametric fit likelihoods ($\mathcal{L}$) of the different cases considered. The base model's parametric likelihood is $\mathcal{L}_{\rm base}$. Results are shown for both the simulation and the data. In the simulation case the base model and labelled model are both fit to the simulated data. See Table 3.7 for numerical values. The cases considered are: no behind the bar feature subtraction (B), exponential background (C), broad luminosity function (D), metallicity gradient (E), S-model prior with $Z_\odot = 15$ pc (F), S-model prior and broad luminosity function with $Z_\odot = 15$ pc (G), S-model prior with $Z_\odot = 0$ pc (H), S-model prior with $Z_\odot = 0$ pc with a broad luminosity function (I).

where R and $Z_{\rm cyl}$ are cylindrical co-ordinates in kpc, h_t is the scale length of the disc and h_h is the scale length of the hole in kpc. The axis ratio of the ellipsoid, ϵ, is age dependent. The values for the thin disc density parameters from Robin et al., 2012 were used in this model, and are summarised in Table. 3.3. We generated a luminosity function for each sub-population of the thin disc using the method described in Section 3.3 assuming a broken power law IMF;

$$\xi\left(m\right) = \begin{cases} m^{-1.6}, & m \leq 1M_{\odot} \\ m^{-3.0}, & m > 1M_{\odot}. \end{cases} \tag{3.18}$$

Within each sub-population, the metallicity is distributed normally in [Fe/H] with mean and dispersion as given in Table 3.4. We used mass-absolute magnitude relations from the PARSEC+COLIBRI isochrones (Marigo et al., 2017).

The formation history of the thick disc was assumed to be a single burst event 12 Gyrs ago. The density profile used is distributed exponentially radially, where vertically the density is parabolic near the plane, transitioning to exponential further away from the plane

$$\rho_{\rm thick}\left(R,Z\right) = \begin{cases} \rho_0 \exp\left(-\frac{R-R_{\odot}}{h_T}\right)\left[1-\frac{Z^2}{h_z}\frac{1}{\zeta(2+\zeta/h_Z)}\right] & Z \leq \zeta \\ \rho_0 \exp\left(-\frac{R-R_{\odot}}{h_T} - \frac{|Z-Z_{\odot}|}{h_Z}\right)\frac{2\exp(\zeta/h_Z)}{1+\zeta/h_Z} & Z > \zeta \end{cases}, \tag{3.19}$$

where $(R_{\odot}, Z_{\odot}) = (8.0\ \text{kpc}, 15\ \text{pc})$ is the position of the Sun. Parameter, h_T is the radial scale length, h_Z is the vertical scale height and ζ is the height where the density transitions from parabolic to exponential. The IMF for the thick disc is a simple power law

$$\xi\left(m\right) = m^{-0.22}. \tag{3.20}$$

Both the thick and thin discs were modelled as having a warp and a flare,

$$Z_{\rm warp} = \gamma_{\rm warp}(R - R_{\rm warp})\cos\left(\phi - \phi_{\rm warp}\right) \tag{3.21}$$

where the density in Eq. 3.16 and Eq. 3.19 at Z, is instead evaluated at $Z + Z_{\rm warp}$ when $R > R_{\rm warp}$; $\phi_{\rm warp}$ is the direction in which the warp is maximum. The flare was modelled by linearly increasing the scale height by

$$h_{\rm flare} = \gamma_{\rm flare}(R - R_{\rm flare}) \tag{3.22}$$

Table 3.3 Density distribution parameters for the Besançon thick and thin discs used for our simulation

Component	Age	$h_{t/T}$	ϵ/h_Z	h_h
Thin Disc	0.0-0.15	5.00	0.0140	3.00
	0.15-1	2.53	0.0268	1.32
	1-2	2.53	0.0375	1.32
	2-3	2.53	0.0551	1.32
	3-5	2.53	0.0696	1.32
	5-7	2.53	0.0785	1.32
	7-10	2.53	0.0791	1.32
Thick Disc	12	2.36	0.535	-

Table 3.4 Metallicity distribution parameters for the Besançon thick and thin discs used for our simulation

Component	Age (Gyr)	$\mu_{[Fe/H]}$	$\sigma_{[Fe/H]}$
Thin Disc	0.0-0.15	-0.01	0.12
	0.15-1	-0.03	0.12
	1-2	-0.03	0.10
	2-3	-0.01	0.11
	3-5	-0.07	0.18
	5-7	-0.14	0.17
	7-10	-0.37	0.20
Thick Disc	12	-0.78	0.3

when $R > R_{\rm flare}$. We used the same parameters for the flare and warp as Robin et al., 2003; $\gamma_{\rm warp} = 0.18$, $R_{\rm warp} = 0.98 R_\odot$, $\phi_{\rm warp} = 90.0°$, $\gamma_{\rm flare} = 0.0054$ and $R_{\rm flare} = 1.12 R_\odot$. The disc parameters we used are listed in Tables 3.3 and 3.4.

The density of the S model is of the form

$$\rho = \rho_0 \, \mathrm{sech}^2 \left(r_s \right), \tag{3.23}$$

where,

$$r_s = \left(\left[\left(\frac{X}{x_0} \right)^{c_\perp} + \left(\frac{Y}{y_0} \right)^{c_\perp} \right]^{\frac{c_\parallel}{c_\perp}} + \left(\frac{Z}{z_0} \right)^{c_\parallel} \right)^{\frac{1}{c_\parallel}}. \tag{3.24}$$

We used the parameters from S17 Table 3 for the S model with updated disks, also given here in Table. 3.5. The normalisations we used for each of the three components

Table 3.5 Density distribution parameters for the bulge component used for our simulation. The second row gives the total number of stars in the unmasked regions of the simulation in the range $12 < K_s < 14$.

x_0(kpc)	y_0(kpc)	z_0(kpc)	$\alpha(^\circ)$	$c_{\parallel}$	$c_{\perp}$
1.61	0.69	0.48	-19.16	2.50	1.86

$N_{\rm thin}(\times 10^6)$	$N_{\rm thick}(\times 10^6)$	$N_{\rm bulge}(\times 10^6)$
1.35	1.87	17.04

have been scaled up so that the total number of stars in the unmasked region and in $12 < K_s < 14$ matches the number of stars in the VVV PSF catalogue. The luminosity function we used for the bulge in the simulation is the same as we used in our fitting procedure, described in Section 3.3.

To choose the values of the regularisation parameters we tested a range of choices in a $1^\circ \times 1^\circ$ region centred on $(l, b) = (0.9, -6.1)$. For this test, we did not want to use a prior that was too close to the true value, so we used the base SX (Eq. 3.12) model that had been fitted to the VVV data (see case A in Fig. 3.6). We first fixed the maximum entropy regularisation parameter, λ from Eq. 3.10, to zero and applied our maximum entropy deconvolution method with a range of smoothing regularisations, η. We repeated this for $\eta = 0$ and a range of λ values. In Fig. 3.9 the deconvolved density for all choices of η follow the general shape of the true density. Small values of η give spurious oscillatory deviations from the true density, which decrease in amplitude as η increases. There is not a significant difference in the predicted star counts between the choices of η. For $\lambda \geq 1.0$, the predicted star counts deviate significantly from the simulation, which is also seen in the deconvolved density where it overestimates at distances less than 6 kpc, and underestimates from 6-8 kpc. This is because the prior density is not a good estimate of the true density for the current case. When $\lambda = 0.01$, the deconvolved density is scattered around the simulated density, and the predicted star counts are over-fitting. The results of this test suggested that a small value of λ and a large value of η would give the most accurate density deconvolution. Therefore, we used a value of $\lambda = 0.01$ and $\eta = 100 - 1000$. For the background modelling, a simulation is not needed to determine an optimal set of regularisation parameters, as the effectiveness can be determined by directly comparing to the data. Also, the prior background from the S17 model gives a good description of the background. This means we expect less deviation from the prior and so a larger value of λ can be used.

The regularisation parameters used for the background determination are presented in Table 3.6.

The distribution of curvature in log-density (Eq. 3.6) for the simulated bulge in Fig. 3.10 is strictly negative. It is broadest in b, second broadest in l and narrowest in s. The ℓ_2-norm regularisation gives a minimum penalty to the likelihood when the log of the fitted density has zero curvature. Larger values of η narrows the fitted distribution, so we used larger values of η for s than l and b. The regularisation parameters used for fitting the simulated population are summarised in Table 3.6.

We applied the maximum entropy deconvolution process to the simulated star counts, first by fitting the background including the feature behind the bar, then by fitting a parametric density model to determine a prior density estimation for the full 3-D density deconvolution. The parameters of the fitted prior density are presented in Table 3.2, labelled case A. The maximization of the $\ln \mathcal{L}$ in Eq. 3.10 and $\ln \mathcal{L}$ in Eq. 3.7 were both performed using the python implementation PYLBFGS[2] of the Limited Memory Broyden-Fletcher-Goldfarb-Shanno (L-BFGS) algorithm.

The density was modelled non-parametrically on a (257, 100, 50) grid of (s, l, b), in the range $4 < (s/\mathrm{kpc}) < 13$, $-10^\circ < b < 0^\circ$ and $-10^\circ < l < 10^\circ$, for a total of $1.285{\times}10^6$ free parameters. The grid spacing is $(\Delta s, \Delta l, \Delta b) = (35\ \mathrm{pc}, 0.2^\circ, 0.2^\circ)$. To make the optimization of so many parameters feasible, we evaluated the gradients of $\ln \mathcal{L}$ in Eq. 3.10 and $\ln \mathcal{L}$ in Eq. 3.7 analytically, see Appendix A more details. We assumed symmetry about the Galactic mid-plane so that we could reliably extend our non-parametric density model to latitudes $b > 5^\circ$, where there are no observations in the VVV sample. Making the two-fold symmetry assumption forced us to position the Sun in the Galactic mid-plane ($Z_\odot = 0$ kpc). We fixed the reconstructed density just outside the region of interest to the prior density by setting $\lambda = 1$ in those regions. This meant that the smoothness regularisation forced the reconstructed density to smoothly transition to the parametric prior density at $|l| > 10^\circ$ and $|b| > 10^\circ$.

Shown in the top panel of Fig. 3.11 is the background fitted to the simulation. From the deconvolution of the VVV data shown in Fig. 3.11, we can see the simulated population lacks a splitting of the RC peak that is present in the VVV observations case shown in Fig. 3.12. In Fig. 3.13 we compare the 3-D deconvolved density to the density used in simulating the population. The deconvolved density using the maximum entropy method compares well to the density used in our simulation, even inside of the masked regions where there is no data influencing the deconvolution.

[2] https://github.com/dedupeio/pylbfgs

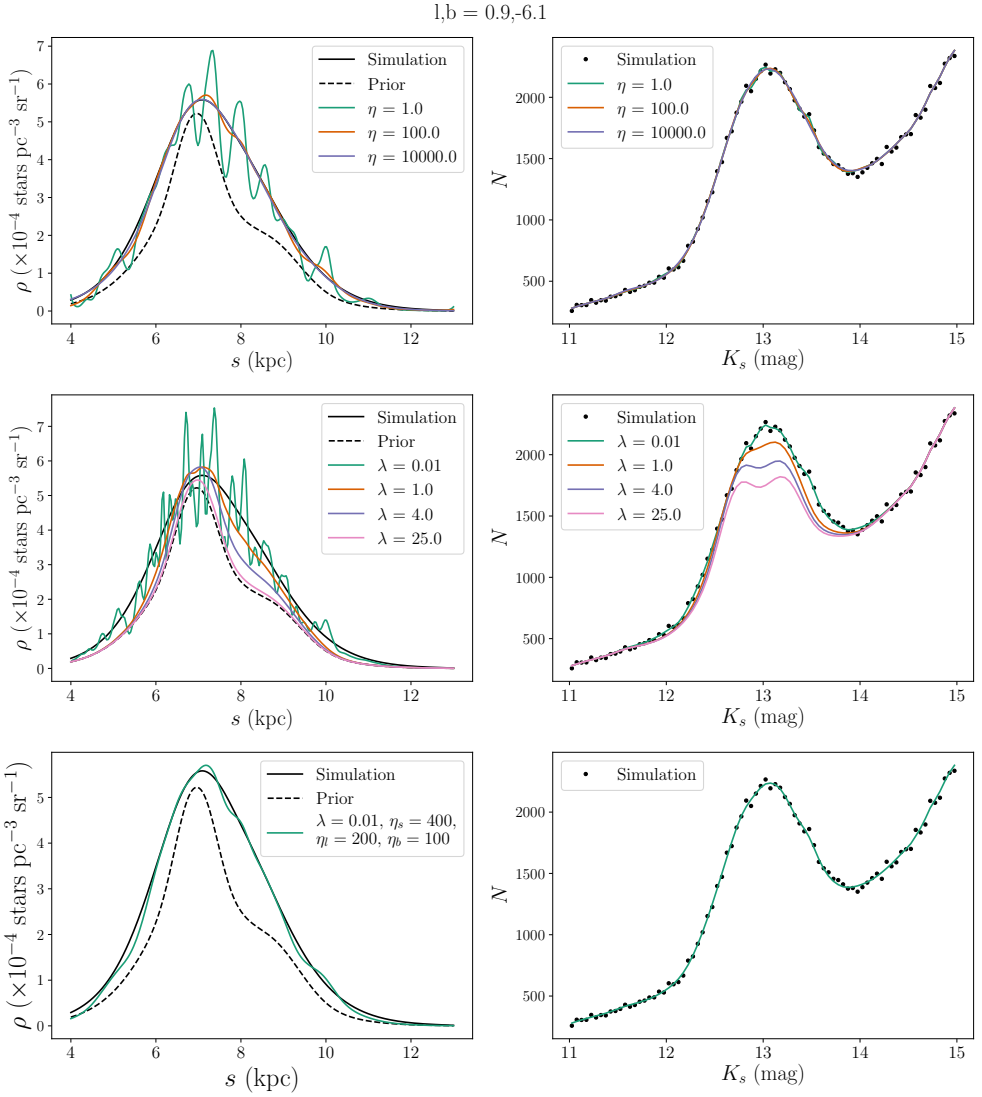

Fig. 3.9 Testing the choice of regularisation parameters. We perform our maximum entropy deconvolution to a $1^\circ \times 1^\circ$ region of our simulated population, centred on $(l, b) = (0.9, -6.1)$. In the top panels, the maximum entropy regularisation is set to zero, and a range spatial smoothness parameter values are tested. The middle panels have the spatial smoothness regularisation set to zero, and a range of maximum entropy regularisation values are tested. The bottom panels have the regularisation parameters used in our final analysis. The left panels show the deconvolved density compared to the true density in the simulation, the right show the model star counts (N) compared to the simulated population (n). For small values of η, the deconvolved density has many spurious features, which get smaller in amplitude as η is increased. The predicted star counts are not significantly sensitive to the choice of η in the range tested here. For all $\lambda \geq 1.0$, the predicted star counts do not match the simulation, where it is clear that the prior density distribution is not a good estimate of the true density.

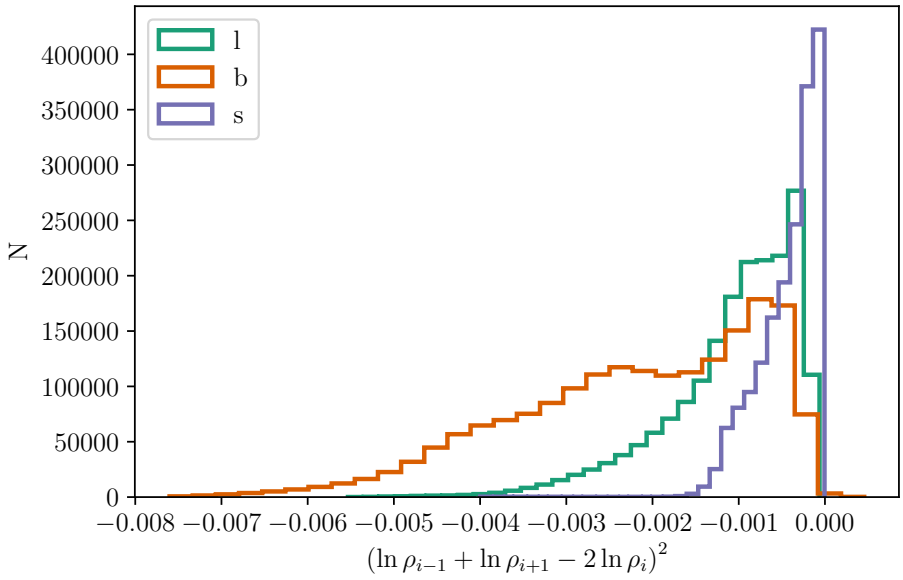

Fig. 3.10 Distributions of the curvature in log-density (Eq. 3.6) along respective density model coordinates of the simulated bulge.

Table 3.6 Regularisation parameters used when fitting to the simulated population and the VVV sample.

	λ	η_s	η_l	η_b
Background	1.0	1000.0	100.0	100.0
3-D Deconvolution	0.01	400.0	200.0	100.0

However, the reconstruction displays some discrepancy at around $s = 4$ kpc. Note that this is due to the low star counts in the bulge at this radius which makes an accurate reconstruction difficult. Note that Fig. 3.13 does not show the X-bulge morphology that is seen in the VVV data which is displayed in Fig. 3.14.

3.6 Deconvolution of VVV

In this section, we discuss how we applied our maximum entropy deconvolution method to the VVV data sample for our base case A. We used the parametric SX model (case A in Fig. 3.6) as the prior density distribution and the values for the regularisation parameters in Table 3.6. The background was fitted using the maximum entropy method of Section 3.4.1. In Fig. 3.12 we present a breakdown of the maximum entropy

deconvolution model components along a single line-of-sight through the region that the photometric split clump has been observed.

Displayed in Fig. 3.15 is a comparison between the predicted star counts by our maximum entropy deconvolution, the fitted parametric model we used as the prior, and the VVV data. For compactness, we show every tenth magnitude bin. At $K_s < 12$ and $K_s > 14$ the RC+RGBB stars contribute negligibly to the total star counts, so both the parametric model and maximum entropy deconvolution are dominated by the background. By construction, these regions are well described by the background model, though perhaps there is slight over-fitting in the $K_s = 14.975$ bin. The non-parametric model reproduced the data well and has smaller deviations in comparison to the parametric model, especially notable in the $K_s = 12.525$ bin at $l = 5°$ where the X-bulge is prominent. The assumption of symmetry about the Galactic mid-plane seems to be reasonable, as there is no visible bias in fitting to the mirrored contours above and below the plane.

The deconvolved density and the fitted parametric density, for fixed latitude bins, are shown in Fig. 3.14. For compactness, only 9 of the 50 bins are displayed and only for $b < 0°$, as the density is assuned to be symmetric about b. Unlike the simulated bulge shown in Fig. 3.13, the density from deconvolution of the VVV data shows the arms of the X-bulge, first noticeable at $b = -8.7°$ for $(l, s) = (4.7°, 6.6 \text{ kpc})$ and $(l, s) = (-3.3°, 9 \text{ kpc})$. As latitude decreases, the arms get closer until they merge at $b = -2.7°$. The maximum density at $b = -2.7°$, where the arms merge, is at longitude $l = -0.7°$. The maximum density of the X-bulge arms in the parametric model do not align with the maximum density in the non-parametric model, which is also evident in the star counts. Cartesian versions of the reconstructed bulge from the VVV data and the simulation are shown in the first columns of Figures 3.16 and 3.17 respectively.

3.7 Systematic Tests

In order to gain a better understanding of the robustness of our results we test systematics based on the following:

- Adding the feature behind the bulge to the background.
- The VVV data mask.
- The determination of the background component.

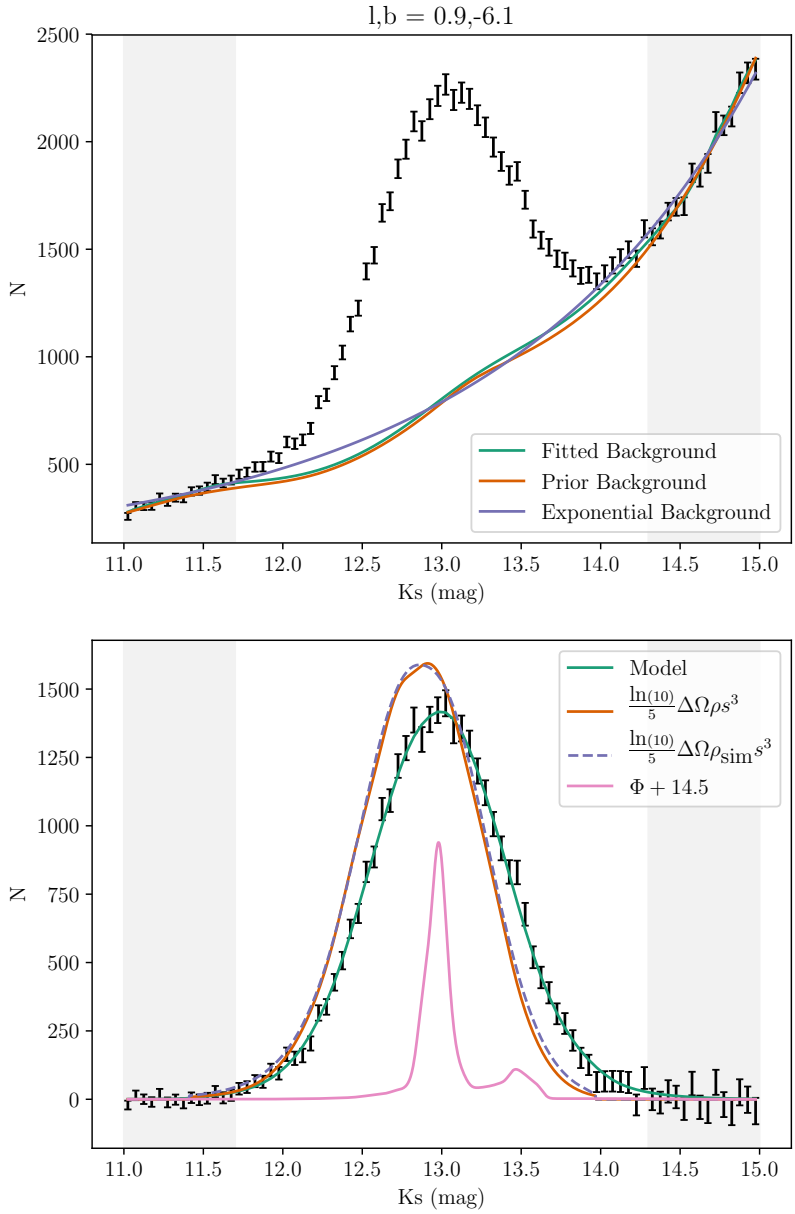

Fig. 3.11 Demonstration of the maximum entropy deconvolution method to a simulated population for a $1^\circ \times 1^\circ$ region. *Top*: The background has been fitted in the grey shaded regions using the maximum entropy method. The prior background is the background of the model used to generate the simulation. *Bottom*: Maximum entropy deconvolution of the line-of-sight star count distribution. Shown in green is the predicted number of RC star counts from the convolution of the fitted density (orange) and assumed luminosity function (pink). The density used to produce the simulation is shown as a dashed purple line. The luminosity function has been scaled for display. The simulated population lacks a split RC peak as seen in Fig. 3.12, and the deconvolved density only has a single peak.

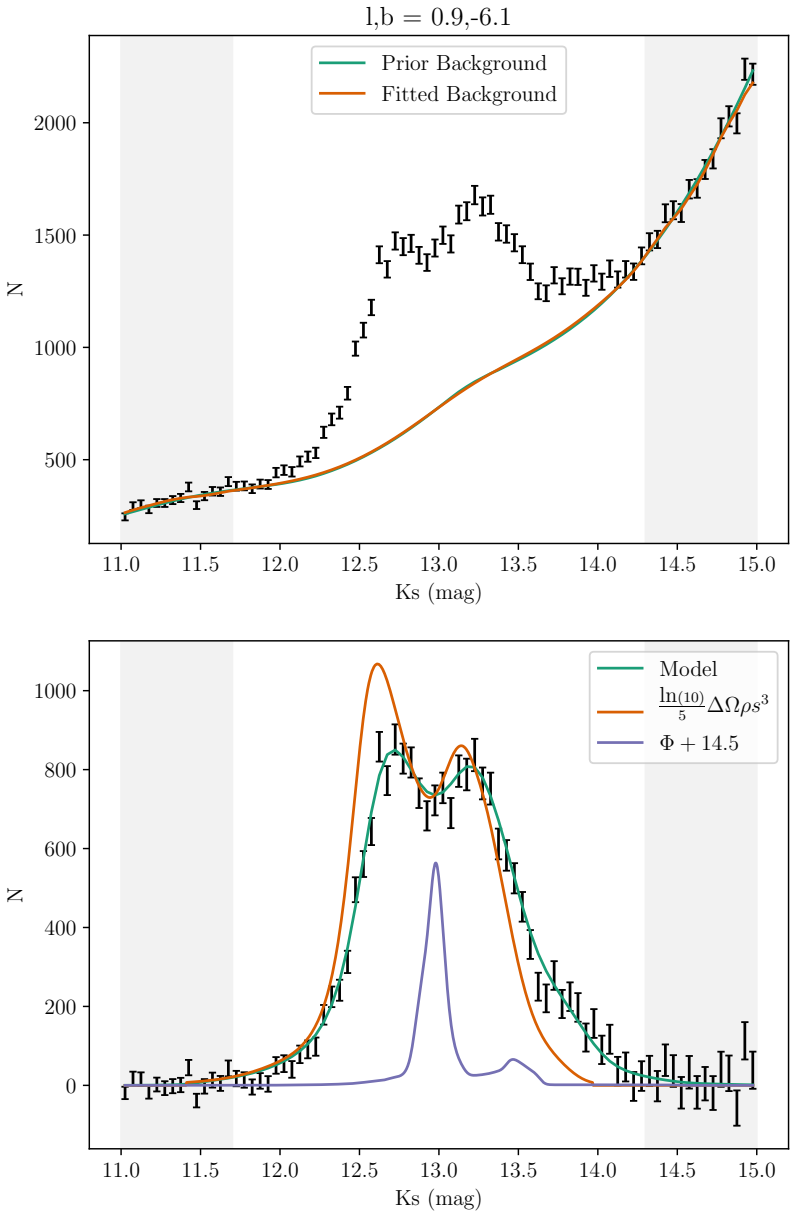

Fig. 3.12 Demonstration of the maximum entropy deconvolution method in a 1° × 1° (5 × 5 pixels) region. *Top*: The background has been fitted in the grey shaded regions using the maximum entropy method. The prior background was calculated using the S17 S-model, which has been scaled to match the VVV observations between $11.0 < K_s < 11.5$. *Bottom*: Maximum entropy deconvolution of the line-of-sight background subtracted star count distribution. Shown in green is the predicted number of RC star counts from the convolution of the fitted density (orange) and assumed luminosity function (purple). The luminosity function has been scaled for display.

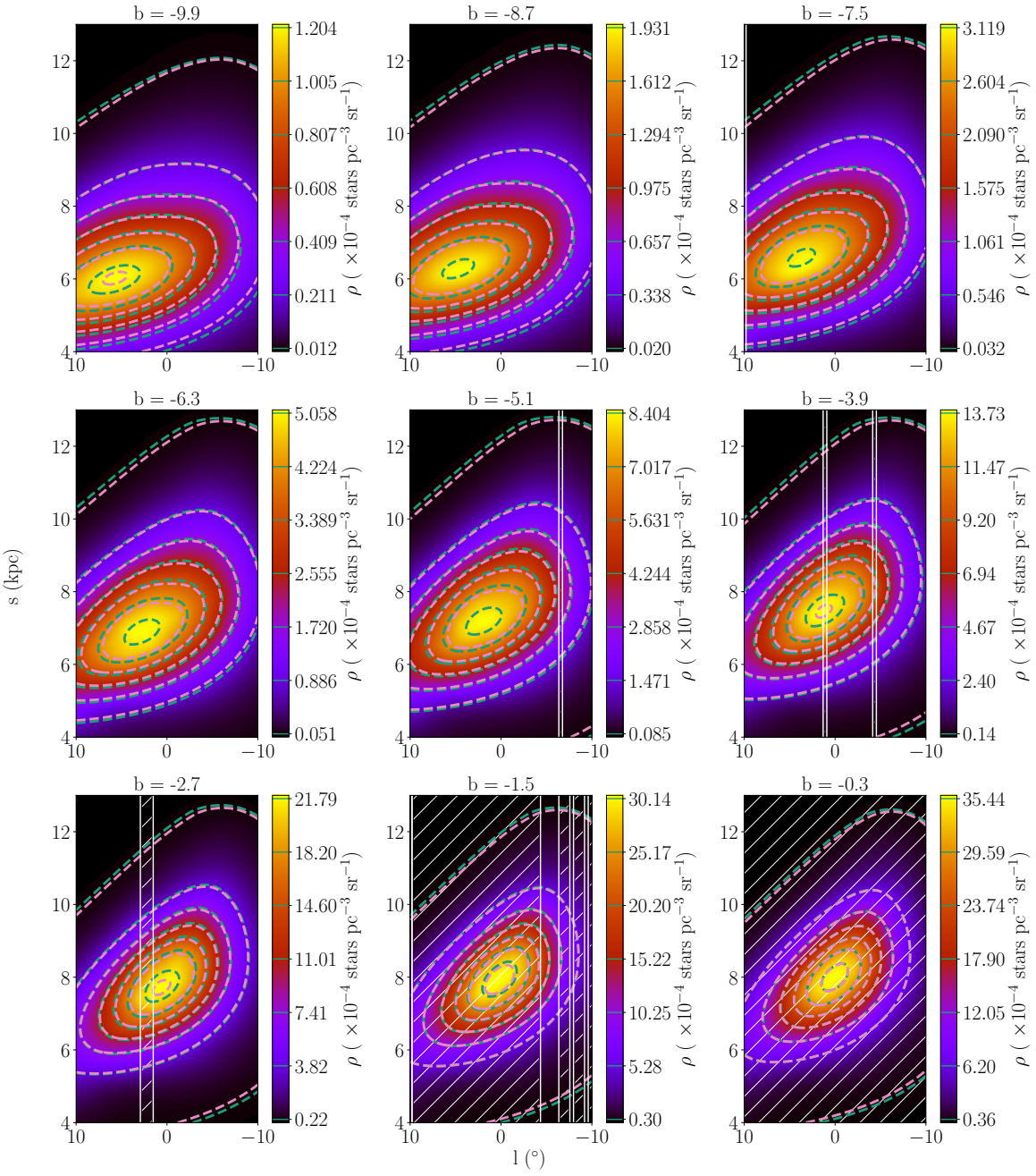

Fig. 3.13 Deconvolved RC+RGBB star density using the maximum entropy method for a simulated 10 Gyr S-model. White hatched regions were masked during the analysis, and were inpainted naturally as part of the deconvolution. Green dashed contours show the true density used in simulating the S-bulge. Pink show the parametric SX model used as the prior density.

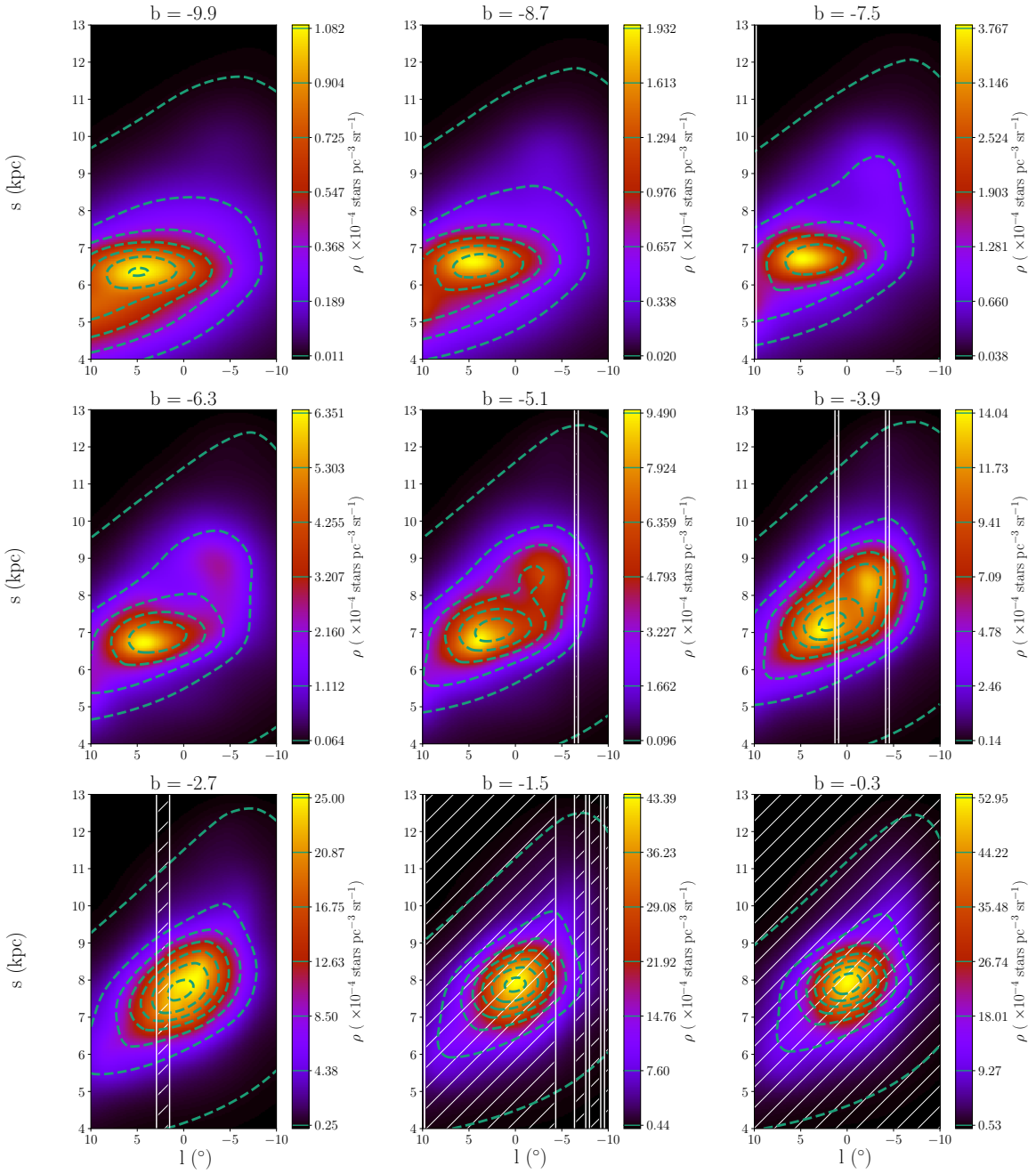

Fig. 3.14 Deconvolved RC+RGBB star density using the maximum entropy method. White hatched regions were masked during the analysis, and were inpainted as part of the deconvolution. The prior density model is shown in green dashed contours.

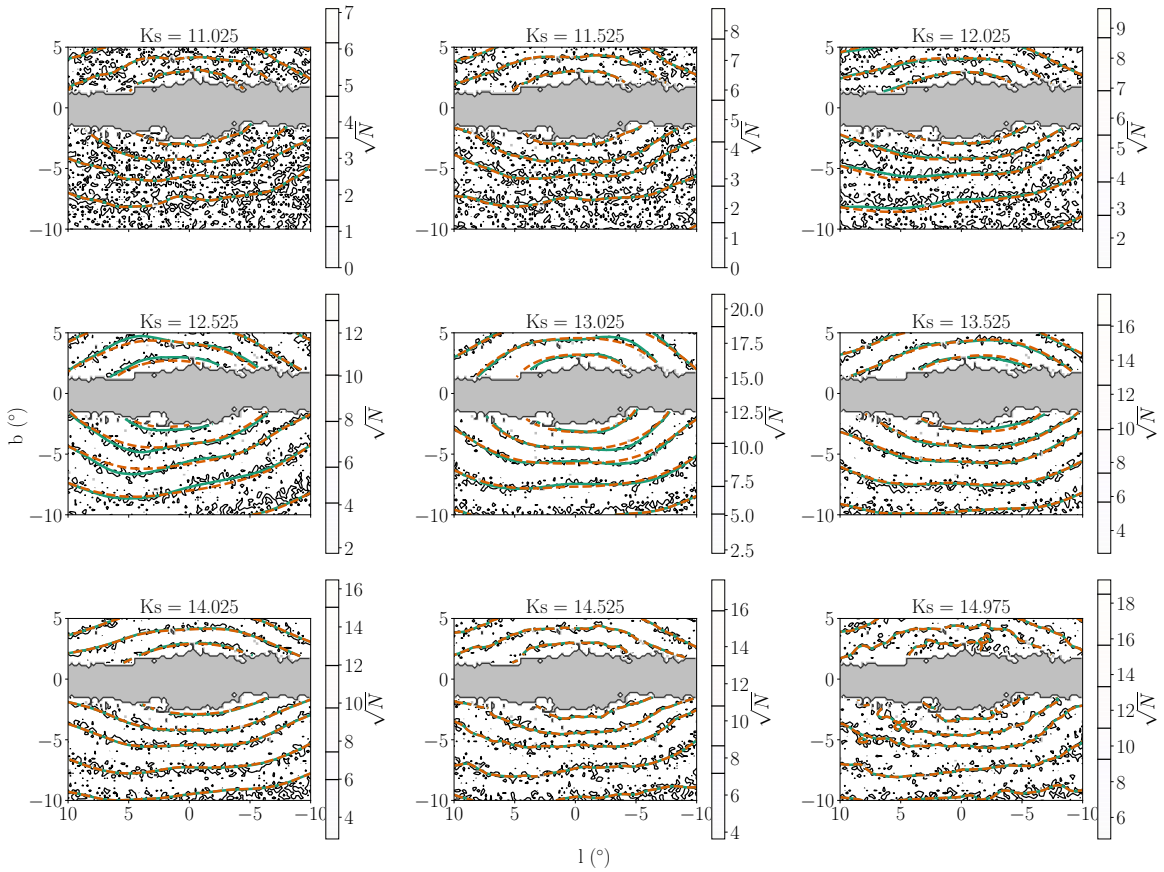

Fig. 3.15 Predicted star counts for our maximum entropy deconvolution method. Black contours show the VVV star counts, where the levels of the contours are indicated by black lines on the colour bar. Green contours show the star counts predicted by the non-parametric model, where the levels match the black contours. The orange dashed line is the parametric model used as the prior.

Table 3.7 Minimum values of $-2\ln\mathcal{L}$. The base case (A) values of $(-1.36968, -2.35631, -1.4102015, -2.32068) \times 10^8$ have been subtracted from columns one to four respectively. The non-base cases considered are: no behind the bar feature subtraction (B), exponential background (C), broad luminosity function (D), metallicity gradient (E), S-model prior with $Z_\odot = 15$ pc (F), S-model prior and Broad luminosity function with $Z_\odot = 15$ pc (G), S-model prior with $Z_\odot = 0$ pc (H), S-model prior with $Z_\odot = 0$ pc with a broad luminosity function (I), extinction mask (J).

	VVV Data		Simulation	
Case	Parametric	Non-parametric	Parametric	Non-Parametric
A	0	0	0	0
B	17086	974	733	307
C	65507	60554	55654	69758
D	-1793	2917614	13797	76778
E	266	184	109	-1641
F	38934	241421	-5523	176708
G	21665	209841	15475	161736
H	19723	1361	640	95
I	15107	25589	22740	6252
J	-23656527	-36916846	-16226836	-26086218

- The semi-analytic luminosity function.
- The metallicity distribution.
- The position of the Sun.
- The deconvolution method used.

We tested the significance of these assumptions by systematically changing one, then repeating the maximum entropy deconvolution, including the background fitting and parametric prior density model fitting. We also repeated the deconvolution with the new assumptions on the simulated population. The resulting TS for the systematic tests are plotted in Fig. 3.8 for the parametric model and Fig. 3.18 for the non-parametric model.

3.7.1 Feature Behind the Bulge

Unlike the parametric case we discussed in Section 3.4.4, we do not find a significant change in our penalized likelihood when not removing the feature behind the bulge. This can be seen in Fig. 3.18 where case B has a TS very close to zero for both the

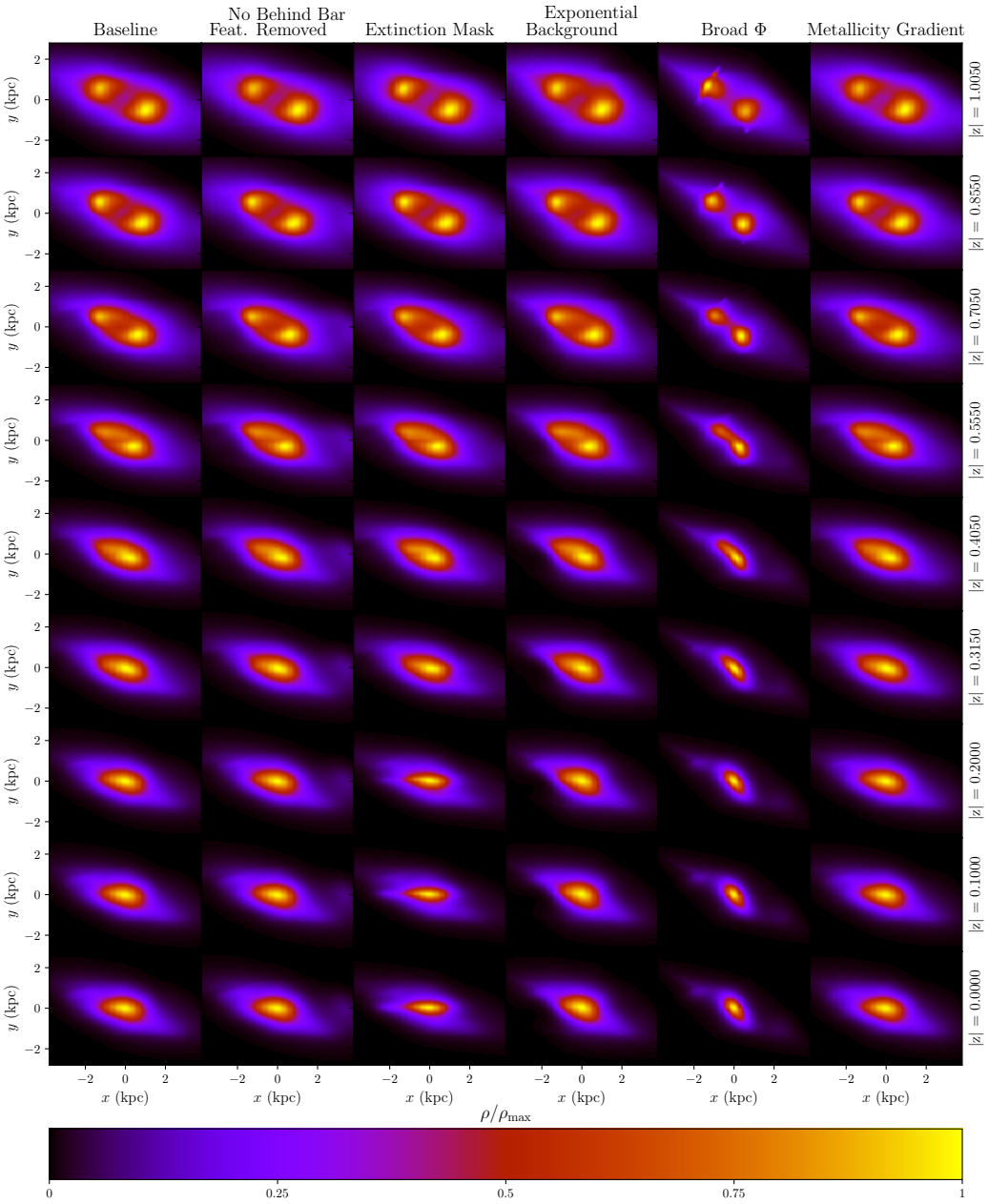

Fig. 3.16 Cartesian projections of the deconstructed density of the VVV RC stars in the bulge, for several systematic test cases. The x-axis is aligned with the Sun-Galactic centre line and the z-axis is perpendicular to the Galactic plane and measured in kpc. The Galactic centre is located at the maximum bulge density. The significance of each test case is discussed in the text in Section 3.7

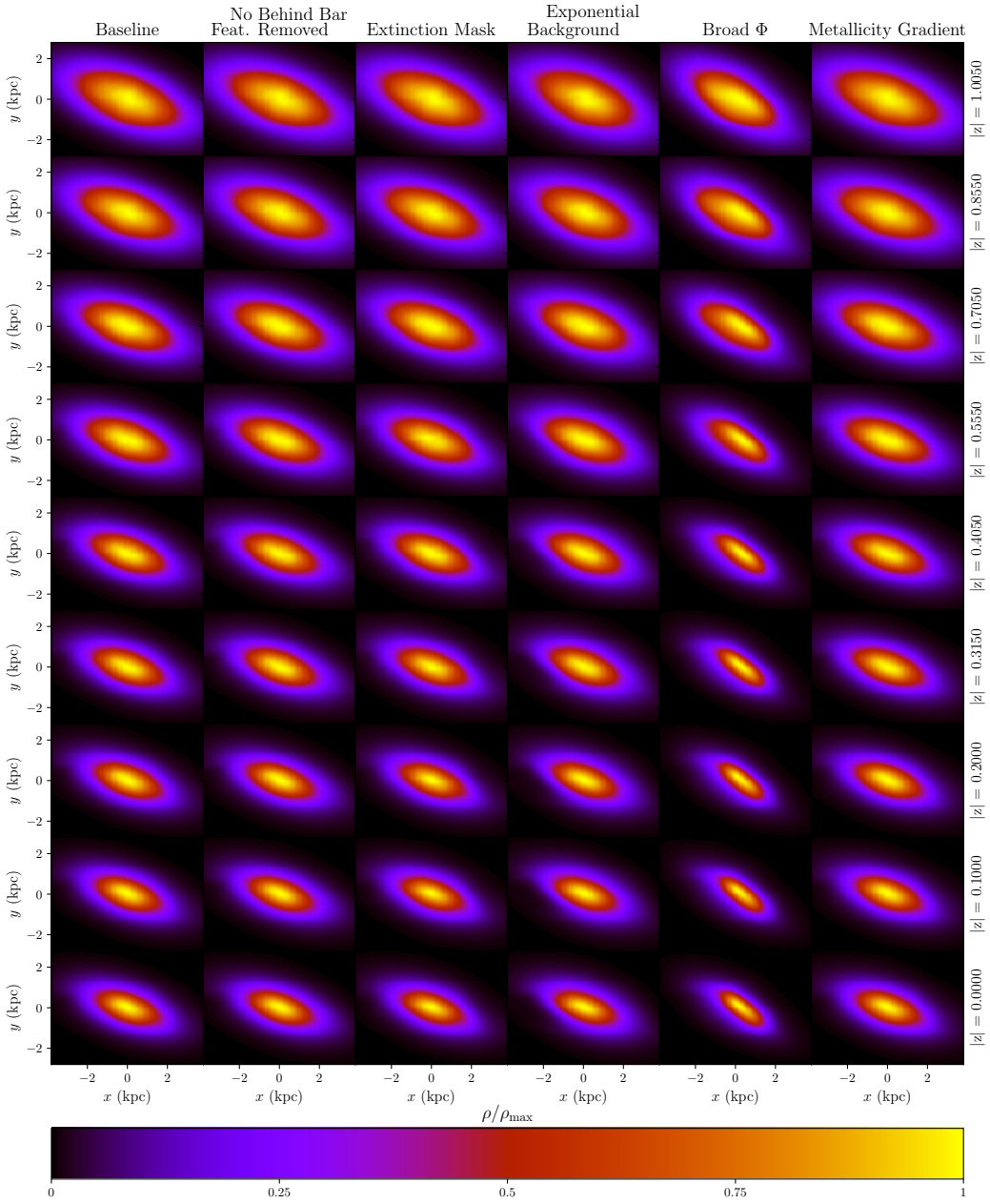

Fig. 3.17 Cartesian projections of the deconstructed density of the simulated bulge population, for several systematic test cases. The x-axis is aligned with the Sun-Galactic centre line. Nearly all of the cases give a qualitatively similar density to the base case. However, the exponential background gives densities that are too low at $(x, y) = (-2.5\text{kpc}, 0\text{kpc})$, especially at low latitudes. Also, the broadened luminosity function gives a larger bar angle than the base case. The two exceptions noted here are also seen in the VVV data (Fig. 3.16).

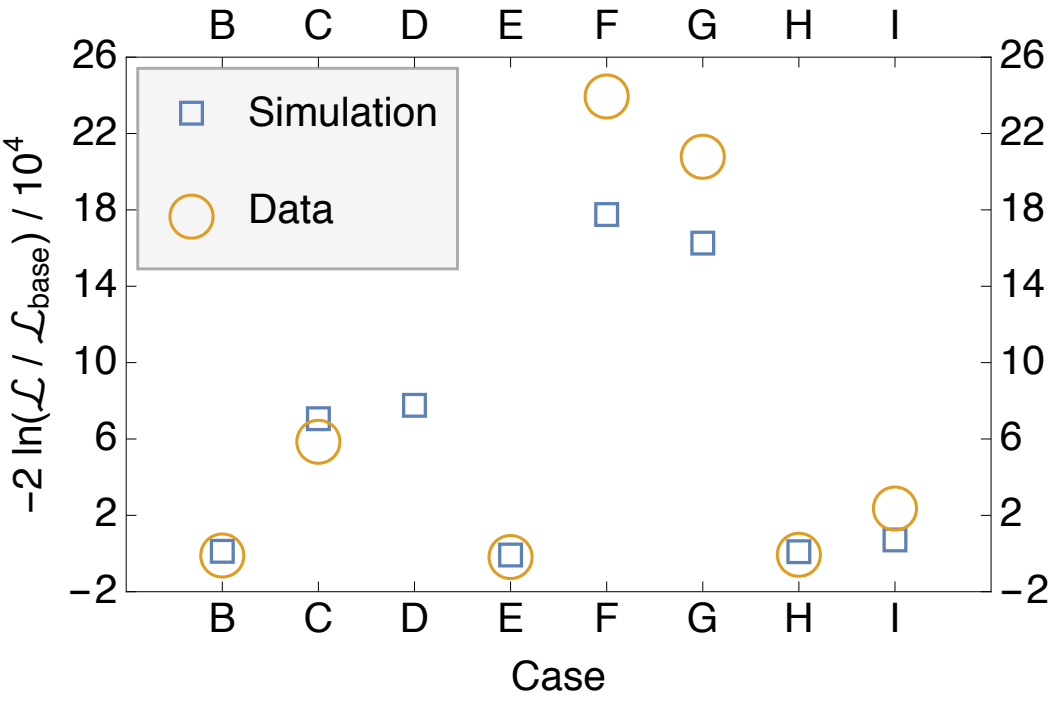

Fig. 3.18 The non-parametric likelihood ($\mathcal{L}$) different cases considered. The base case's non-parametric likelihood is $\mathcal{L}_{\rm base}$. Results are shown for both the simulations and the data. In the simulation case, the base case and labelled case are both fit to the simulated data. Case D's data symbol is not shown due to it's very low likelihood value not being in the range of the plot. See Table 3.7 for numerical values. The cases considered are: no behind the bar feature subtraction (B), exponential background (C), broad luminosity function (D), metallicity gradient (E), S-model prior with $Z_\odot = 15$ pc (F), S-model prior and Broad luminosity function with $Z_\odot = 15$ pc (G), S-model prior with $Z_\odot = 0$ pc (H), S-model prior with $Z_\odot = 0$ pc with a Broad luminosity function (I), extinction mask (J).

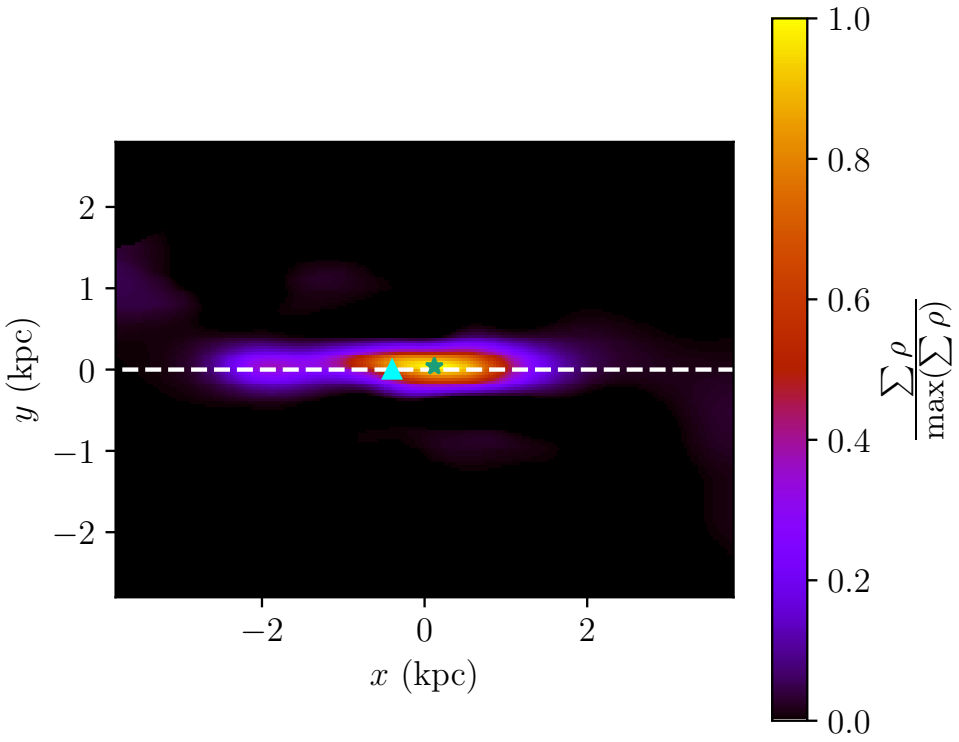

Fig. 3.19 Difference between the deconvolved density using a crowding + extinction based mask and a extinction only mask in Cartesian co-ordinates where x is aligned with the Sun-Galactic centre line. The density difference has been summed over $|z < 1\,\mathrm{kpc}|$. The white dashed line indicates $l = 0°$. The maximum density of the difference (indicated by a green star) is 150 pc behind the maximum density location of the crowding + extinction based mask reconstructed bulge. The cyan triangle is at the expected maximum density location for a population that would have a RC 0.1 mag brighter than our PARSEC derived semi-analytic luminosity function, such as a 5 Gyr old population or a more metal rich population.

data and simulation. This is to be expected as the flexibility of the non-parametric method can easily incorporate the feature behind the bulge as being part of the bulge as seen by comparing column 1 and 2 in Fig. 3.16. While for the simulation, where there should be no feature behind the bulge, the corresponding columns are virtually indistinguishable as seen in Fig. 3.17.

3.7.2 Mask Systematic

We changed the region in which the data is excluded, from the combined extinction boundary and Ks-band uncertainty boundary case ($E(J-K) > 0.9$ and $\langle \sigma_{K_s} \rangle > 0.06$), to just the extinction based exclusion boundary. This systematic test changes the amount of data used in the analysis, so the likelihood is not comparable to the base case. In Fig. 3.16, the density that is reconstructed with an extinction only mask has a prominent bar-like feature at $|z| < 0.2\,\mathrm{kpc}$, that is pointed nearly directly towards the Sun. Note, that this feature is not seen in the corresponding simulation result of Fig. 3.17. We extracted this feature by subtracting the baseline case. Plotted in Fig. 3.19 is the sum of the density difference for all density with $|z| < 1\mathrm{kpc}$. At first glance, this apparent over-density looks similar in structure to the younger, secondary population of bulge stars in S17 (E component of the S+E-model). The green star indicates the maximum density of the difference and is located at $(x, y) = (120\,\mathrm{pc}, 90\,\mathrm{pc})$. This is 150 pc behind the centre of the bulge ($(x, y) = (0\,\mathrm{pc}, 0\,\mathrm{pc})$). This suggests that the stars are unlikely to be from a significantly younger or more metal rich population than the rest of the stars in our bulge model, as they would have a brighter RC in the luminosity function than we have modelled. A 5 Gyr old population, with a similar metallicity distribution to our fiducial case, has a 0.1 mag brighter RC. This corresponds to a difference of 400 pc closer at 8 kpc, indicated by the cyan triangle on Fig. 3.19.

We argue based on the reconstructed distance from the Sun, that the apparently over-dense region is not consistent with a different population of stars. Its orientation, which is suspiciously pointed directly towards the Sun, and is distinctly different from the majority of the bulge population also makes it inconsistent with main population of the bulge stars. This was one of our motivations in using the crowding+extinction based mask over the extinction only based mask. A combination of significant crowding and residual extinction deteriorates the quality of the star count catalogues, including the photometric zero-point.

3.7.3 Background Systematics

We changed the background in case C to one that is common in the literature, a second order polynomial in $\log(N)$, described in Section 3.7.7. We have already displayed this background for a couple of lines of sight in Fig. 3.5. At high latitudes (top panel), this background tends to estimate higher counts than the maximum entropy background for $12 < K_s < 12.5$ and estimate fewer counts at $13 < K_s < 14$. At lower latitudes, this background tends to overestimate at all K_s, especially at around $K_s = 12.0$. On the simulation, the exponential background significantly over estimates in the range, $11.7 < K_s < 13.0$, as shown in the top panel of Fig. 3.11. As a result, the density is underestimated on the near side ($x < 0$) of the bulge at low latitudes when using the exponential background rather than the maximum entropy background in both the VVV data (Fig. 3.16) and simulated population (Fig. 3.17).

In Fig. 3.8, for the parametric fit, the exponential background (case C) has the worst TS both for the data and simulation, out of all of the cases considered in that figure. The TS was also high for both the data and simulation in the non-parametric case as shown in Fig. 3.18. This provides further evidence that the maximum entropy method is providing a better background than exponential model approach.

3.7.4 Luminosity Function Systematics

S17 found that the best-fitting luminosity function was significantly broader than the luminosity function they had simulated with GALAXIA (Sharma et al., 2011), using the same isochrones we have used in our analysis. We also tried a similarly broad luminosity function, by convolving our luminosity function with an additional Gaussian with a standard deviation of 0.24 mag. The density slices in the "Broad Φ" column of Figures 3.16 and 3.17 are consistent with the broadened luminosity function requiring a narrower and more angled bulge. A similar relationship can be seen in Fig. 16 of S17. In Fig. 3.8, the SX parametric model with broadened luminosity function (case D) had a slightly improved TS for the data, while it was disfavoured for the simulation. However, this broader luminosity function is not consistent with recent measured intrinsic RC magnitude dispersions (Hall et al., 2019; Chan et al., 2019). Also, in Fig. 3.6, the X-shape parameters, n and x_1, are anomalous for this case (case D). The consequence of this was that the broader luminosity function fit resulted in unnaturally narrow X-arms as depicted in Fig. 3.20. As can be seen in the non-parametric results of Fig. 3.18, the broader luminosity function (case D) provided a high TS for the

simulations indicating a bad fit. This is to be expected as the simulations were based on our standard narrower luminosity function. The TS for the data was so high for the broad luminosity function that we could not accommodate it in Fig. 3.18 without making the range of the plot too great to see any of the other details. This was because the non-parametric model was being heavily penalised for deviating greatly from the prior SX model, which had converged to a physically unnatural solution, shown in the top panel of Fig. 3.20.

Since our prior for the maximum entropy deconvolution was unnatural for the broad luminosity function, we wanted to check if a different prior gave similar results. So we repeated the test, but instead we used an S-model as the prior density, shown in the bottom panel of Fig. 3.20. As shown in Fig. 3.8, this S-model with a broad luminosity function (case I) was disfavoured by both the data and the simulation. However, as presented in Fig. 3.18, this case did not have a significantly larger TS for either the data or simulation when compared with the general range of TSs we see in the other cases. This indicates that at least from a TS perspective, our non-parametric results were not very sensitive to the width of the luminosity function.

3.7.5 Metallicity Distribution Systematics

Our base case assumed that the metallicity distribution is constant throughout the bulge. Several spectroscopic studies, e.g. Zoccali et al., 2017 and García Pérez et al., 2018, have observed a vertical metallicity gradient in the bulge, where stars near the Galactic midplane are on average more metal rich than stars on the periphery of the bulge. We used the photometric metallicity map generated by the BEAM-II calculator (Gonzalez et al., 2018) to allow the metallicity distribution function in the computation of our semi-analytic luminosity function to have a different mean metallicity for every line-of-sight. The metallicity dispersion was kept fixed at 0.4 for this test. Shown in Fig. 3.21 (top panel) is the metallicity map of Gonzalez et al., 2018, where we have filled the missing values with [Fe/H] = 0.0. From the luminosity functions in bottom panel of Fig. 3.21, it is clear that the lower metallicity line-of-sight has a fainter RC, and is naturally broader, though the difference in brightness is only 0.03 mag between $b = -9.1$ and $b = -3.1$. Some part of the broadness is from the overlapping of the RC and RGBB, since the RGBB is brighter at lower metallicities. Qualitatively, the density which was fitted using the metallicity gradient is nearly identical to the base case as seen in the last column of Fig. 3.16. The insensitivity to the metallicity gradient can be seen in case E of Fig. 3.8 and 3.18. The TS changes for the metalicity cases are

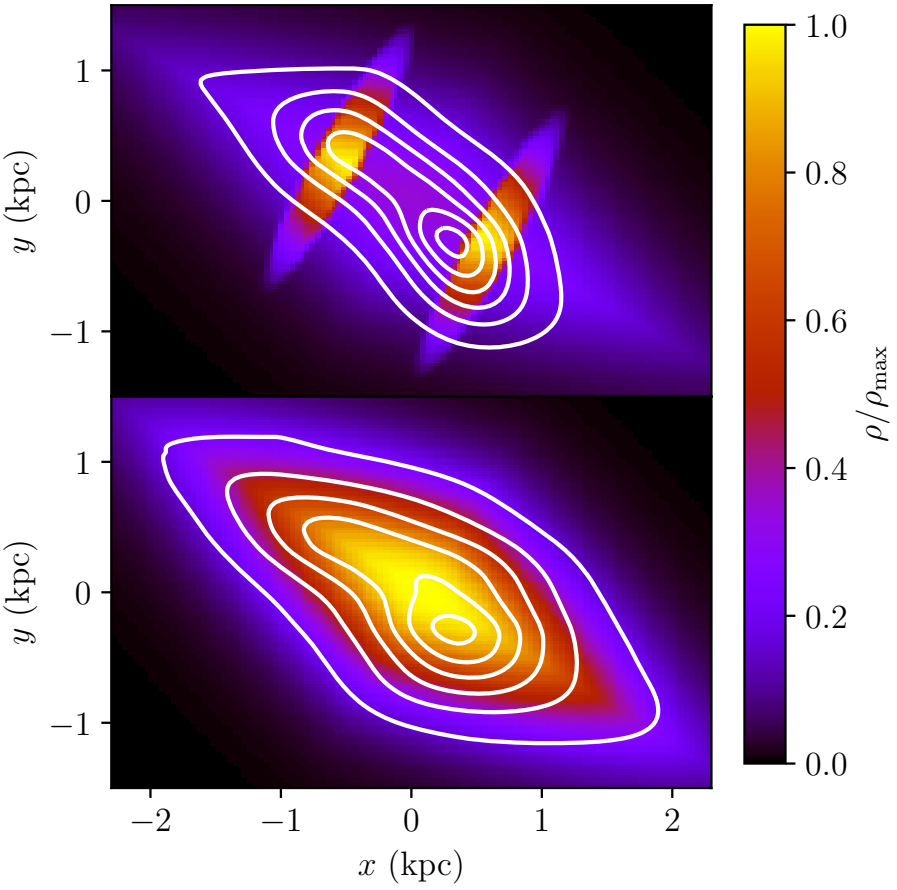

Fig. 3.20 SX (top) and S (bottom) parametric density models at $z = 0.495\,\mathrm{kpc}$, fitted to the VVV data using the 10 Gyr bulge PARSEC derived luminosity function that has been convolved with a Gaussian with $\sigma = 0.24$ (case D). They are used as the prior models for a non-parametric fit. The broadened luminosity function has driven the X-component to be unnaturally contrasting to the S component, which necessitates the non-parametric model (white contours) modulate significantly from the prior density. By contrast, the S-model is still largely visible in the non-parametric solution, with the modulated X-bulge arms visible at $x = \pm 0.5$

negligible in comparison to the TS changes associated with the other systematics. The E case does appear to have an anomalous x_1 in Fig. 3.6. However, as $A \approx 0$ for the E case, its X-component is negligible. We conclude from this test that the inclusion of a simple unimodal metallicity gradient does not significantly affect our results. A more sophisticated double population model, consistent with spectroscopic observations, is necessary to properly include a metallicity gradient.

3.7.6 Sun Position Systematic

Our simulated population of stars had the Sun located at $Z_\odot = 15$ pc, which is different to the $Z_\odot = 0$ pc assumed in our base model. We tested the significance of this assumption by fitting an S-model with the Sun in the same position as in our simulation (case F). We still assumed symmetry in the maximum entropy density about $b = 0°$. Fig. 3.8 shows how parametric case F provided a significantly improved fit to the simulation. This is to be expected as it corresponds with the model used to generate the simulation. In the case of the VVV data, it is harder to interpret the case F result in Fig. 3.8 as we have changed both the position of the Sun and the parametric form of the prior density. The difference between case F and case H is the position of the Sun, where both differ from the base case by having an S-model parametric form. The VVV data TS of case F was significantly larger than case H in the parametric case, however, there was less of a difference when fitting the parametric model to the simulation. This confirms that the VVV data significantly prefers $Z_\odot = 0$ pc when fitting the parametric S-model as seen in Fig. 3.18. When comparing the same cases, F and H, for the non-parametric method, case F had a significantly larger TS than case H for both the simulated population and the VVV data. It is hard to interpret this result for the non-parametric model, given that it had an assumed symmetry around the $Z_\odot = 0$ pc plane.

3.7.7 Deconvolution Method Systematic

Since our data differ from previous 3-D RC bulge studies in its photometry and completeness, we investigated how these changes are reflected in past methods applied to view the VVV RC. Given our semi-analytic formulation of a Ks-band luminosity function, we compare the results of past methods using different luminosity functions and backgrounds to our maximum entropy non-parametric density model. We continued to use the semi-analytic luminosity function derived in Section 3.3. We also used the

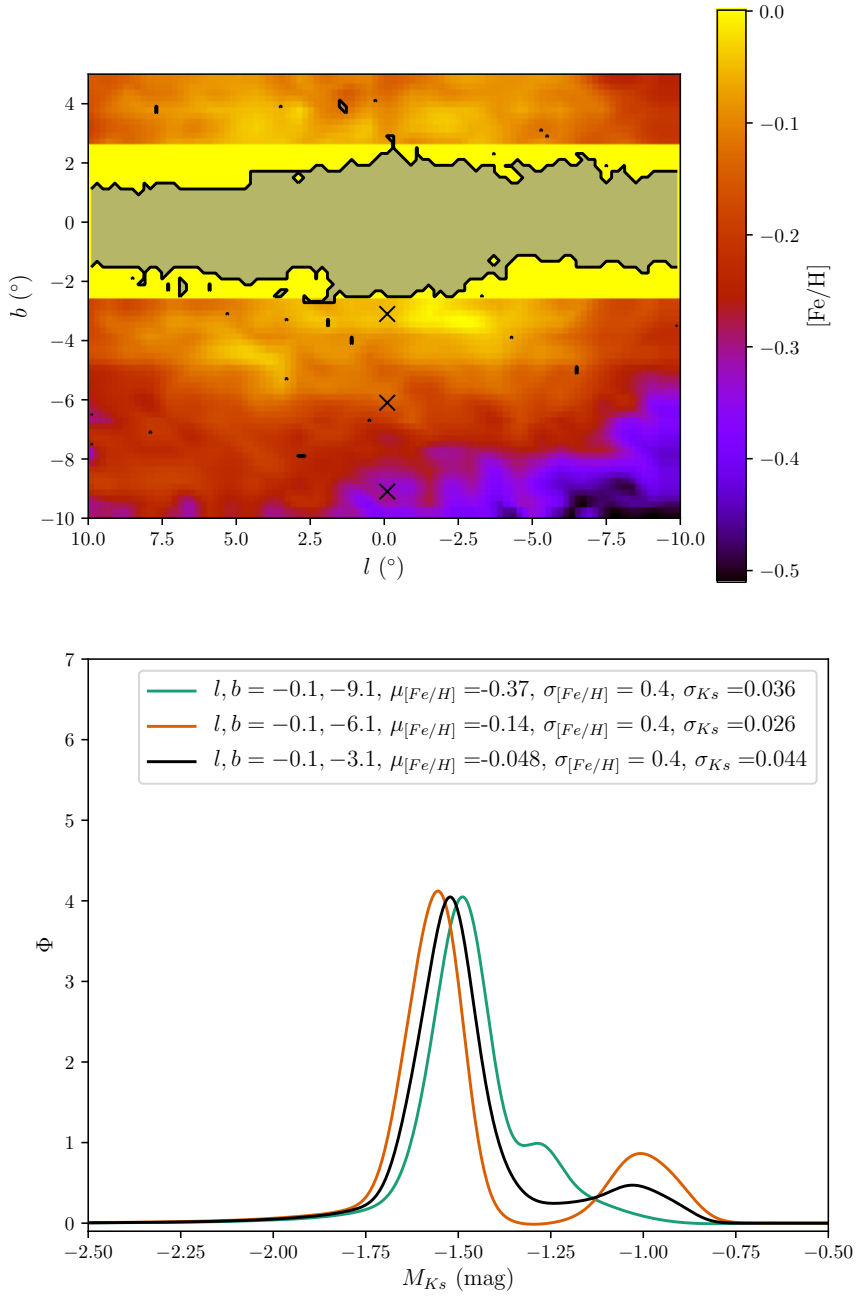

Fig. 3.21 *Top:* Mean photometric metallicity map, [Fe/H], of Gonzalez et al., 2018. Where the map does not have coverage at $|b| < 2.6$ we assume the fiducial value $\left[\text{Fe/H}\right]_{=0.0}$. The black crosses indicate the locations of the three luminosity functions plotted in the bottom panel. *Bottom:* The RC+RGBB luminosity functions for a range of fields of view, assuming a metallicity distribution as in the above panel. They have been convolved with a Gaussian with dispersion σ_{K_s}, the photometric uncertainty. In order of increasing metallicity, the mean absolute magnitude of the RC is -1.49 mag, -1.51 mag and -1.52 mag.

parametric function fitted to Monte Carlo simulations of WG13 (abbreviated as the BaSTI luminosity function). The WG13 luminosity function construction involved random draws of star masses from a Salpeter IMF and metallicity from the Baade's window metallicity distribution measured by Zoccali et al., 2008. Then, the K_s absolute magnitude was obtained from interpolated α enhanced BaSTI isochrones (Pietrinferni et al., 2004) assuming an age of 10 Gyr. The parametrisation of the WG13 BaSTI based luminosity function takes the form of the sum of two Gaussians corresponding to the RC and RGBB with parameters $\mu_{\mathrm{M_{Ks,RC}}} = -1.72$, $\sigma_{\mathrm{RC}} = 0.18$, $\mu_{M_{\mathrm{Ks,RGBB}}} = -0.91$, $\sigma_{\mathrm{RGBB}} = 0.19$ and relative fraction $f_{\mathrm{RGBB}} = 0.20$ (μ and σ taking their typical meanings in a Gaussian distribution). A notable difference here is that the RC dispersion is 3 times the width of our semi-analytic form, which is approximately 0.06 when fitting a Gaussian to the RC component.

As in WG13, we fitted a background of the form

$$B(K_s) = \exp(a + b(K_s - 13) + c(K_s - 13)^2) \tag{3.25}$$

to the magnitude ranges $11 \leq K_s \leq 11.9$ mag and $14.3 \leq K_s \leq 15$ mag for each line-of-sight. Several adjustments they recommended were retained for this background fit. Higher extinction and crowding in fields with $|b| < 2^\circ$ were accommodated by setting the second order coefficient, c, to 0 and restricting the upper fitted magnitude range to 14.5 mag. The bright latitude end magnitude range for regions where $l \geq 5.5^\circ$ was reduced down to $11 \leq K_s \leq 11.7$. The star count model for each field of view takes the form of Eq. 3.4, converted to the form of a background plus a linear convolution via the transform of line-of-sight distance (s) to distance modulus (μ). The luminosity function was convolved with the mean combined photometric and systematic uncertainty for each K_s along each line-of-sight to account for their effects. The VVV data was re-discretised into $\sim 1.5^\circ \times \sim 0.5^\circ$ spatial bins over 0.05 mag K_s bins. For each line-of-sight, the density distribution was initialised to a Hann window function over a distance modulus of 11.2 to 17, renormalised to the observed counts. We then applied the modified Richardson-Lucy procedure of WG13, retaining their stopping criteria, for both the BaSTI and PARSEC luminosity functions. This produced an estimate of the bulge density which depended on μ which we mapped onto a density which depends on s. We then reprojected the bulge density to Cartesian form using linear interpolation. For the low resolution data, step sizes of $(\Delta \mathrm{x} \times \Delta \mathrm{y} \times \Delta \mathrm{z}) = (0.15 \times 0.1 \times 0.075)$ kpc were used. This simple reprojection only produced a noisy unsymmetrised view of

the density model. For a view of the deconvolved bulge density assuming eight fold symmetry, the appropriate frame needs to be found.

We applied a process of finding the maximally eight fold symmetric frame following WG13. For each slice in the z direction, we carried out a simple grid search over distance to the Galactic centre R_0 and bar angle α, in steps of 0.02 kpc and 0.5 deg. For each α fixed, we shifted the bulge centre to some value of R_0 and computed the symmetrised density

$$\bar{\rho}(x, y, z) = \frac{1}{N} \left[\rho(x, y, z) + \rho(-x, y, z) + 6 \text{ other octants}\right] \tag{3.26}$$

where octant positions without matching densities in the (l, b, s) projection were ignored from the computation. Then the quantity

$$\frac{1}{\mathrm{N_z}} \sum_{z=0.4\mathrm{kpc}}^{1\mathrm{kpc}} \frac{\langle \rho_{\mathrm{rms}} \rangle_z}{\langle \rho \rangle_z} \tag{3.27}$$

was minimised, where N_z is the number of slices between 0.4 and 0.8 kpc in the chosen cartesian grid, so the quantity is comparable between resolutions. The parameter ρ_{rms} denotes the root mean square deviation between each octant's density in the symmetrisation and the average density, $\bar{\rho}$, of those points, which was then averaged across all points in each z-slice.

Rather than minimising Eq. 3.27 directly, $\langle \rho_{\mathrm{rms}} \rangle_z / \langle \rho \rangle_z$ was minimised over individual slices of z for our R_0 grid search. This was an intermediary step in the bar angle selection process to account for potential magnitude shifts in the model resulting from factors such as metallicity gradients, on top of the required shift in finding the maximally eight fold symmetric frame.

This process was then repeated for $0.2^\circ \times 0.2^\circ$ spatial bins using our maximum entropy derived background, described in Section 3.4.1, and Cartesian grid spacing adjusted to $(\Delta \mathrm{x} \times \Delta \mathrm{y} \times \Delta \mathrm{z}) = (0.04 \times 0.04 \times 0.03)$ kpc, to accommodate the finer data resolution.

In Fig. 3.22, we recovered the relation observed in S17, in which the broader BaSTI luminosity function results in a larger bar angle in comparison to the narrower PARSEC luminosity function. We note how the shift in R_0 for each slice to maximise eight fold symmetry is nearly flat with a constant shift in the BaSTI cases and a much shallower gradient than found by WG13 in our semi analytic PARSEC luminosity function cases. Figures 3.23 and 3.24 show our density deconvolutions on the data using the BaSTI

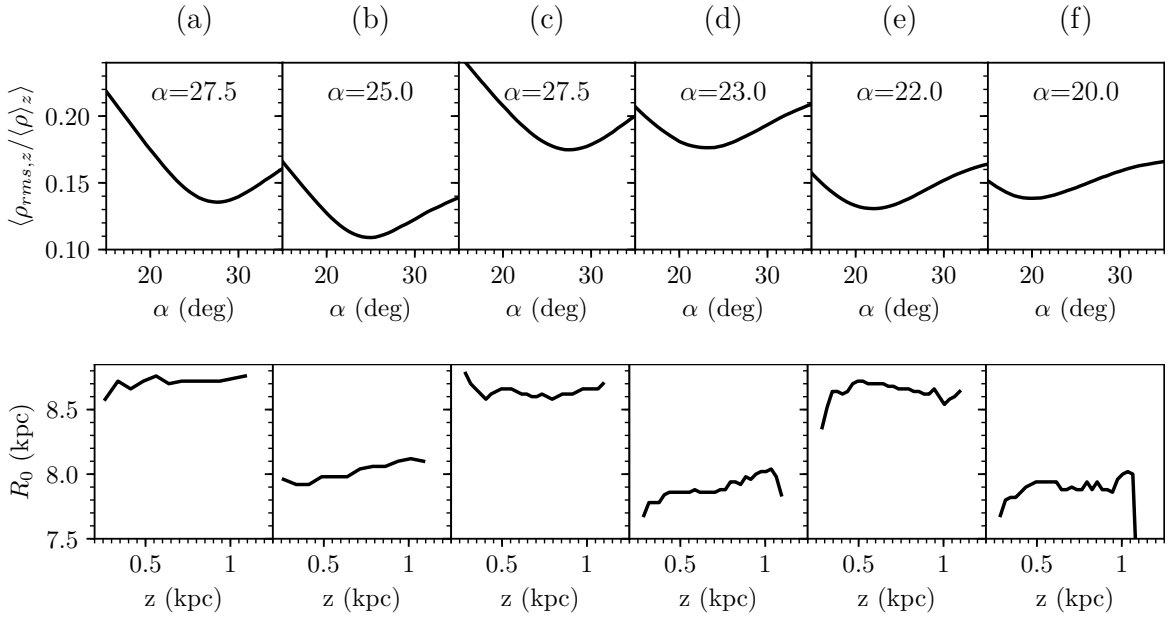

Fig. 3.22 Maximally eight fold symmetric angle (top) and R_0 (bottom) orientation of modified Richardson-Lucy deprojected data. From left to right: (a) BaSTI luminosity function on low resolution data (b) PARSEC luminosity function on low resolution data (c) BaSTI luminosity function on high resolution data (d) PARSEC luminosity function on high resolution data (e) BaSTI luminosity function on simulated data (f) PARSEC luminosity function on simulated data.

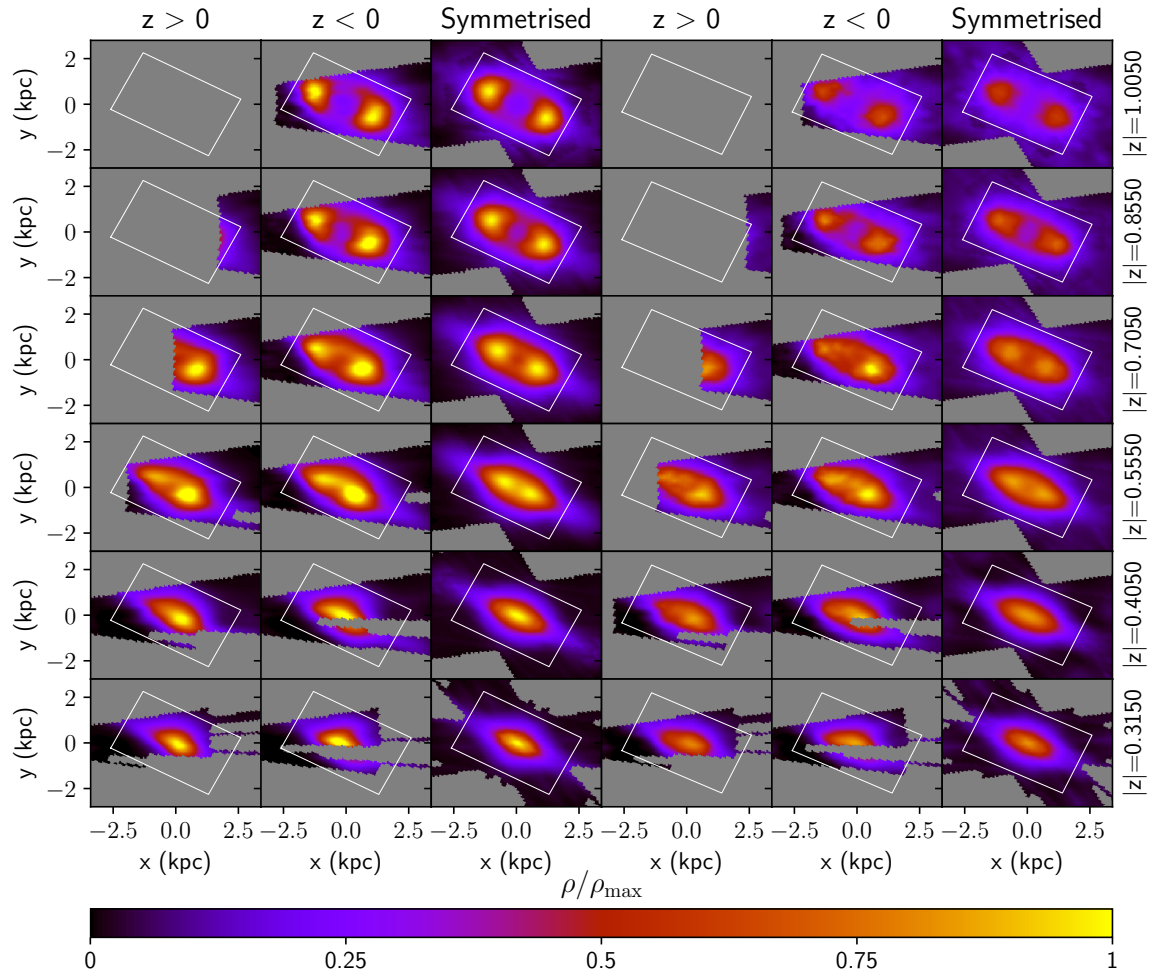

Fig. 3.23 Three-dimensional reconstruction of low-resolution VVV data. Columns 1-3 using BaSTI luminosity function and 4-6 using the PARSEC luminosity function. Slices of |z| normalised by the maximum of the BaSTI symmetrised model.

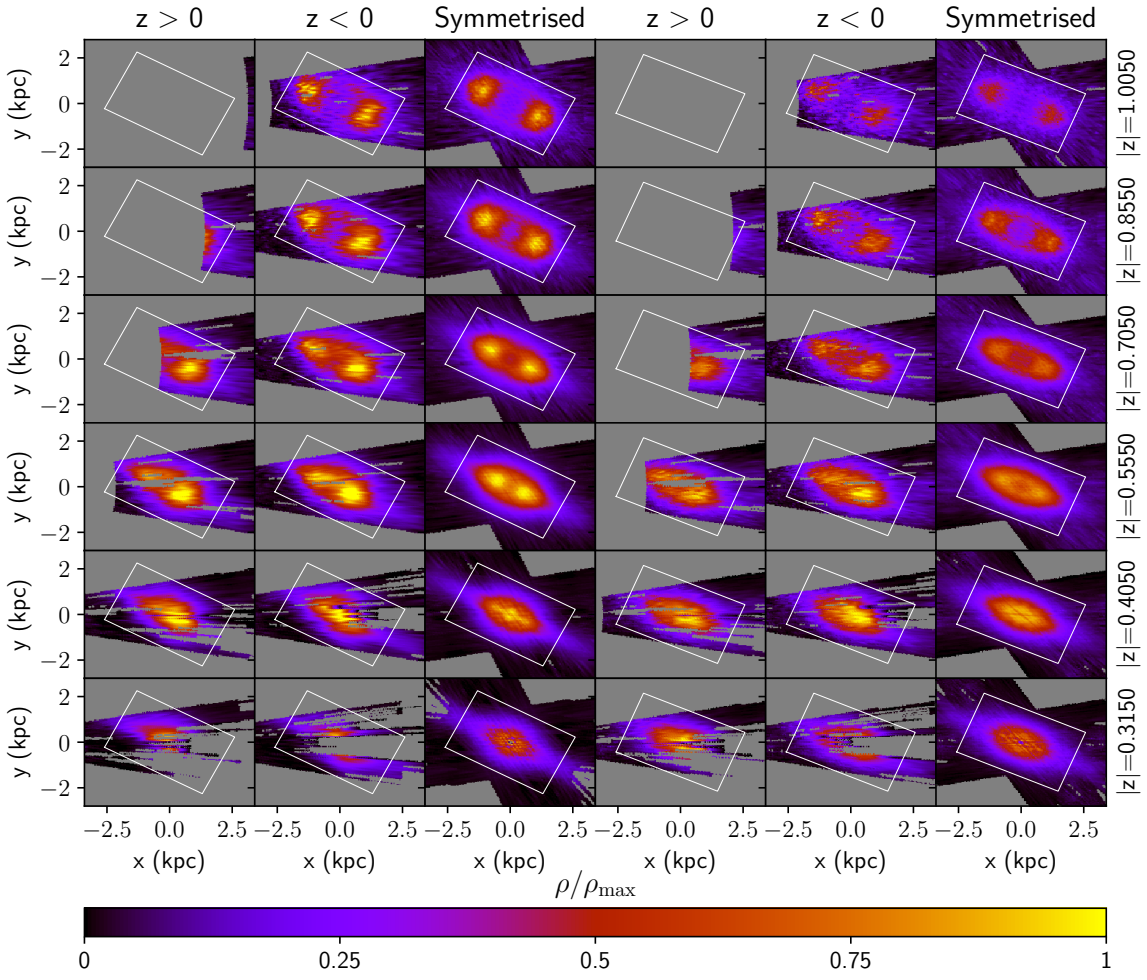

Fig. 3.24 Three dimensional reconstruction of high-resolution VVV data. Columns 1-3 using the BaSTI luminosity function and 4-6 using the PARSEC luminosity function.

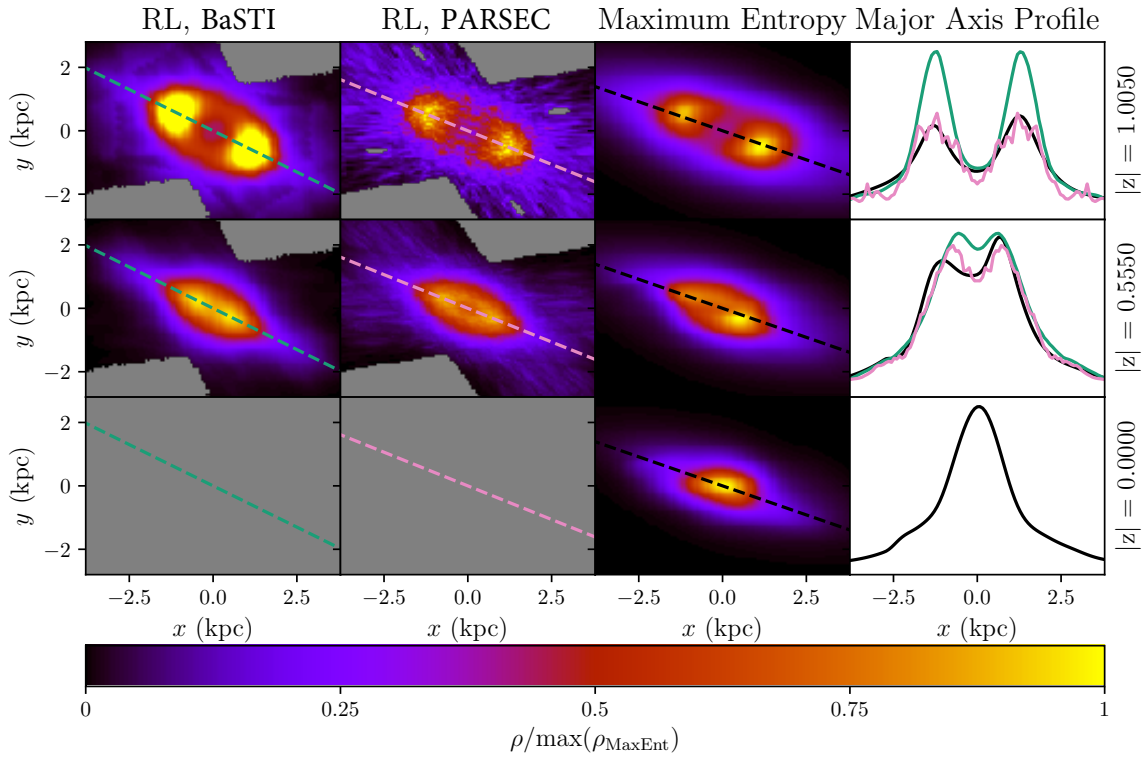

Fig. 3.25 Comparison between the modified Richardson-Lucy (RL) deconvolution and maximum entropy deconvolution. The left column implements the same method and resolution as WG13 except on our updated data set. The middle column is constructed in the same way as the left column except that the narrower PARSEC luminosity function is used instead of the BaSTI luminosity function used by WG13. Density slices have been normalised to the maximum value in the corresponding maximum entropy slice. The green, pink, and black profile plots in the fourth column are along the lines shown in column one, two, and three respectively.

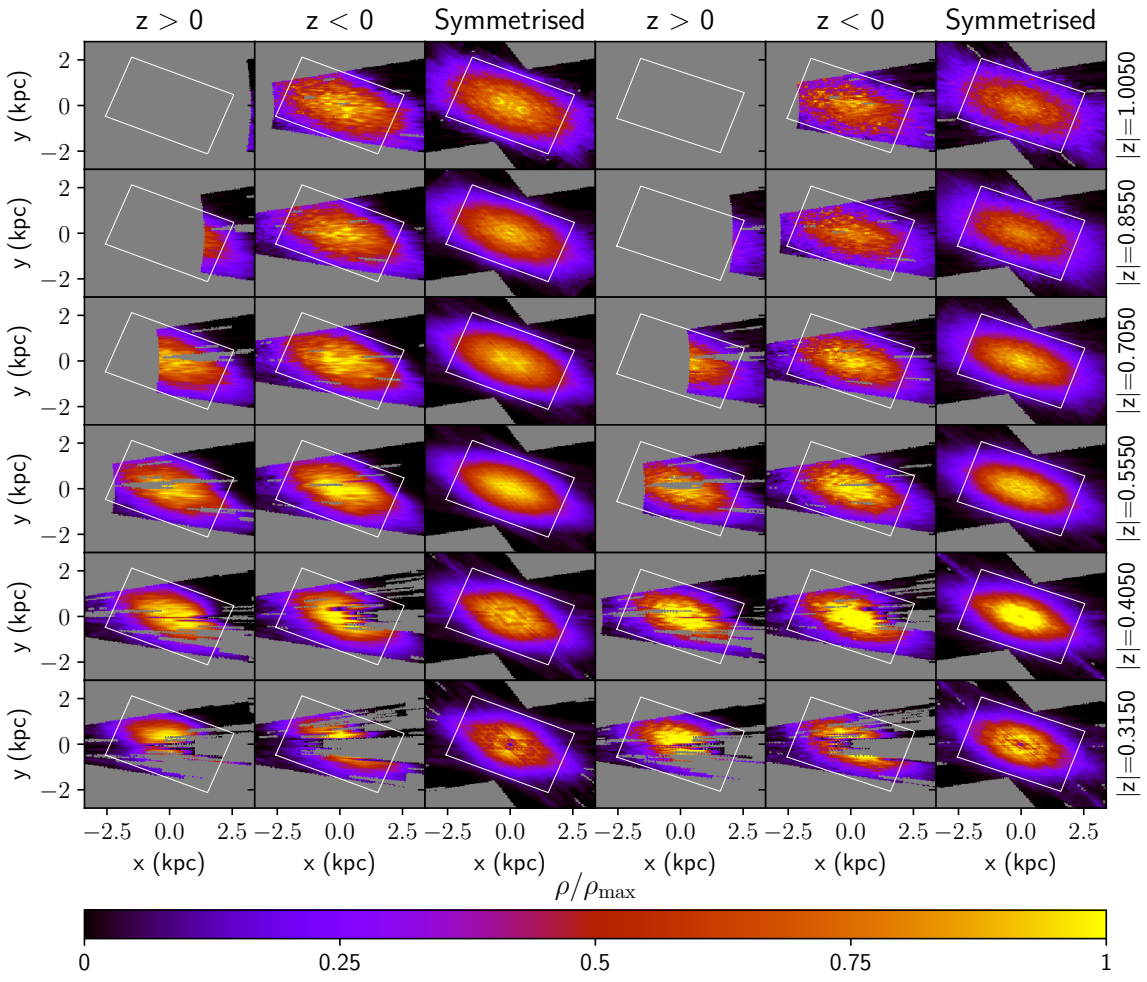

Fig. 3.26 Three dimensional reconstruction of S-model simulations. Columns 1-3 using BaSTI luminosity function and 4-6 using the PARSEC luminosity function.

and PARSEC luminosity functions across the two different resolutions we considered. The region used in the maximisation of eight fold symmetry, compatible with WG13, is bounded by a white rectangle. The X-bulge structure and features seen in WG13, such as the near-far RC density asymmetry, are visibly recovered. The K- and K_s-band RC magnitude widths being observed using *Gaia* DR2 of 0.03-0.09 mag (Hall et al., 2019; Chan et al., 2019) are consistent with the PARSEC luminosity function which is narrower than the BaSTI luminosity function.

In Fig. 3.25 we show a comparison between the modified Richardson-Lucy deconvolution and our non-parametric method. As can be seen from the profile plot in the right most panel, the modified Richardson-Lucy deconvolution with the BaSTI luminosity function has significantly denser X-arms at high $|z|$. However, this is primarily due to the use of the BaSTI luminosity function rather than the PARSEC luminosity function. If the PARSEC luminosity function is used with the modified Richardson-Lucy deconvolution (as in the second column) then the peaks are similar to our non-parametric deconvolution. However, the eight fold symmetry assumption forces the peaks to be the same height whereas our non-parametric method finds the peak closer to the Sun to be less dense. But, as can be seen from the second column, of the figure, when the PARSEC luminosity function is used with the modified Richardson-Lucy deconvolution, a much noisier reconstruction is obtained even though the low resolution case is being used. The PARSEC luminosity function has an intrinsic RC dispersion that is more consistent with observations (as mentioned above). It is distinct advantage that our non-parametric model can give non-noisy reconstructions with the narrower PARSEC luminosity function at higher resolution. We checked the method against simulations for the finer resolution to examine possible shortcomings in that regime independently of the actual data.

In Fig. 3.26 we show the results of the deconvolution and symmetrisation of the simulated data with our standard $0.2^\circ \times 0.2^\circ$ resolution. The bar angle was effectively recovered using 0.5° steps in a grid search for the PARSEC luminosity function case and a larger angle using the broader BaSTI luminosity function as seen in our earlier results and also by S17. The shift in R_0 is mostly flat across z slices in both cases with a slight negative gradient in the BaSTI case. Comparing to the gradient in the data fits, it is not apparent whether or not these comparably shallow gradients are spurious. The R_0 eight fold symmetric maximisation on the data results in a very flat shift in R_0 across z slices between 400 and 800 pc. Above 800 pc the counts are very low at this resolution, causing excessively noisy features and below 400 pc our

mask starts interfering substantially with the symmetrisation procedure. We find a negligible gradient using the broader BaSTI derived luminosity functions. It is not clear within this method how one might interpret the apparent magnitude-shift gradient depending on the broadness of the luminosity function seen here and how much of it is an artefact of the symmetrisation, when there is a persistent asymmetry at odds with the assumption of eight fold symmetry. Our metallicity distribution systematic above for comparison, found unimodal corrections driven by observation were negligible.

3.8 Applications

3.8.1 Properties of the Bulge

Mass of the bulge

From the fitted density and IMF we can estimate the total mass of the bulge. Integrating the RC+RGBB stellar density over the entire bulge region gives us a total of 19.1×10^6 (RC + RGBB) stars. Based on our luminosity function, 0.062 % of all stars are in either the RC or RGBB, so the total number of stars in the bulge is $N_{\rm total} = 30.7 \times 10^9$. Stars in the bulge with a mass $>1 M_\odot$ have evolved into stellar remnants, so the normalisation of the IMF is then given by

$$\xi_0 = \frac{N_{\rm total}}{\int_{0.15\,M_\odot}^{1\,M_\odot} \xi(m)\,{\rm d}m}, \tag{3.28}$$

where ξ is the IMF and ξ_0 is the normalisation of the IMF. We use the Chabrier IMF, which was also used to generate our luminosity function. With the IMF correctly normalised, the mass of the bulge is then calculated by integrating the IMF multiplied by the final mass of the star, over the range $0.15\ M_\odot < m < 150 M_\odot$. Stars with an initial mass $< 1 M_\odot$ have not yet evolved into remnants, so the final mass is equal to the initial mass. Stars with initial mass $1 M_\odot < m < 8 M_\odot$ have evolved into white dwarfs, where the final mass is related to the initial mass by $m_f = 0.48 + 0.077 m_i$ (Maraston, 1998). To determine the final mass stars with initial mass $> 8 M_\odot$, which have evolved into neutron stars or black holes, we use the results of the numerical population synthesis code SEVN (Spera et al., 2015). The normalised IMF is shown in Fig. 3.27. Therefore, the total stellar mass of the bulge (assuming a Chabrier log-normal IMF) is $M_{bulge} = 1.64 \times 10^{10}\, M_\odot$. This includes the mass of the stellar remnants, which make up 30.1% of the total mass.

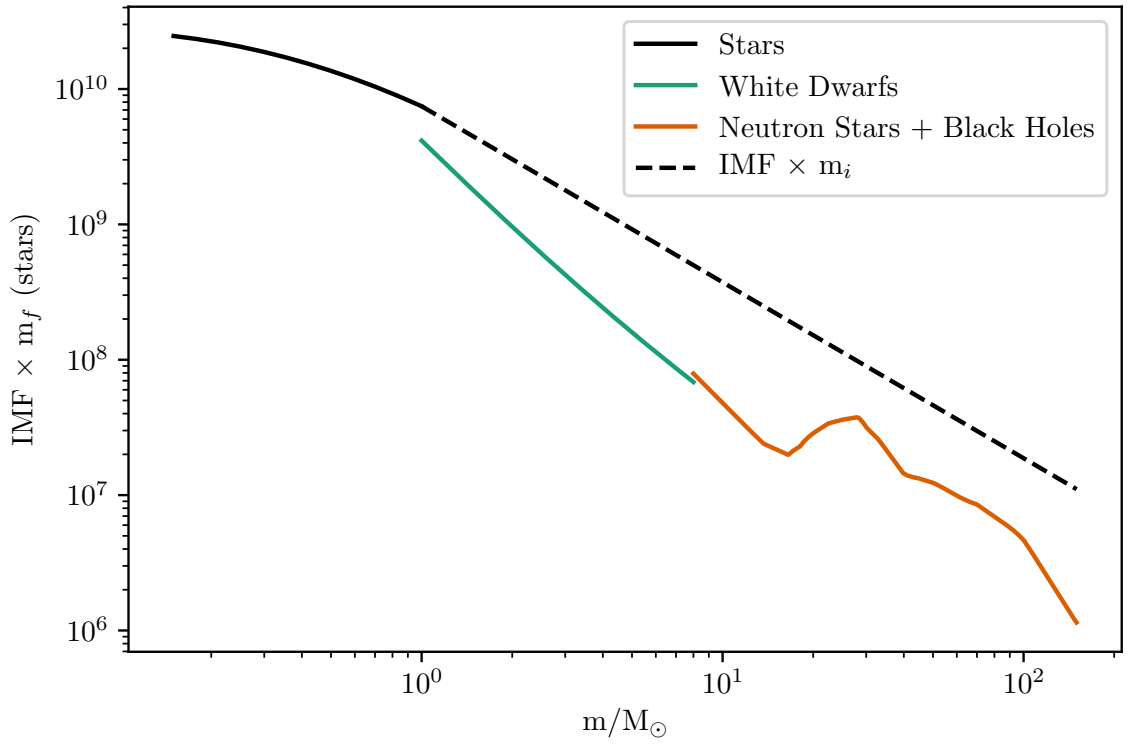

Fig. 3.27 Normalised initial mass function multiplied by the final mass of the star. Stars that have evolved into compact remnants, white dwarfs (green line) or neutron stars/black holes (orange line), lose mass during the later stages of their evolution, so they have a lower IMF × m than their initial mass would predict (black line).

Parametric modelling of VVV bulge stars in S17 found a total stellar mass of the bulge assuming a Chabrier IMF of $2.36 \times 10^{10} M_{\odot}$, with the stellar remnants making up 49% of the total mass. Both the total mass and remnant fraction of S17 are larger than we are reporting. However, if we were to have the same remnant fraction as S17, then our total mass would be $2.24 \times 10^{10} M_{\odot}$.

A dynamical estimate of the bulge mass by combining the VVV bulge stellar distribution of WG13 with kinematic information from BRAVA in Portail et al., 2015 found a bulge stellar mass of 1.3-1.7$\times 10^{10} M_{\odot}$, which is consistent with our estimated mass. They also provide a mass-to-clump ratio, which can be used to estimate the total stellar mass of the bulge from the number of RC+RGBB stars. For a Chabrier IMF, there are approximately $905 M_{\odot}$ of bulge mass for each RC+RGBB star. So for our estimated 19.1×10^{6} (RC+RGBB) stars the estimated mass was $1.73 \times 10^{10} M_{\odot}$. This is remarkably similar to our value, considering Portail et al., 2015 used different isochrones, metallicity distribution, and treatment of the compact remnants to those used in our estimation. Additionally, we list the bulge mass estimates for all of our systematic test cases in Table 3.8. The mass estimates of the simulated data encompass the mass of the model used for the simulation with a spread of a few percent. Also, the mass estimates for the bulge from the VVV data are in the range 1.33-1.71 $\times 10^{10} M_{\odot}$, which is in agreement with the results of Portail et al., 2015.

Distance to the Galactic centre

As mentioned previously, we associate the Galactic centre with the location of the maximum density of the bulge. In all cases we examined, this maximum bulge density was in the same location for the parametric and non-parametric fit. According to our base non-parametric model, the distance from the Sun to the Galactic centre is 7.9 kpc, where the assumed mean absolute magnitude of the RC is $\mu_{M_{Ks},RC} = -1.53$. If we had instead used the observed local RC mean magnitude of $\mu_{M_{Ks},RC} = 1.62$ (Chan et al., 2019; Hall et al., 2019), then all distances would be increased by a factor of 1.04. With the brighter RC, the distance to the Galactic centre would then be 8.24 kpc, which is consistent with the recent measurement of 8.18 ± 0.04 kpc calculated using parallax observations of Sgr A* (Gravity Collaboration et al., 2019). Our value is also consistent with 8.2 ± 0.1 kpc of Bland-Hawthorn et al., 2016, who combined estimates from eight independent methods.

Table 3.8 Total stellar mass estimate for the Galactic bulge for all test cases. A Chabrier IMF was assumed, which gave a remnant fraction of 30.1% The cases considered are: base (A), no behind the bar feature subtraction (B), exponential background (C), broad luminosity function (D), metallicity gradient (E), S-model prior with $Z_\odot = 15$ pc (F), S-model prior and broad luminosity function with $Z_\odot = 15$ pc (G), S-model prior with $Z_\odot = 0$ pc (H), S-model prior with $Z_\odot = 0$ pc with a Broad luminosity function (I). The mass of the simulated stellar population is $\mathrm{Mass}^{\mathrm{Sim}}_{\mathrm{Bulge}} = 1.92 \times 10^{10} M_\odot$.

Case	$\mathrm{Mass}^{\mathrm{VVV}}_{\mathrm{Bulge}}$ ($\times 10^{10} M_\odot$)	$\mathrm{Mass}^{\mathrm{Sim}}_{\mathrm{Bulge}}$ ($\times 10^{10} M_\odot$)
A	1.64	1.89
B	1.70	1.92
C	1.33	1.84
D	1.61	1.90
E	1.63	1.89
F	1.52	1.91
G	1.58	1.93
H	1.53	1.92
I	1.57	1.93
J	1.71	1.90

Table 3.9 Ratios given by the X component of each corresponding model integrated in all directions down to a scalar divided by overall integrated SX model, for data and simulation fits.

	A	B	C	D	E	J
Data	0.23	0.23	0.18	0.25	0.24	0.92
Simulations	0.20	-0.0062	-0.048	0.012	0.018	0.016

Estimating the X-component proportion

The X component was obtained by setting the 1 in $(1+A)$ from the SX model definition in Eq. 3.12 to 0. The X-component proportion was then computed by integrating the X component and SX model over all coordinates and then taking the ratio of them. These ratios are listed in Table 3.9.

A partial degeneracy in the SX model, due to allowing the X-arm power law exponent (n) to vary, turns up in our extinction mask parametric fit (case J) to the data. The additional density unveiled by the extinction mask depicted in Fig. 3.19 may be the main driving factor in this behaviour, which only showed up in that model case. The result of this is visible in Fig. 3.6, where the J case is an outlier in the A and n parameters. With an exponent, n, less than 1, the X-arms become very broad. This case is not shown in Fig. 3.8 because it involves a different amount of data, so the

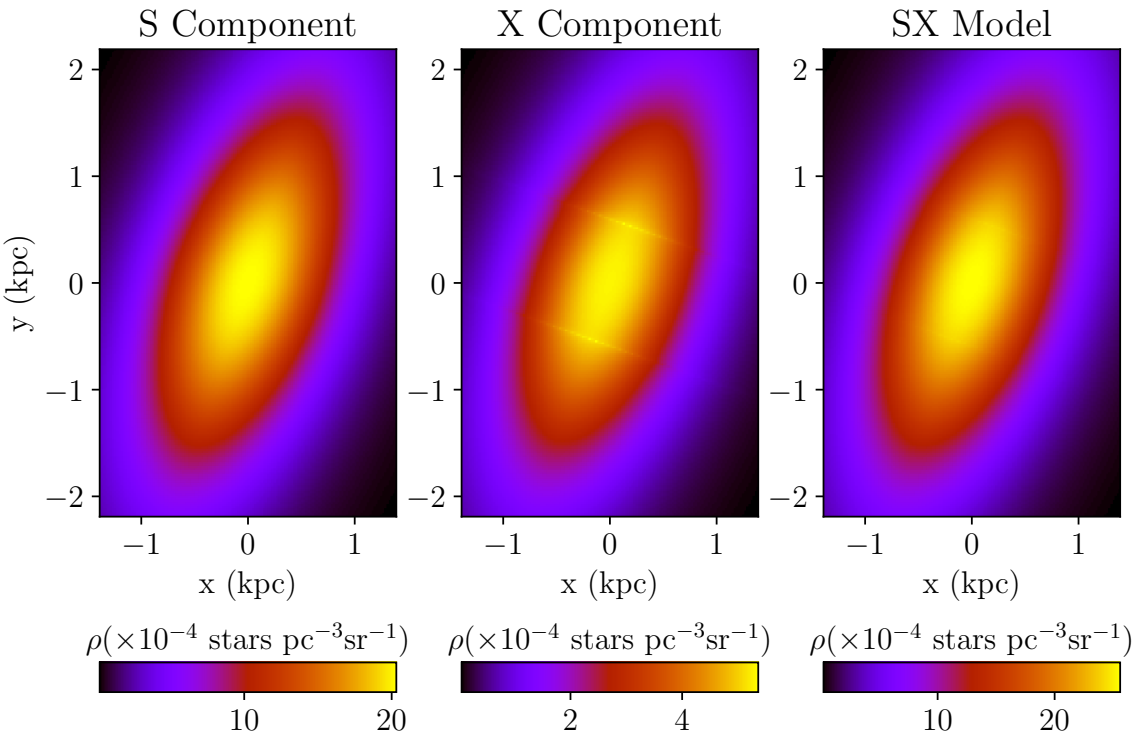

Fig. 3.28 Sample slice at $z = 310pc$ of the parametric model in case A, fitted to simulations. A simple ratio of the X component to the full SX model can imply there is a significant X-arm component when there isn't one. Due to the very small exponent $n \sim 0.02$, the X component has effectively the same shape as the S component only with small cusps at the origins of the exponential functions.

change of likelihood will be on a different scale to that in the other cases. Another case of A and n replacing the bulk of the S component of the SX model is in parametric case A on the simulations. A slice near the edge of the Galactic plane data mask, at 310 pc, is displayed in Fig. 3.28.

As the parameter n approaches 0, the perturbation tends towards a constant with a cusp at the X-arm origins from the exponential term. Although this model can appear to have a strong X component, the fact we have $n \ll 1$ tells us that this component is near constant, so it is effectively adding to the normalisation of the S component rather than giving an X shaped perturbation. This result could in principle have come out for any of the simulation cases, so this behaviour is not particular to the A model, just the random model initialisation that resulted in a convergence to a model that has the X component trace the bulge rather than, for example, fall below the mask by having a large X-arm parting factor C.

Based on the above arguments we discard the J case parametric estimate for the simulation and the A case parametric result for the data in Table 3.9. It follows that our simulation results are consistent with a negligible X-component which is correct as the model used to generate the simulation had no X-component. Additionally, we can conclude that our parametric fit to the data has the X-component contributing a range of 18% to 25% to the bulge mass. This estimate of the X-bulge component contribution is consistent with that found for the WG13 model by Portail et al., 2015 which was 24%.

Bulge angle

As can be seen from Table 3.2 our bar angles (α) for the simulation ranged from 19.1° to 29.3° which encompasses the simulated value of $\alpha = 19.2°$. As can be seen from Table 3.1 our parametric fit of the VVV data had bulge angles in the range of 18° to 32°. This is consistent with previous estimates. E.g. WG13 obtained a best fit of 27° and S17 obtained a best fit of 20°.

3.8.2 Gamma Ray Galactic Centre Excess

The work of Macias et al., 2019 found the S-bulge model (denoted by F98S hereafter) from Freudenreich, 1998 provided the best fit to the *Fermi* GCE in a template fitting analysis. We created a template from our base parametric model and our non-parametric model fitted to the VVV data for comparison with quality of the F98S template fit. We assumed that the density of MSPs is spatially correlated with the RC stellar density. The template (T) for the *Fermi-LAT* analysis needs to be proportional to the expected flux of the MSPs, so it was constructed using:

$$T(l, b) = \int_s \rho(s, l, b)\, \mathrm{d}s, \tag{3.29}$$

where ρ is, as before, the RC+RGBB stellar density of the bulge. We show a comparison between the F98S template and templates generated from our parametric and non-parametric fits in Fig. 3.29. Our non-parametric template has a noticeable "peanut" like morphology. This may at first seem in contrast to the X-shaped morphology apparent from Fig. 3.16 for example. However, in that figure each slice in z is normalized by the maximum density in that slice. As is well known, when no such normalization is done the bulge has a more peanut morphology as can be seen from the third panel of the cross-sections in Fig. 3.30.

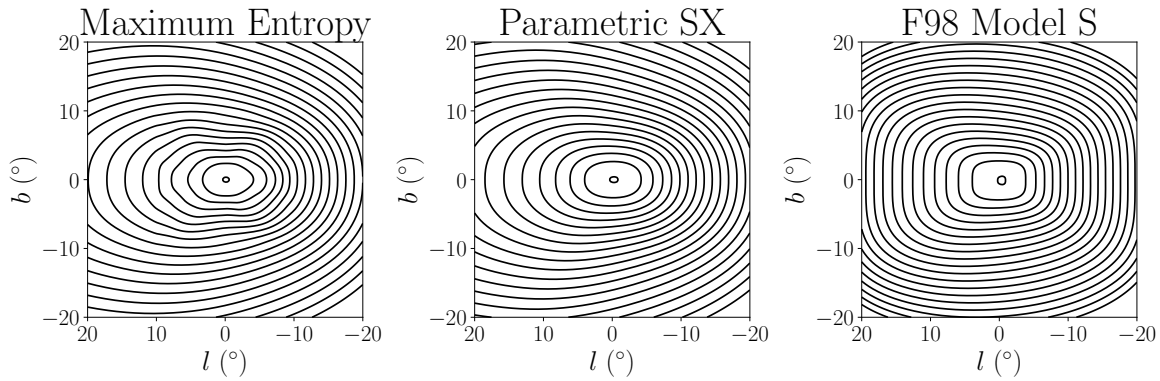

Fig. 3.29 Integrated density, $T(l,b) = \int \rho(s,l,b)\,\mathrm{d}s$, for the maximum entropy deconvolution, the parametric SX prior density for the deconvolution and the parametric S-model of Freudenreich, 1998.

In fitting to the *Fermi*-LAT data, we followed the same method as Macias et al., 2019. The bulge template was fitted simultaneously with the resolved point sources, gas correlated templates, inverse Compton templates (ICS-F98SA50) (Porter et al., 2017), *Fermi* bubbles templates, and Sun/Moon templates. The energy range of the photons used in the *Fermi-LAT* analysis was 667 MeV to 158 GeV, distributed over 15 logarithmically spaced energy bins. A $40° \times 40°$ region around the Galactic centre was used with $0.5° \times 0.5°$ pixels. This large region of interest was necessary to be able to constrain the background components. Also, no mask was used in the *Fermi-LAT* analysis. This made our non-parametric method of estimating the bulge from the VVV data particularly suitable as it allowed us to obtain an estimate of the bulge morphology over a $40° \times 40°$ area with no masked regions.

We evaluated the improvement to the fit to the *Fermi-LAT* data by working out $\mathrm{TS}_{\mathrm{Fermi}} = 2\ln\mathcal{L}_{\mathrm{null}} - 2\ln\mathcal{L}_{\mathrm{bulge}}$ where $\mathcal{L}_{\mathrm{null}}$ is the maximum likelihood with all the above mentioned templates' normalisations treated as free parameters in each of the 15 energy bands. $\mathcal{L}_{\mathrm{bulge}}$ is the maximum likelihood estimate using all the above mentioned templates and the the bulge template where the template normalisations were all fitted simultaneously. As discussed by Macias et al., 2019, a $\mathrm{TS}_{\mathrm{Fermi}} \geq 34.8$ corresponds to a 4σ detection of a new extended source. In Table 3.10, we list the change in $\mathrm{TS}_{\mathrm{Fermi}}$ for the different bulge templates we considered. The non-parametric template was preferred by the *Fermi-LAT* data, with $\Delta\mathrm{TS}_{\mathrm{Fermi}} = 177$ compared to the previous best-fitting template, F98S. A similar values was obtained when using a S-model fitted to the VVV data instead of F98S. Compared to our parametric SX template, our non-parametric template had $\Delta\mathrm{TS}_{\mathrm{Fermi}} = 65$. Each successive enhancement in our

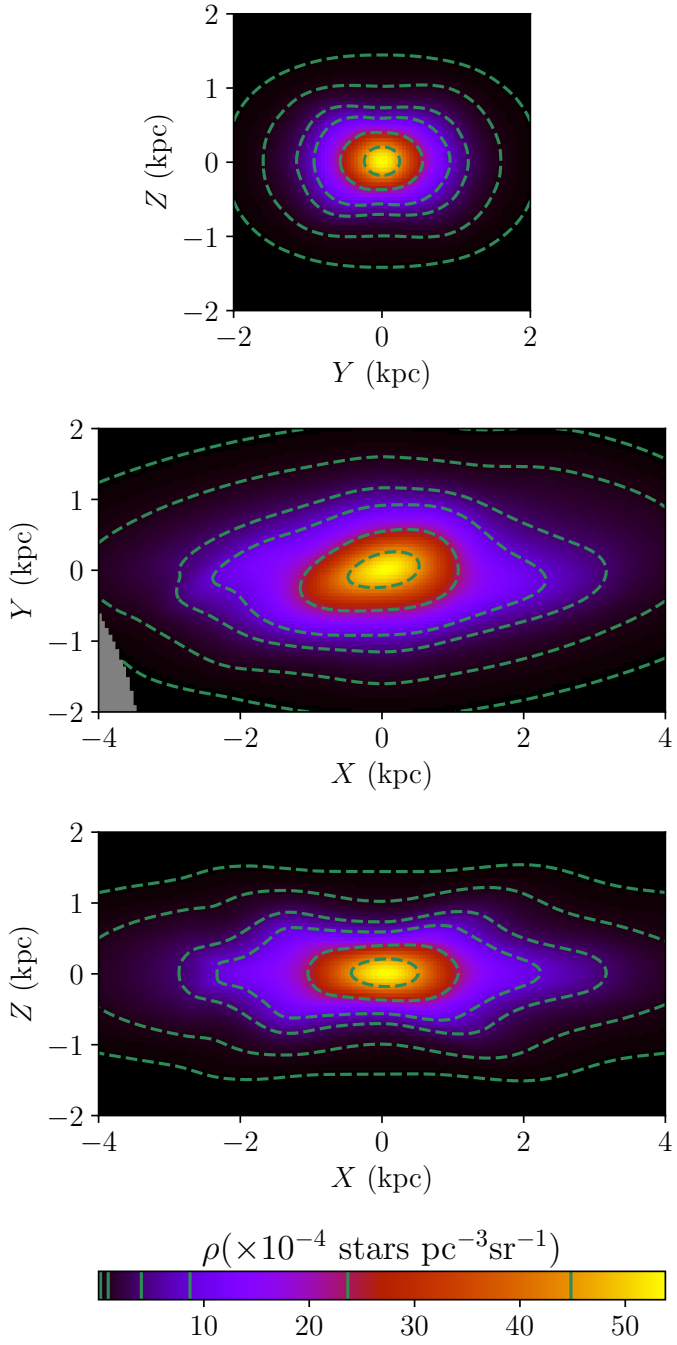

Fig. 3.30 Slices at the Galactic centre of the stellar density across different axis slices for our base non-parametric model. The 3 perpendicular axes are aligned along the bar angle and centre using α and ΔR_0 from our best fitting parametric model for the base case. The coordinate X is along the main axis of the bar and Z is perpendicular to the Galactic plane.

bulge model, from S to SX to non-parametric, resulted in a steady improvement in the quality of fit to the *Fermi* data. This provides further evidence that the GCE traces the stellar content of the Galactic bulge.

Contour plots of the data and two alternative models are shown in Fig. 3.31. The improvement of the fit when the Galactic bulge component is included is particularly noticeable around $(l, b) = (5°, -5°)$. The contribution of the Galactic bulge to the *Fermi-LAT* model fit is shown in Fig. 3.32. The peanut nature for the bulge shape is evident in this figure, even after accounting for the PSF smoothing of the *Fermi-LAT* instrument. Around the $l = 5°$ region there is a larger ratio of bulge to total signal than in other longitudes displayed. This helps in explaining why that area has one of the most noticeable improvements in fitting to the gamma ray data presented in Fig. 3.31. Also, this figure shows how typically the bulge component is an order of magnitude smaller than the overall signal. This makes it hard to assign a statistical significance to the difference in $\Delta\mathrm{TS}_{\mathrm{Fermi}}$ values seen in Table 3.10, as small errors in the larger components could cause one template to be preferred over the other. One alternative method to account for this complication may be to use a maximum entropy non-parametric approach to modulate the larger components as handled by the SkyFACT method (Storm et al., 2017), which also found a preference for a boxy bulge model of the GCE in the *Fermi-LAT* data (Bartels et al., 2018).

Shown in Fig. 3.33 are the gamma ray spectra for the NB + F98 model and the NB + non-parametric bulge model. Included for comparison in this figure are the NB + boxy bulge models from Bartels et al., 2018 (hereon referred to as B18 boxy bulge) and Macias et al., 2018 (M18 boxy bulge). The spectra of the F98 and non-parametric bulge models generally agree well with the B18 and M18 boxy bulge models. The spectrum of M18 boxy bulge model is slightly harder and overall more luminous than the other three spectra.

The B18, F98 and non-parametric models all offer an improved method of modelling the foreground/background gamma ray emission than the the M18 model. In the case of the F98 and non-parametric model, the template of the *Fermi* bubbles has been improved from a flat catenary to a structured and inpainted template (Macias et al., 2019). Also, the region of the sky studied is significantly larger at $40° \times 40°$ compared to $15° \times 15°$ as in the M18 boxy bulge, which offers more constraining power to the foreground/background emission from high latitude observations. For the B18 boxy bulge model, an even larger region of the sky was analysed ($180° \times 40°$) and the spatial template of the foreground models are able to modulate. This demonstrates that the

Table 3.10 A comparison of the different bulge templates ability to explain the *Fermi-LAT* GCE. For model i, we list $\Delta\mathrm{TS}_{\mathrm{Fermi}} = 2\ln\mathcal{L}_{\mathrm{nonparam}}/\mathcal{L}_i$.

Model	$\Delta\mathrm{TS}_{\mathrm{Fermi}}$
Non-parametric bulge	0
SX bulge	65
S-bulge	177

GCE spectrum is more sensitive to the modelling of the larger foreground/background components than the accuracy of the GCE spatial template.

3.9 Spiral Arms Revisited

In Section 3.4.1 we demonstrated that our maximum entropy method was able to detect the spiral arm structure behind the bar. In this section, we relax some of the assumptions made in the previous sections to see if a spiral arm feature is also visible in front of the bar. For this analysis we are not interested in extending the bulge density outside of the field of view of the VVV observations, so we dropped the assumption that the density smoothly reconnects to the prior density outside the field of view, and no longer assumed the bulge density is symmetric about the Galactic midplane. We directly accounted for stars in the foreground disk and non-RC bulge red giants with the model

$$N\left(K_s,l,b\right) = N_{\mathrm{thin}}\left(K_s,l,b\right) + N_{\mathrm{thick}}\left(K_s,l,b\right) + \Delta\Omega\Delta K_s\int_4^{13}\rho\left(s,l,b\right)\Phi\left(K_s - 5\log s - 10\right)s^2\,\mathrm{d}s, \quad (3.30)$$

where N denotes total number of stars in a voxel centred at (K_s, l, b). This is made up of contributions from the the thin disc (N_{thin}), thick disc (N_{thick}), and a contribution given by a weighted integral of the Galactic bulge number density (ρ). The $\Delta\Omega$ denotes the solid angle subtended by the line-of-sight, ΔK_s denotes the width of a K_s magnitude bin, and and s denotes the distance from the Sun measured in kpc. An example of the the broadened luminosity function (Φ) is shown in Fig. 3.3. We chose the integration range 4 kpc $\leq s \leq$ 13 kpc as the Galactic bulge density is negligible outside that region.

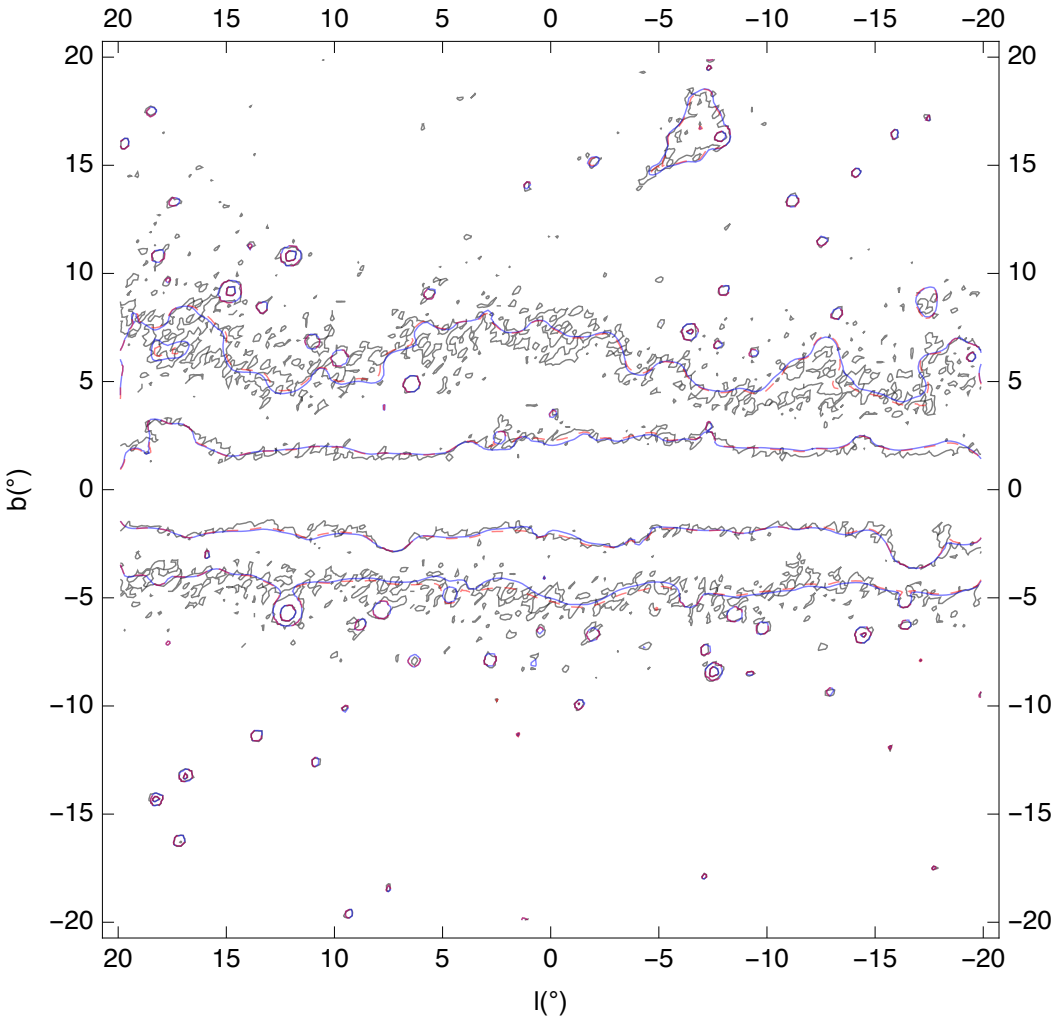

Fig. 3.31 Contours of the *Fermi-LAT* data (black), a model without a Galactic bulge (blue), and model with our non-parametric Galactic bulge (red, dashed). The energy range is 1.1 to 2.8 GeV and the contour levels are 750 and 2000, in units of photons per square degree.

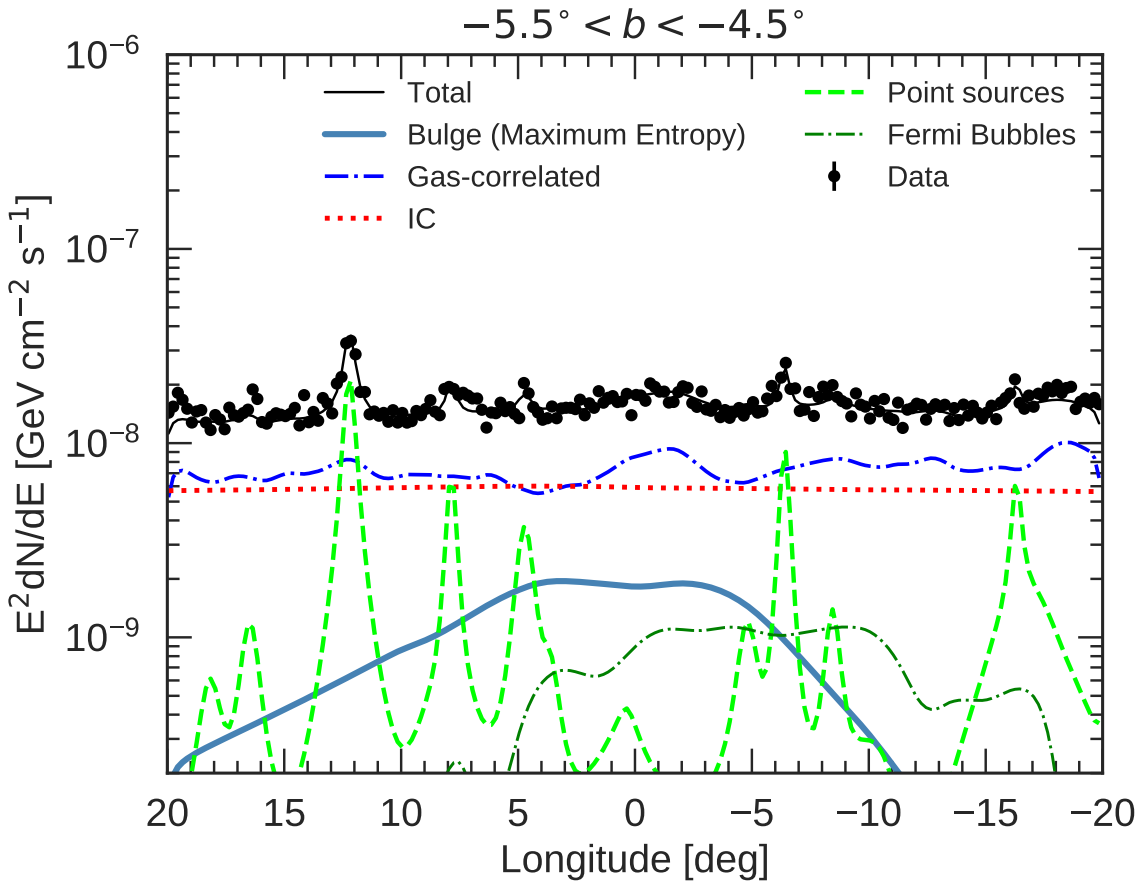

Fig. 3.32 Spatial distribution of the main model components included in the *Fermi-LAT* fit. The flux profiles in the energy range $[1.1, 2.8]$ GeV are displayed. Black dots represent the data and the continuous black line the total best-fitting model. Other components not shown here (*e.g.,* isotropic, Sun, Moon and Loop I) are $\sim \mathcal{O}(1)$ less bright in the region used to construct the profile.

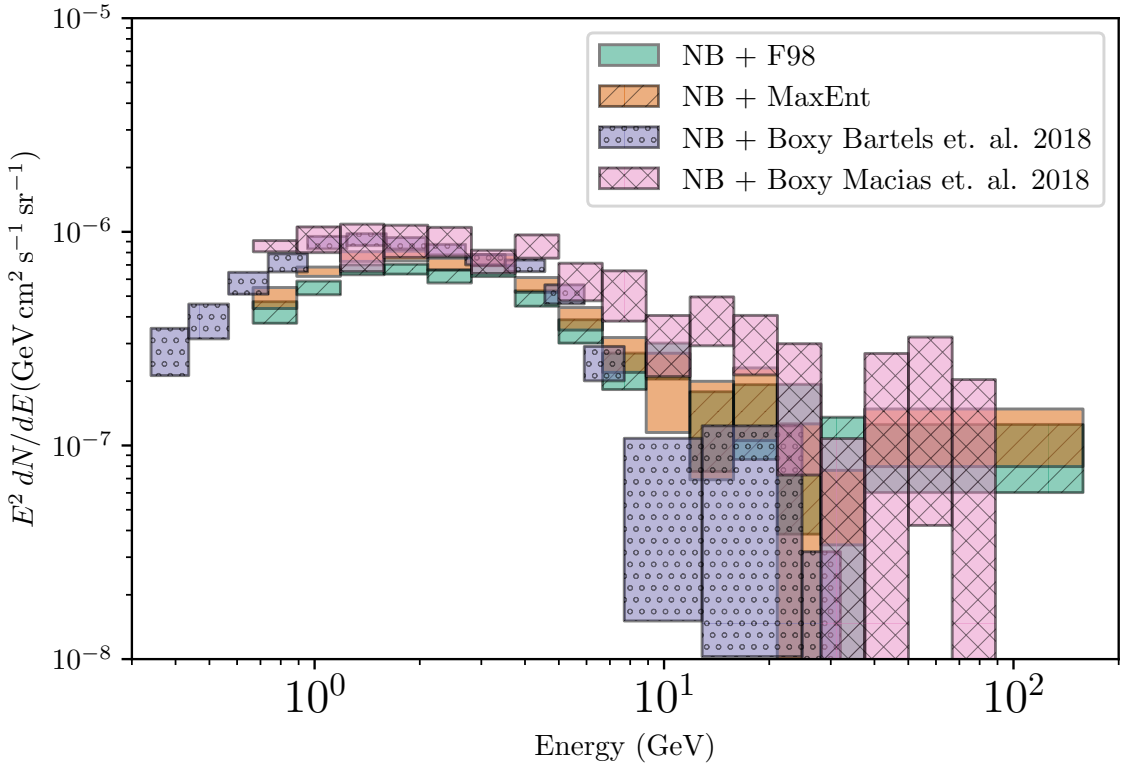

Fig. 3.33 Gamma ray fluxes for the Nuclear Bulge (NB) + Freudenreich, 1998 boxy bulge model (green) and the NB + non-parametric maximum entropy bulge (orange). Included for comparison are the NB + boxy-bulge model of Bartels et al., 2018 (purple) and the NB + boxy bulge model of Macias et al., 2018 (pink).

We deconvolved the density of the bulge in the minimal assumption model, Eq. 3.30, by minimising the $-2\ln\mathcal{L}$ in Eq. 3.10, using the same prior parametric density as model H. We used the regularisation parameters in Table 3.6.

Fig. 3.34 shows examples of our model fit for two different lines of sight. At high latitudes, as in the top panel of Fig. 3.34, the VVV data is very noisy due to low number counts. The maximum entropy method is able to predict the splitting of the RC, even though it is not immediately apparent in the data. Due to the smoothing regularisation, the fitted model for the displayed line of sight is influenced by data in all of the neighbouring voxels. As a result, the model can appear poorly constrained by the data in a single line of sight, as in the bottom panel of Fig. 3.34. When viewed as a slice of the data, as in Fig.3.35, the model is well constrained across multiple neighbouring line of sights. Due to the narrowness of the RC in the luminosity function, the morphology of the bulge is mainly constrained by the stars in the magnitude range $12 < K_s < 14$. Therefore, the slight bias of the fit outside this range is not of particular concern as it is not directly influencing our inferences about the morphology of the bulge region.

We plot a Cartesian projection of the reconstructed bulge density in Fig. 3.36, where the origin is centred on the maximum density of the bulge. From this we infer that the Sun is at $(x, y, z) = (-8.0, 0.0, 0.0)$ kpc. The X-arms are visible at $|z| > 0.319$ kpc. Although WG13 had a similar result for $z < 0$, they had significant gaps in their reconstruction for $z > 0.263$ kpc. However, they filled in these gaps by assuming eight fold symmetry. As we did not have this problem, we did not need to make any symmetry assumptions. A result of this is that our final reconstruction of the X-arm nearest to the Sun is less dense than our reconstruction of the X-arm that is farthest from the Sun. In contrast, WG13's final reconstruction had identical X-arms due to their symmetry assumptions. Our less restrictive symmetry assumptions have also allowed us to uncover the presence of a spiral arm structure in front of the bar, which is visible in the deconvolved density (left panels of Fig. 3.36) for all $|z| < 500$ pc at $x \sim -3$ kpc. We also found a spiral arm structure behind the bar which is visible at all $|z| < 1$ kpc at $x \sim 3$ kpc.

At $z = \pm 0.319$ kpc where, the X-arms have started to merge, the residuals in the right column of Fig. 3.36 show that the maxima of the X-arm at positive x has migrated to $(x, y) = (0, 0)$ kpc. The maxima of the X-arm at negative x has migrated to $(x, y) = (-0.8, 0.0)$ kpc, so that the midpoint of the two X-arms is at $(x, y) = (-0.4, 0.0)$ kpc. At $z = -1.001$ kpc, the midpoint of the X-arms is

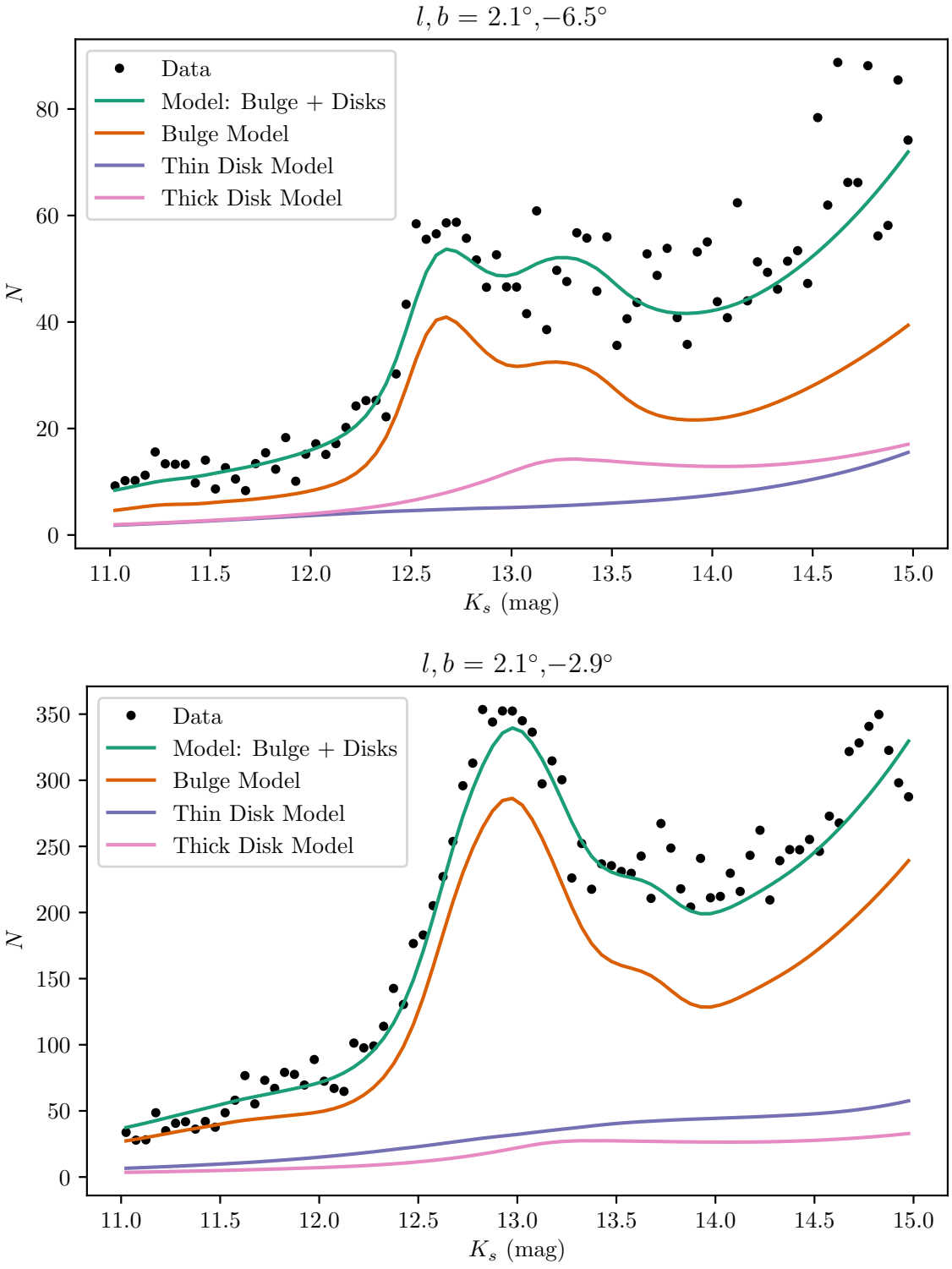

Fig. 3.34 Demonstration of the fitted model for a line of sight that displays a splitting in the RC (Top panel) and a line of sight that is near the edge of the masked midplane region (Bottom panel).

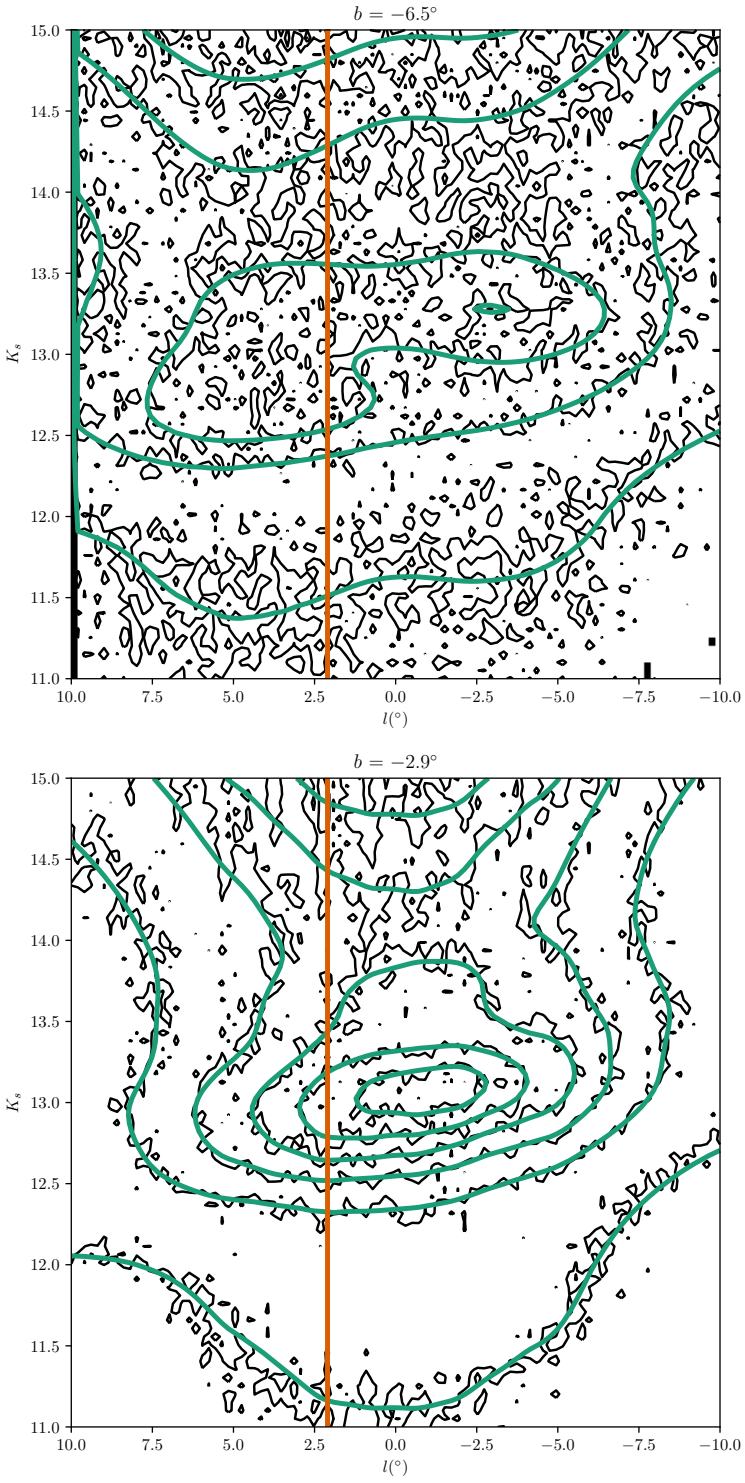

Fig. 3.35 Fitted model (green contours) as compared to the VVV data (black contours) for two representative latitude slices, one that shows the split RC at $b = -6.7°$ (top panel), and one that is near the Galactic midplane mask at $b = -2.9°$ (bottom panel). The line of sights in Fig. 3.34 are shown in orange.

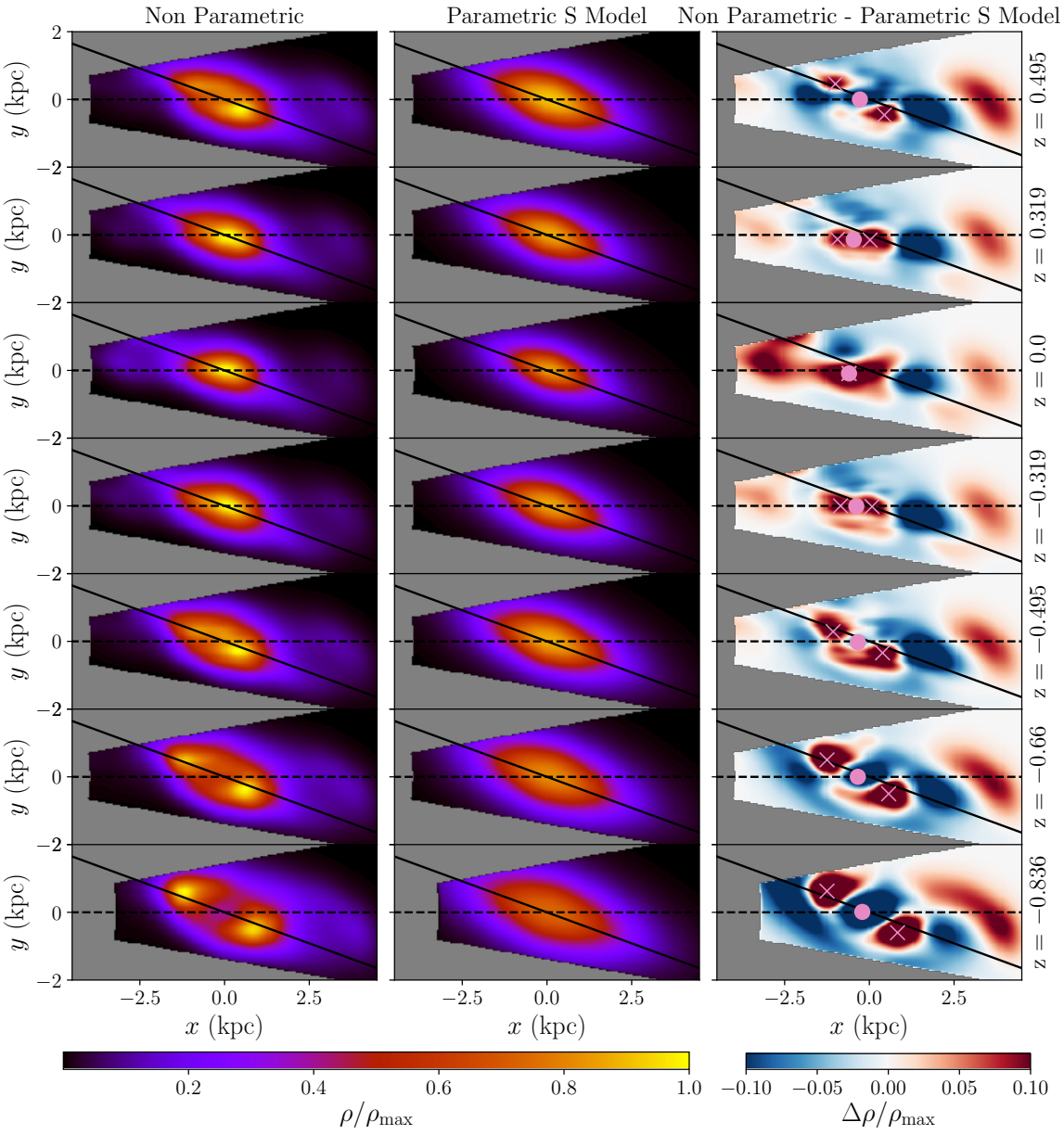

Fig. 3.36 Cartesian projections of the bulge density from the maximum entropy deconvolution (left column) and the parametric prior density model (middle column). The Sun is located at $(x, y, z) = (-8.0, 0.0, 0.0)$. The dashed black line indicates $l = 0°$ and the solid black line is the major axis of the bar in the parametric model, which is at an angle of 19.8° from the $l = 0°$ line. The z coordinate is measured in kpc. At $x \sim \pm 3$ kpc the spiral arm structures at both ends of the bulge are visible, most clearly in the residuals (right column), which has had the colour bar clipped at ±10%. The pink crosses indicate the maximum density of the X-arms, and the pink circle is the midpoint between the two arms.

$(x, y) = (0.0, 0.0)$. This is consistent with the observed R_0 shift of 400 pc in WG13, which they interpreted as an intrinsic brightening of the RC due to a metallicity gradient. Additionally, a 400 pc shift forward is also consistent with the 5 Gyr old (0.1 mag brighter RC) E-model component of the S+E model in S17. The bottom of the X-arms merge into a structure that is consistent with the orientation of the E component of S17 S+E model.

Shown in the top left panel of Fig. 3.37 are the positions of the maximum density in the X-arms, where the X-arms maxima appear to move closer to the Sun as z approaches zero. We assume that the shifting towards the Sun is an intrinsic brightening of the RC, so that at each z the X-arm maxima positions should be shifted so that the mid-point between them is $(x, y) = (0.0, 0.0)$. After correcting for the apparent intrinsic brightening, the X-arms exhibit a clear twisting structure. The twist is especially obvious in the bottom-right panel of Fig. 3.37, which shows there is no axis in the $x - y$ plane in which the X-arms would exhibit axial symmetry. The X-arms have a 180° rotational symmetry. Interestingly, the maxima of the X-arms appear to be nearly aligned with the major axis of the long bar of Wegg et al., 2015 (purple shading in bottom-right panel of Fig. 3.37). Overall, the results in Fig. 3.37 demonstrate that the X-bulge cannot be described by an eight fold symmetric structure.

The positions of the spiral arm structures in Fig. 3.38 are consistent with the inner galaxy of the simulated gas distribution of Renaud et al., 2013[3]. The location of the spiral arm from Gonzalez et al., 2018 (white triangles in Fig. 3.38) are closer to the Sun than predicted by our model. This is likely because we have only considered fields that are not heavily effected by extinction and crowding. Additionally, the K_s magnitudes of the VVV stars in Gonzalez et al., 2018 have the photometric zero-point calibrated to the CASU aperture photometry catalogues, which is not consistent with the corrected zero-point magnitudes we have used.

In order to evaluate the apparent magnitude of the spiral arm structure in front of the bar, we note that as illustrated in Fig. 3.3, $M_{K_s} \approx -1.53$ mag. Also, as can be seen from Fig. 3.38, the distance of this feature from the Sun is 5 kpc. We can then use the standard relation

$$K_s - M_{K_s} = 5 \log_{10} s + 10, \tag{3.31}$$

[3] http://www.astro.lu.se/~florent/mw_large.php

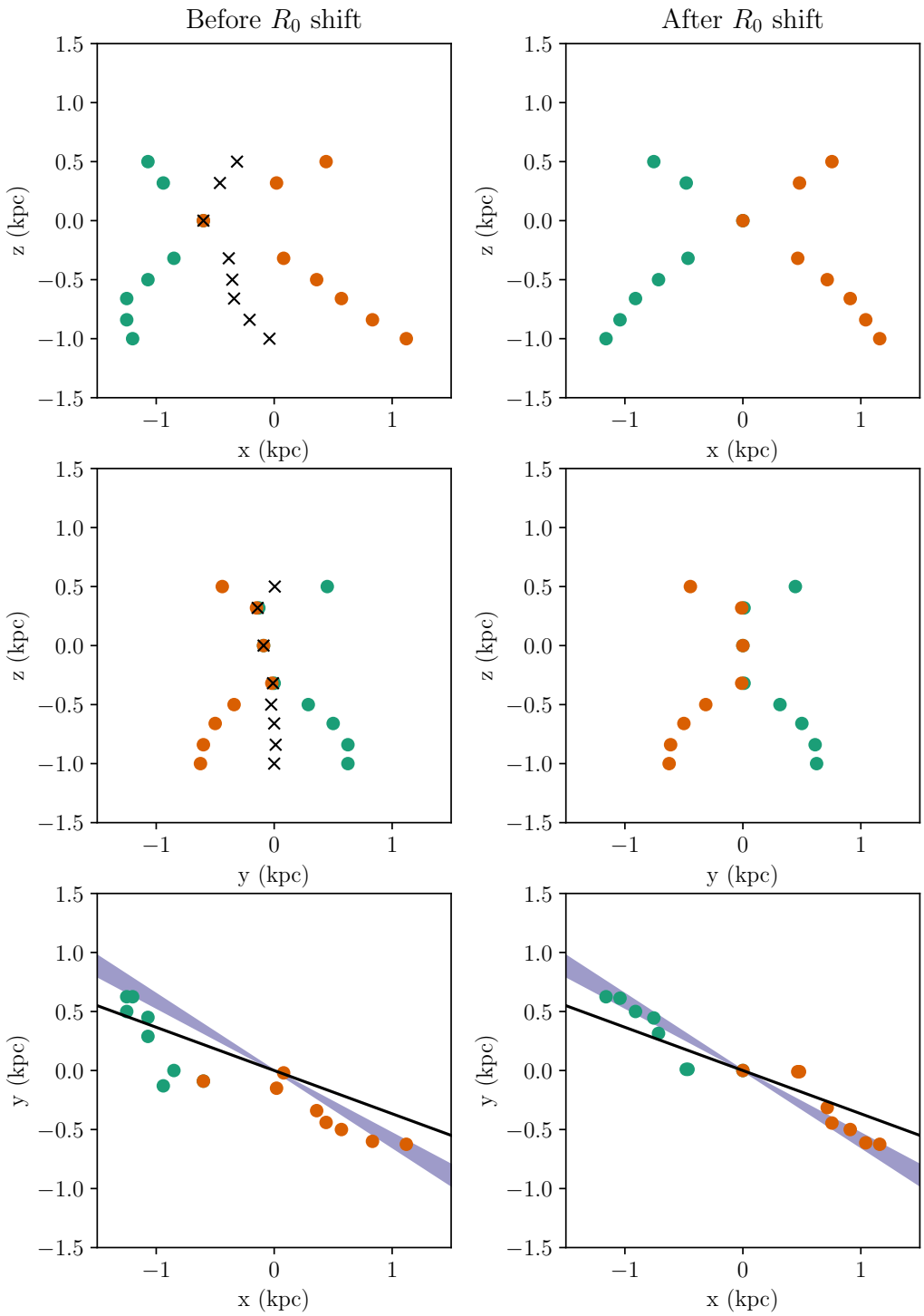

Fig. 3.37 Positions of the maximum density in the X-arms in Cartesian co-ordinates, with the Sun at $(x, y, z) = (-8.0, 0.0, 0.0)$. The panels on the right have been shifted assuming the X-arms midpoints (black crosses) between the arms should be at $(x, y) = (0, 0)$ kpc. The black line in the bottom panel shows the bar major axis. The purple shaded region shows the range of long bar angles (28-33°) found by Wegg et al., 2015.

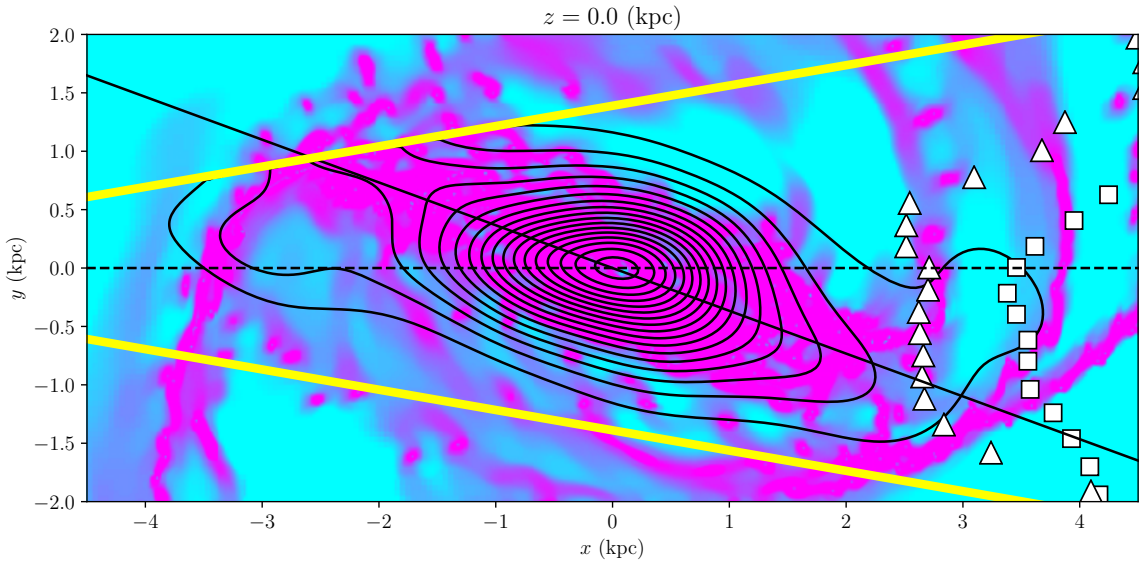

Fig. 3.38 VVV deconvolved stellar density (black contours) as compared to the simulated inner galaxy gas distribution of Renaud et al., 2013. The Sun is located at $(x, y, z) = (-7.9, 0.0, 0.0)$. The location of the spiral arm structure behind the bar falls between the simulation (white squares) and VVV data analysis predictions (white triangles) of Gonzalez et al., 2018. The yellow lines show $l = \pm 10°$. The spiral arm structures at the end of the bars are offset from the bar major axis (black solid line).)

where s is in kpc. Substituting in the above values and solving gives $K_s \approx 11.96$ mag. As Gonzalez et al., 2018 only used data with $K_s \gtrsim 12$ mag, they would not have been sensitive to this feature.

As noted by Gonzalez et al., 2018, the RGBB of the bulge has a similar K_s to the feature behind the bar. A mismodelling of the RGBB might explain some of the signal at z far from the Galactic midplane seen in the right hand side panels of Fig. 3.36, where we may not expect a spiral arm like density. At low $|z|$, the density morphology is more obviously spiral arm like and is mirrored by a similar morphology in front of the bar, as seen in Fig. 3.38, where there is no RGBB contamination. Therefore, even though the high $|z|$ region is showing contamination from the RGBB, the symmetric morphology at low $|z|$ and the consistency with N-body simulations suggests that at least some of the signal is from a spiral arm structure.

3.10 Conclusions

We have used a non-parametric method incorporating maximum entropy and smoothness regularisation to deconvolve the density distribution of bulge stars in the VVV MW-BULGE-PSFPHOT catalogue. We have also proposed a maximum entropy method for determining the background non-RC stars, based on prior estimates of the background using parametric models. Reasonable values for the regularisation parameters were found by testing the deconvolution method on a realistic simulated stellar population of the galaxy made of a 10 Gyr old eight fold symmetric bulge, thin disk and thick disk. Testing our maximum entropy deconvolution and background fitting method on a simulated population, we were able to nearly perfectly reconstruct the density even in the heavily extincted and crowded regions that had been masked in the analysis.

Applying the deconvolution method to the VVV data we found many of the features previously observed in the literature, including the X-shaped bulge from the split RC, the apparent vertical R_0 gradient (possibly due to the vertical metallicity gradient), the dependence on viewing angle and intrinsic RC luminosity dispersion and the spiral arm structure ~ 3 kpc behind the bar. The R_0 gradient was not clearly seen in the MW-BULGE-PSFPHOT star counts when using the Richardson-Lucy deconvolution method assuming eight fold symmetry, though it was observed when using a minimal assumption maximum entropy deconvolution.

We have observed two new morphological features in the inner region of the Milky Way: a feature ~ 3 kpc in front of the Galactic centre consistent with a foreground spiral arm, and a twisting in the shape of the X-arms of the X-bulge. Both features were more easily detected when using our minimal assumption model, which made no symmetry assumptions and utilised the full luminosity function of the bulge and the Besançon disk models to account for background stars. In fact, the spiral arm structure in front of the bar was not detectable in our maximum entropy method which assumed two-fold symmetry and the maximum entropy background. The existence of the twisting explains the difficulty in fitting the eight fold symmetric bulge models to the stellar density, as the twisted X-arms exhibit no axes of symmetry.

Assuming a Chabrier IMF, we estimate the total stellar mass of the bulge to be 1.33-1.71 $M_\odot$, where 30.1% of the mass is stellar remnants. From parametric modelling, we infer a bar angle in the range 18-32° and an X-bulge mass fraction of 18-25%. These results are broadly compatible with other recent analyses of the VVV data.

We performed extensive systematic tests of the maximum entropy deconvolution method to test our assumptions regarding the choice of background model, metallicity distribution, intrinsic dispersion of the RC, and the position of the Sun above the Galactic midplane.

The maximum entropy background was significantly preferred over the widely used exponential background by both the parametric models we fitted and the maximum entropy deconvolution method. Future studies of bulge star counts should be wary using the exponential background, as we have shown it has a tendency to over estimate the background star counts at the bright end of the luminosity function, causing the density of stars to be significantly underestimated at nearby distances.

A broad, unimodal metallicity distribution with spatially varying mean metallicity did not significantly effect the bulge stellar density. A bi-modal metallicity distribution is likely needed, which will become possible as the coverage of bulge spectroscopic surveys grows.

Using an intrinsically broader RC luminosity function was not favoured by the maximum entropy deconvolution method or a parametric model. In particular, the broad luminosity function was not compatible with a SX parametric model, as the optimal solution was one with an unnaturally pronounced X-shaped feature.

Our non parametric density model provided a significantly better fit to the *Fermi* GeV CCE than the previously implemented parametric S model of F98. This further supports the population of millisecond pulsar population interpretation of the GeV GCE, traced by the Galactic bulge stellar population.

Chapter 4

Summary and Future Work

An anomalous excess of GeV gamma rays originating from the Galactic centre has offered the possibility to indirectly observe the annihilation of dark matter particles. Early analyses suggested that the excess was morphologically spherically symmetric, with a gamma-ray spectrum that peaked at ~ 2 GeV, consistent with the annihilation of 20-50 GeV/c^2 mass weakly interacting massive particles distributed with a Navarro-Frenk-White density profile. This was an exciting prospect, as the density distribution was generally consistent with cosmological simulations, and the particle properties were about what was expected for the neutralino from super-symmetry. The excess signal properties were, however, not unique to annihilating dark matter. The gamma-ray spectrum was similar in shape to the those of resolved millisecond pulsars, so a proposed astrophysical alternative was an unresolved of bulge millisecond pulsars. A spherical morphology would be expected for a population of millisecond pulsars that had been assimilated into the bulge via mergers with globular clusters in the early history of the Milky Way.

Both the morphological and spectral properties of the galactic centre excess (GCE) are reliant on accurate modelling of all usual astrophysical processes. The most significant contribution, by a factor of $\sim$10, at the peak energy of the GCE spectrum comes from the interaction between cosmic rays and the interstellar medium. In Chapter 2, we compare two different methods of generating hydrogen gas maps. The standard interpolation method used by the Fermi Collaboration to produce the interstellar emission model assumes that the gas orbits the Milky Way in circular orbits, where the Galactic centre region is interpolated to correct for the loss of kinematic resolution. Alternatively, we use the model of Pohl et al., 2008, which infers the orbital motion of the gas in the inner galaxy using hydrodynamical simulations. From the Doppler shift

of the 21cm emission of atomic hydrogen and 2.6mm emission of carbon monoxide we constructed a map of the 3-D distribution of gas in annular regions of the Milky Way, using both the interpolated and hydrodynamic methods. The hydrodynamic gas map provided a statistically better fit to the *Fermi* gamma ray emission than the interpolated gas map. Even when we accounted for all resolved point sources and used the improved diffuse gamma ray emission template from the hydrodynamical modelling, the GCE persisted.

Prior to our analysis of the GCE that is presented in Chapter 2 and originally in Macias et al., 2018, the spatial morphology of the millisecond pulsar explanation of the GCE assumed that the population of unresolved point sources were distributed identically to the dark matter distribution in an *a posteriori* way to match the observed GCE signal. We instead posited *a priori* that the millisecond pulsar population should follow the distribution of the bulge stellar population. We included into our model an extended source with spatial morphology matching the integrated density of stars in the nuclear bulge and either the X-shaped bulge or boxy-bulge. Including the integrated stellar density templates significantly improved the fit to the gamma ray emission. Once they had been included, the significance of an additional spherically symmetric Nevarro-Frenk-White signal consistent with dark matter annihilation was $< 3\ \sigma$. These results have been corroborated by Bartels et al., 2018, with a preference for the boxy-bulge over an X-shaped bulge when a larger fraction of the sky is analysed.

In Chapter 3, we worked to update the boxy-bulge template from Chapter 2 from the S-model bulge of Freudenreich, 1998, which was obtained by fitting a parametric triaxial density model to the diffuse near infra-red observations of *COBE/DIRBE*. For this purpose, we take advantage of the standard candle property of the He core burning red clump giant stars of the galactic bulge to trace out the 3-D distribution of stars. Near infrared observations from the VISTA Variables in Via Lactea (VVV) survey offer K_s apparent magnitudes for red clump giant stars over $\sim 75\%$ of the area of the bulge. Both parametric and non-parametric descriptions of the VVV red clump giant density have been explored in the literature, notably Simion et al., 2017 and Wegg et al., 2013. Neither of the existing approaches could offer a sufficiently detailed technique to provide a stellar density template for an analysis of the *Fermi* GCE; the parametric models did not capture the X-shaped component of the bulge, whereas the non-parametric model was limited to the VVV region ($|l| < 10°$ and $-10° < b < 5°$) that was not heavily extincted by dust. We developed a hybrid non-parametric model that would smoothly transition to a prior parametric model outside the VVV region

and naturally inpaint the heavily crowded and extincted galactic plane. Part of this non-parametric method involved fitting a background of non red clump giant stars.

Our maximum entropy deconvolution method required three things; a luminosity function describing the expected absolute magnitude distribution of red giant stars, a choice of hyper parameters for the maximum entropy and smoothness regularisation, and a parametric density model as a prior estimate of the red clump giant density. We generated the luminosity function using a semi-analytic technique assuming a 10 Gyr old population of stars with normally distributed metallicity, $[\mathrm{Fe/H}] \sim \mathcal{N}(0.0, 0.4)$, and using the PARSEC+COLIBRI isochrones. To choose the ideal regularisation hyper parameters, we tested a range of choices on a realistic synthetic catalogue of stars for a triaxial bulge and selected the parameters which gave a reconstruction close to the true density. A prior parametric density was obtained by fitting a SX parametric model to the VVV catalogue.

To test to robustness and limitations of our new non-parametric method we performed a range of systematic tests regarding particular choices made for our model; we tested the effect of not adding the feature behind the bar to the background, masking the VVV data based on extinction only rather than extinction + crowding, using the widely used exponential background for the red giant branch, using a broad intrinsic luminosity function for the red clump, adding a vertical metallicity gradient, and the position of the Sun. For each test case we performed the full maximum entropy deconvolution, including fitting the parametric prior model, to both the synthetic star catalogue and the VVV catalogue. To assess the significance of each test we compared the test statistic (TS) to the corresponding TS in the synthetic catalogue. For example, the simulated population does not have a metallicity gradient and the TS for this test case is nearly zero. The metallicity gradient case in the VVV data also has a near zero TS, so we conclude that the VVV data does not significantly favour the broad, uni-modal metallicity gradient over no metallicity gradient. In a similar vein, the non-parametric method was insensitive to a broader intrinsic red clump luminosity function and the position of the Sun above the plane. The exponential background was disfavoured significantly by both the non-parametric and parametric model.

From the parametric model fitting the bulge is at an angle of 18-32° where the larger angles are due to the broad red clump luminosity function test case, consistent with the result of Simion et al., 2017. The contributions from the X-shaped component is 18-25% of the mass of the bulge. From the non-parametric density models we estimate the total stellar mass of the bulge assuming a Chabrier initial mass function

as 1.33-1.71$\times 10^6$ $M_\odot$, where 30.1 % of the mass is in stellar remnants. The distance to the Galactic centre we infer is 7.9 kpc, though if our red clump luminosity function had the same mean absolute magnitude (-1.53 mag) as local red clump giants (-1.61 mag), then the distance would increase by a factor of 1.04 to 8.24 kpc.

As a final test of the power and flexibility of our maximum entropy deconvolution we relaxed all symmetry assumptions and modified the model to make use of the full luminosity function rather than just the red clump. The reconstructed density in the minimal assumption model uncovered spiral arm structures $\sim$3 kpc in front of and behind the bulge, offset above and below the bar major axis. Additionally, once corrected for the apparent vertical brightening, the X-arms in the minimal assumption model were twisted so that they did not exhibit any axial symmetry, only a 180° rotational symmetry in the plane of the galaxy. It is clear from this analysis that the luminosity function needs to be improved to account for the bi-modal metallicity distribution observed in spectroscopic studies of the bulge, which could account for the apparent vertical brightening of the red clump giants. Another interesting follow up to this work would be investigating whether twisted X-arms are present in N-body simulations of bulges, and if there is any association between the spiral arm structures.

We found that the maximum entropy deconvolution integrated density provided the best fit to the *Fermi* data, the parametric SX model provided the second best fit, and the parametric S-model of Freudenreich, 1998 provided the worst fit of the bulge density templates. This shows that as the model for the galactic bulge more accurately describes the stellar density, the better it also fits to the *Fermi* data. Even though our analysis can't explicitly show that bulge millisecond pulsars contribute to the gamma ray emission in the inner galaxy, it is clear that there is an extended emission associated with the stellar bulge.

References

Abazajian, K. N. (2011). "The consistency of Fermi-LAT observations of the galactic center with a millisecond pulsar population in the central stellar cluster". In: *JCAP* 2011.3, 010, p. 010. DOI: 10.1088/1475-7516/2011/03/010. arXiv: 1011.4275 [astro-ph.HE].

Abazajian, K. N. et al. (2012). "Detection of a gamma-ray source in the Galactic Center consistent with extended emission from dark matter annihilation and concentrated astrophysical emission". In: *Phys. Rev. D* 86.8, 083511, p. 083511. DOI: 10.1103/PhysRevD.86.083511. arXiv: 1207.6047 [astro-ph.HE].

Abazajian, K. N. et al. (2014). "Astrophysical and dark matter interpretations of extended gamma-ray emission from the Galactic Center". In: *Phys. Rev. D* 90.2, 023526, p. 023526. DOI: 10.1103/PhysRevD.90.023526. arXiv: 1402.4090 [astro-ph.HE].

Abdo, A. A. et al. (2013). "The Second Fermi Large Area Telescope Catalog of Gamma-Ray Pulsars". In: *ApJS* 208.2, 17, p. 17. DOI: 10.1088/0067-0049/208/2/17. arXiv: 1305.4385 [astro-ph.HE].

Acero, F. et al. (2015). "Fermi Large Area Telescope Third Source Catalog". In: *ApJS* 218, 23, p. 23. DOI: 10.1088/0067-0049/218/2/23. arXiv: 1501.02003 [astro-ph.HE].

Acero, F. et al. (2016). "Development of the Model of Galactic Interstellar Emission for Standard Point-source Analysis of Fermi Large Area Telescope Data". In: *ApJS* 223.2, 26, p. 26. DOI: 10.3847/0067-0049/223/2/26. arXiv: 1602.07246 [astro-ph.HE].

Ackermann, M. et al. (2012). "Fermi-LAT Observations of the Diffuse γ-Ray Emission: Implications for Cosmic Rays and the Interstellar Medium". In: *ApJ* 750.1, 3, p. 3. DOI: 10.1088/0004-637X/750/1/3. arXiv: 1202.4039 [astro-ph.HE].

Ackermann, M. et al. (2013). "Detection of the Characteristic Pion-Decay Signature in Supernova Remnants". In: *Science* 339.6121, pp. 807–811. DOI: 10.1126/science.1231160. arXiv: 1302.3307 [astro-ph.HE].

Ackermann, M. et al. (2014). "The Spectrum and Morphology of the Fermi Bubbles". In: *ApJ* 793, 64, p. 64. DOI: 10.1088/0004-637X/793/1/64. arXiv: 1407.7905 [astro-ph.HE].

Ackermann, M. et al. (2015). "Searching for Dark Matter Annihilation from Milky Way Dwarf Spheroidal Galaxies with Six Years of Fermi Large Area Telescope Data". In: *Phys. Rev. Lett.,* 115.23, 231301, p. 231301. DOI: 10.1103/PhysRevLett.115.231301. arXiv: 1503.02641 [astro-ph.HE].

Ackermann, M. et al. (2017). "The Fermi Galactic Center GeV Excess and Implications for Dark Matter". In: *ApJ* 840, 43, p. 43. DOI: 10.3847/1538-4357/aa6cab. arXiv: 1704.03910 [astro-ph.HE].

Ajello, M. et al. (2016). "Fermi-LAT Observations of High-Energy Gamma-Ray Emission toward the Galactic Center". In: *ApJ* 819.1, 44, p. 44. DOI: 10.3847/0004-637X/819/1/44. arXiv: 1511.02938 [astro-ph.HE].

Akerib, D. S. et al. (2017). "Results from a Search for Dark Matter in the Complete LUX Exposure". In: *Phys. Rev. Lett.,* 118.2, 021303, p. 021303. DOI: 10.1103/PhysRevLett.118.021303. arXiv: 1608.07648 [astro-ph.CO].

Aprile, E. et al. (2018). "Dark Matter Search Results from a One Ton-Year Exposure of XENON1T". In: *Phys. Rev. Lett.,* 121.11, 111302, p. 111302. DOI: 10.1103/PhysRevLett.121.111302. arXiv: 1805.12562 [astro-ph.CO].

Arcadi, G. et al. (2018). "The waning of the WIMP? A review of models, searches, and constraints". In: *European Physical Journal C* 78.3, 203, p. 203. DOI: 10.1140/epjc/s10052-018-5662-y. arXiv: 1703.07364 [hep-ph].

Atlas Collaboration (2016). "Search for new phenomena in final states with an energetic jet and large missing transverse momentum in p p collisions at $\sqrt{\{s\}}$=13 TeV using the ATLAS detector". In: *Phys. Rev. D* 94.3, 032005, p. 032005. DOI: 10.1103/PhysRevD.94.032005. arXiv: 1604.07773 [hep-ex].

Atwood, W. B. et al. (2009). "The Large Area Telescope on the Fermi Gamma-Ray Space Telescope Mission". In: *ApJ* 697.2, pp. 1071–1102. DOI: 10.1088/0004-637X/697/2/1071. arXiv: 0902.1089 [astro-ph.IM].

Babusiaux, C. (2016). "Correlations between Kinematics and Metallicity in the Galactic Bulge: A Review". In: *Publ. Astron. Soc. Australia* 33, e026, e026. DOI: 10.1017/pasa.2016.1. arXiv: 1601.07761.

Babusiaux, C. et al. (2010). "Insights on the Milky Way bulge formation from the correlations between kinematics and metallicity". In: *A&A* 519, A77, A77. DOI: 10.1051/0004-6361/201014353. arXiv: 1005.3919 [astro-ph.GA].

Bartels, R. et al. (2016). "Strong Support for the Millisecond Pulsar Origin of the Galactic Center GeV Excess". In: *Phys. Rev. Lett.,* 116.5, 051102, p. 051102. DOI: 10.1103/PhysRevLett.116.051102. arXiv: 1506.05104 [astro-ph.HE].

Bartels, R. et al. (2018). "The Fermi-LAT GeV excess as a tracer of stellar mass in the Galactic bulge". In: *Nature Astronomy* 2, pp. 819–828. DOI: 10.1038/s41550-018-0531-z. arXiv: 1711.04778 [astro-ph.HE].

Bennett, C. L. et al. (2003). "First-Year Wilkinson Microwave Anisotropy Probe (WMAP) Observations: Foreground Emission". In: *ApJS* 148.1, pp. 97–117. DOI: 10.1086/377252. arXiv: astro-ph/0302208 [astro-ph].

Bernabei, R. et al. (2013). "Final model independent result of DAMA/LIBRA-phase1". In: *European Physical Journal C* 73, 2648, p. 2648. DOI: 10.1140/epjc/s10052-013-2648-7. arXiv: 1308.5109 [astro-ph.GA].

Bertone, G. et al. (2005). "Particle dark matter: evidence, candidates and constraints". In: *Phys. Rep.* 405.5-6, pp. 279–390. DOI: 10.1016/j.physrep.2004.08.031. arXiv: hep-ph/0404175 [hep-ph].

Bhattacharya, D. et al. (1991). "Formation and evolution of binary and millisecond radio pulsars". In: *Phys. Rep.* 203, pp. 1–124. DOI: 10.1016/0370-1573(91)90064-S.

Binney, J. et al. (1991). "Understanding the kinematics of Galactic centre gas". In: *MNRAS* 252, pp. 210–218. DOI: 10.1093/mnras/252.2.210.

Bissantz, N. et al. (1997). "The microlensing optical depth of the COBE bulge". In: *MNRAS* 289, pp. 651–659. DOI: 10.1093/mnras/289.3.651. eprint: astro-ph/9612026.

Bissantz, N. et al. (2002). "Spiral arms, bar shape and bulge microlensing in the Milky Way". In: *MNRAS* 330, pp. 591–608. DOI: 10.1046/j.1365-8711.2002.05116.x. eprint: astro-ph/0110368.

Bland-Hawthorn, J. et al. (2003). "The Large-Scale Bipolar Wind in the Galactic Center". In: *ApJ* 582.1, pp. 246–256. DOI: 10.1086/344573. arXiv: astro-ph/0208553 [astro-ph].

Bland-Hawthorn, J. et al. (2016). "The Galaxy in Context: Structural, Kinematic, and Integrated Properties". In: *ARA&A* 54, pp. 529–596. DOI: 10.1146/annurev-astro-081915-023441. arXiv: 1602.07702 [astro-ph.GA].

Bland-Hawthorn, J. et al. (2019). "The large-scale ionization cones in the Galaxy". In: *arXiv e-prints*, arXiv:1910.02225, arXiv:1910.02225. arXiv: 1910.02225 [astro-ph.GA].

Bland-Hawthorn, J. et al. (2013). "Fossil Imprint of a Powerful Flare at the Galactic Center along the Magellanic Stream". In: *ApJ* 778.1, 58, p. 58. DOI: 10.1088/0004-637X/778/1/58. arXiv: 1309.5455 [astro-ph.GA].

Boyarsky, A. et al. (2011). "A comment on the emission from the Galactic Center as seen by the Fermi telescope". In: *Phys. Lett.* B705, pp. 165–169. DOI: 10.1016/j.physletb.2011.10.014. arXiv: 1012.5839 [hep-ph].

Brandt, T. D. et al. (2015). "Disrupted Globular Clusters Can Explain the Galactic Center Gamma-Ray Excess". In: *ApJ* 812.1, 15, p. 15. DOI: 10.1088/0004-637X/812/1/15. arXiv: 1507.05616 [astro-ph.HE].

Camilo, F. et al. (2005). "Pulsars in Globular Clusters". In: *Binary Radio Pulsars*. Ed. by F. A. Rasio et al. Vol. 328. Astronomical Society of the Pacific Conference Series, p. 147. arXiv: astro-ph/0501226 [astro-ph].

Cao, L. et al. (2013). "A new photometric model of the Galactic bar using red clump giants". In: *MNRAS* 434, pp. 595–605. DOI: 10.1093/mnras/stt1045. arXiv: 1303.6430 [astro-ph.GA].

Casandjian, J.-M. (2015). "The Fermi-LAT model of interstellar emission for standard point source analysis". In: *arXiv e-prints*, arXiv:1502.07210, arXiv:1502.07210. arXiv: 1502.07210 [astro-ph.HE].

Casandjian, J.-M. et al. (2009). "High Energy Gamma-Ray Emission from the Loop I region". In: *arXiv e-prints*, arXiv:0912.3478, arXiv:0912.3478. arXiv: 0912.3478 [astro-ph.HE].

Catchpole, R. M. et al. (2016). "The age and structure of the Galactic bulge from Mira variables". In: *MNRAS* 455.2, pp. 2216–2227. DOI: 10.1093/mnras/stv2372. arXiv: 1510.03295 [astro-ph.SR].

Chabrier, G. (2003). "Galactic Stellar and Substellar Initial Mass Function". In: *PASP* 115.809, pp. 763–795. DOI: 10.1086/376392. arXiv: astro-ph/0304382 [astro-ph].

Chan, V. C. et al. (2019). "The {Gaia} DR2 parallax zero point: Hierarchical modeling of red clump stars". In: *arXiv e-prints*, arXiv:1910.00398, arXiv:1910.00398. arXiv: 1910.00398 [astro-ph.SR].

Chemin, L. et al. (2009). "H I Kinematics and Dynamics of Messier 31". In: *ApJ* 705.2, pp. 1395–1415. DOI: 10.1088/0004-637X/705/2/1395. arXiv: 0909.3846 [astro-ph.CO].

Chemin, L. et al. (2015). "Incorrect rotation curve of the Milky Way". In: *A&A* 578, A14, A14. DOI: 10.1051/0004-6361/201526040. arXiv: 1504.01507 [astro-ph.GA].

Chernyakova, M. et al. (2011). "The High-energy, Arcminute-scale Galactic Center Gamma-ray Source". In: *ApJ* 726, 60, p. 60. DOI: 10.1088/0004-637X/726/2/60. arXiv: 1009.2630 [astro-ph.HE].

Cholis, I. et al. (2015). "The Galactic Center GeV excess from a series of leptonic cosmic-ray outbursts". In: *JCAP* 2015.12, 005, p. 005. DOI: 10.1088/1475-7516/2015/12/005. arXiv: 1506.05119 [astro-ph.HE].

Clarke, J. P. et al. (2019). "The Milky Way bar/bulge in proper motions: a 3D view from VIRAC & Gaia". In: *arXiv e-prints*, arXiv:1903.02003, arXiv:1903.02003. arXiv: 1903.02003 [astro-ph.GA].

Clarkson, W. I. et al. (2011). "The First Detection of Blue Straggler Stars in the Milky Way Bulge". In: *ApJ* 735.1, 37, p. 37. DOI: 10.1088/0004-637X/735/1/37. arXiv: 1105.4176 [astro-ph.GA].

Clemens, D. P. (1985). "Massachusetts-Stony Brook Galactic plane CO survey: the galactic disk rotation curve." In: *ApJ* 295, pp. 422–436. DOI: 10.1086/163386.

CMS Collaboration (2017). "Search for dark matter produced with an energetic jet or a hadronically decaying W or Z boson at sqrt(s) = 13 TeV". In: *arXiv e-prints*, arXiv:1703.01651, arXiv:1703.01651. arXiv: 1703.01651 [hep-ex].

Cook, G. B. et al. (1994). "Recycling Pulsars to Millisecond Periods in General Relativity". In: *ApJ* 423, p. L117. DOI: 10.1086/187250.

Cornwell, T. J. et al. (1985). "A simple maximum entropy deconvolution algorithm". In: *A&A* 143, pp. 77–83.

Dame, T. M. et al. (2001). "The Milky Way in Molecular Clouds: A New Complete CO Survey". In: *ApJ* 547.2, pp. 792–813. DOI: 10.1086/318388. arXiv: astro-ph/0009217 [astro-ph].

Damiani, F. et al. (1997). "A Method Based on Wavelet Transforms for Source Detection in Photon-counting Detector Images. I. Theory and General Properties". In: *The Astrophysical Journal* 483.1, pp. 350–369. DOI: 10.1086/304217. URL: https://doi.org/10.1086%2F304217.

Daylan, T. et al. (2016). "The characterization of the gamma-ray signal from the central Milky Way: A case for annihilating dark matter". In: *Physics of the Dark Universe* 12, pp. 1–23. DOI: 10.1016/j.dark.2015.12.005. arXiv: 1402.6703 [astro-ph.HE].

de Blok, W. J. G. et al. (2008). "High-Resolution Rotation Curves and Galaxy Mass Models from THINGS". In: *Astronom. J.* 136, pp. 2648–2719. DOI: 10.1088/0004-6256/136/6/2648. arXiv: 0810.2100.

Dékány, I. et al. (2013). "VVV Survey Near-infrared Photometry of Known Bulge RR Lyrae Stars: The Distance to the Galactic Center and Absence of a Barred Distribution of the Metal-poor Population". In: *ApJ* 776.2, L19, p. L19. DOI: 10.1088/2041-8205/776/2/L19. arXiv: 1309.5933 [astro-ph.GA].

Dickey, J. M. et al. (2009). "The Outer Disk of the Milky Way Seen in λ21 cm Absorption". In: *ApJ* 693.2, pp. 1250–1260. DOI: 10.1088/0004-637X/693/2/1250. arXiv: 0901.0968 [astro-ph.GA].

Dwek, E. et al. (1995). "Morphology, near-infrared luminosity, and mass of the Galactic bulge from COBE DIRBE observations". In: *ApJ* 445, pp. 716–730. DOI: 10.1086/175734.

Einasto, J. (1974). "Galactic Models and Stellar Orbits". In: *Stars and the Milky Way System*. Ed. by L. N. Mavridis. Vol. 2, p. 169.

— (1979). "Galactic mass modeling". In: *The Large-Scale Characteristics of the Galaxy*. Ed. by W. B. Burton. Vol. 84. IAU Symposium, pp. 451–458.

Ferrière, K. M. (2001). "The interstellar environment of our galaxy". In: *Rev. Mod. Phys.* 73 (4), pp. 1031–1066. DOI: 10.1103/RevModPhys.73.1031. URL: https://link.aps.org/doi/10.1103/RevModPhys.73.1031.

Freeman, K. C. (1970). "On the Disks of Spiral and S0 Galaxies". In: *ApJ* 160, p. 811. DOI: 10.1086/150474.

Freudenreich, H. T. (1998). "A COBE Model of the Galactic Bar and Disk". In: *ApJ* 492, pp. 495–510. DOI: 10.1086/305065. eprint: astro-ph/9707340.

García Pérez, A. E. et al. (2018). "The Bulge Metallicity Distribution from the APOGEE Survey". In: *ApJ* 852.2, 91, p. 91. DOI: 10.3847/1538-4357/aa9d88. arXiv: 1712.01297 [astro-ph.GA].

Girardi, L. (1999). "A secondary clump of red giant stars: why and where". In: *MNRAS* 308, pp. 818–832. DOI: 10.1046/j.1365-8711.1999.02746.x. eprint: astro-ph/9901319.

— (2016). "Red Clump Stars". In: *ARA&A* 54, pp. 95–133. DOI: 10.1146/annurev-astro-081915-023354.

Gonzalez, O. A. et al. (2018). "The structure behind the Galactic bar traced by red clump stars in the VVV survey". In: *MNRAS* 481.1, pp. L130–L135. DOI: 10.1093/mnrasl/sly171. arXiv: 1809.03792 [astro-ph.GA].

Goodenough, L. et al. (2009). "Possible Evidence For Dark Matter Annihilation In The Inner Milky Way From The Fermi Gamma Ray Space Telescope". In: *arXiv e-prints*, arXiv:0910.2998, arXiv:0910.2998. arXiv: 0910.2998 [hep-ph].

Gordon, C. et al. (2013). "Dark matter and pulsar model constraints from Galactic Center Fermi-LAT gamma-ray observations". In: *Phys. Rev. D* 88 (8), p. 083521. DOI: 10.1103/PhysRevD.88.083521. URL: https://link.aps.org/doi/10.1103/PhysRevD.88.083521.

Gravity Collaboration et al. (2019). "A geometric distance measurement to the Galactic center black hole with 0.3% uncertainty". In: *A&A* 625, L10, p. L10. DOI: 10.1051/0004-6361/201935656. arXiv: 1904.05721 [astro-ph.GA].

Grenier, I. A. et al. (2005). "Unveiling Extensive Clouds of Dark Gas in the Solar Neighborhood". In: *Science* 307.5713, pp. 1292–1295. DOI: 10.1126/science.1106924.

Grenier, I. A. et al. (2015). "The Nine Lives of Cosmic Rays in Galaxies". In: *ARA&A* 53, pp. 199–246. DOI: 10.1146/annurev-astro-082214-122457.

Haggard, D. et al. (2017). "Low mass X-ray binaries in the Inner Galaxy: implications for millisecond pulsars and the GeV excess". In: *JCAP* 2017.5, 056, p. 056. DOI: 10.1088/1475-7516/2017/05/056. arXiv: 1701.02726 [astro-ph.HE].

Hajdu, G. et al. (2019). "On the optimal calibration of VVV photometry". In: *arXiv e-prints*, arXiv:1908.06160, arXiv:1908.06160. arXiv: 1908.06160 [astro-ph.IM].

Hall, O. J. et al. (2019). "Testing asteroseismology with Gaia DR2: hierarchical models of the Red Clump". In: *MNRAS* 486.3, pp. 3569–3585. DOI: 10.1093/mnras/stz1092. arXiv: 1904.07919 [astro-ph.SR].

Han, D. et al. (2018). "On the claimed X-shaped structure in the Milky Way bulge". In: *Rediscovering Our Galaxy*. Ed. by C. Chiappini et al. Vol. 334. IAU Symposium, pp. 263–264. DOI: 10.1017/S1743921317006470. arXiv: 1801.03940 [astro-ph.GA].

Harris, W. E. (2010). "A New Catalog of Globular Clusters in the Milky Way". In: *arXiv e-prints*, arXiv:1012.3224, arXiv:1012.3224. arXiv: 1012.3224 [astro-ph.GA].

Heiles, C. et al. (2003). "VizieR Online Data Catalog: Millennium Arecibo 21-cm Survey (Heiles+, 2003)". In: *VizieR Online Data Catalog* 214.

Hoof, S. et al. (2018). "A Global Analysis of Dark Matter Signals from 27 Dwarf Spheroidal Galaxies using Ten Years of Fermi-LAT Observations". In: *arXiv e-prints*, arXiv:1812.06986, arXiv:1812.06986. arXiv: 1812.06986 [astro-ph.CO].

Hooper, D. et al. (2011a). "Dark matter annihilation in the Galactic Center as seen by the Fermi Gamma Ray Space Telescope". In: *Physics Letters B* 697.5, pp. 412–428. DOI: 10.1016/j.physletb.2011.02.029. arXiv: 1010.2752 [hep-ph].

Hooper, D. et al. (2011b). "Origin of the gamma rays from the Galactic Center". In: *Phys. Rev. D* 84.12, 123005, p. 123005. DOI: 10.1103/PhysRevD.84.123005. arXiv: 1110.0006 [astro-ph.HE].

IceCube Collaboration et al. (2018). "Multimessenger observations of a flaring blazar coincident with high-energy neutrino IceCube-170922A". In: *Science* 361.6398, eaat1378, eaat1378. DOI: 10.1126/science.aat1378. arXiv: 1807.08816 [astro-ph.HE].

Ivanova, N. et al. (2008). "Formation and evolution of compact binaries in globular clusters - II. Binaries with neutron stars". In: *MNRAS* 386.1, pp. 553–576. DOI: 10.1111/j.1365-2966.2008.13064.x. arXiv: 0706.4096 [astro-ph].

Jaynes, E. T. (1957a). "Information Theory and Statistical Mechanics". In: *Physical Review* 106.4, pp. 620–630. DOI: 10.1103/PhysRev.106.620.

— (1957b). "Information Theory and Statistical Mechanics. II". In: *Physical Review* 108.2, pp. 171–190. DOI: 10.1103/PhysRev.108.171.

Joo, S.-J. et al. (2017). "New Insight on the Origin of the Double Red Clump in the Milky Way Bulge". In: *ApJ* 840, 98, p. 98. DOI: 10.3847/1538-4357/aa6d4f. arXiv: 1609.01294.

Kalberla, P. M. W. et al. (2005). "The Leiden/Argentine/Bonn (LAB) Survey of Galactic HI. Final data release of the combined LDS and IAR surveys with improved stray-radiation corrections". In: *A&A* 440.2, pp. 775–782. DOI: 10.1051/0004-6361:20041864. arXiv: astro-ph/0504140 [astro-ph].

Kalberla, P. M. W. et al. (2009). "The Hi Distribution of the Milky Way". In: *ARA&A* 47, pp. 27–61. DOI: 10.1146/annurev-astro-082708-101823.

Kataoka, J. et al. (2013). "Suzaku Observations of the Diffuse X-Ray Emission across the Fermi Bubbles' Edges". In: *ApJ* 779.1, 57, p. 57. DOI: 10.1088/0004-637X/779/1/57. arXiv: 1310.3553 [astro-ph.HE].

Kataoka, J. et al. (2015). "Global Structure of Isothermal Diffuse X-Ray Emission along the Fermi Bubbles". In: *ApJ* 807.1, 77, p. 77. DOI: 10.1088/0004-637X/807/1/77. arXiv: 1505.05936 [astro-ph.HE].

Kim, S. Y. et al. (2017). "There is No Missing Satellites Problem". In: *arXiv e-prints*, arXiv:1711.06267, arXiv:1711.06267. arXiv: 1711.06267 [astro-ph.CO].

Kormendy, J. et al. (2004). "Secular Evolution and the Formation of Pseudobulges in Disk Galaxies". In: *ARA&A* 42.1, pp. 603–683. DOI: 10.1146/annurev.astro.42.053102.134024. arXiv: astro-ph/0407343 [astro-ph].

Lang, D. (2014). "unWISE: Unblurred Coadds of the WISE Imaging". In: *Astronom. J.* 147.5, 108, p. 108. DOI: 10.1088/0004-6256/147/5/108. arXiv: 1405.0308 [astro-ph.IM].

Leane, R. K. et al. (2019). "Dark Matter Strikes Back at the Galactic Center". In: *arXiv e-prints*, arXiv:1904.08430, arXiv:1904.08430. arXiv: 1904.08430 [astro-ph.HE].

Lee, S. K. et al. (2016). "Evidence for Unresolved γ -Ray Point Sources in the Inner Galaxy". In: *Phys. Rev. Lett.*, 116.5, 051103, p. 051103. DOI: 10.1103/PhysRevLett.116.051103. arXiv: 1506.05124 [astro-ph.HE].

Lee, Y.-W. et al. (2019). "The Globular Cluster Origin of the Milky Way Outer Bulge: Evidence from Sodium Bimodality". In: *ApJ* 878.1, L2, p. L2. DOI: 10.3847/2041-8213/ab22bc. arXiv: 1905.08809 [astro-ph.GA].

Lemoine, M. et al. (2015). "On ultra-high energy cosmic ray acceleration at the termination shock of young pulsar winds". In: *JCAP* 2015.7, 016, p. 016. DOI: 10.1088/1475-7516/2015/07/016. arXiv: 1409.0159 [astro-ph.HE].

Linden, T. et al. (2012). "The Morphology of Hadronic Emission Models for the Gamma-Ray Source at the Galactic Center". In: *ApJ* 753.1, 41, p. 41. DOI: 10.1088/0004-637X/753/1/41. arXiv: 1203.3539 [astro-ph.HE].

López-Corredoira, M. (2016). "A case against an X-shaped structure in the Milky Way young bulge". In: *A&A* 593, A66, A66. DOI: 10.1051/0004-6361/201527074. arXiv: 1606.09627.

— (2017). "Absence of an X-shaped Structure in the Milky Way Bulge Using Mira Variable Stars". In: *ApJ* 836, 218, p. 218. DOI: 10.3847/1538-4357/836/2/218. arXiv: 1702.02539.

López-Corredoira, M. et al. (2000). "Inversion of stellar statistics equation for the Galactic bulge". In: *MNRAS* 313.2, pp. 392–410. DOI: 10.1046/j.1365-8711.2000.03220.x. arXiv: astro-ph/9911182 [astro-ph].

López-Corredoira, M. et al. (2019). "Distribution of red clump stars does not support the X-shaped Galactic bulge". In: *A&A* 627, A3, A3. DOI: 10.1051/0004-6361/201935571. arXiv: 1905.13592 [astro-ph.GA].

Maccione, L. et al. (2011). *DRAGON: Galactic Cosmic Ray Diffusion Code*. ascl: 1106.011.

Macias, O. et al. (2014). "Contribution of cosmic rays interacting with molecular clouds to the Galactic Center gamma-ray excess". In: *Phys. Rev. D* 89.6, 063515, p. 063515. DOI: 10.1103/PhysRevD.89.063515. arXiv: 1312.6671 [astro-ph.HE].

Macias, O. et al. (2018). "Galactic bulge preferred over dark matter for the Galactic centre gamma-ray excess". In: *Nature Astronomy* 2, pp. 387–392. DOI: 10.1038/s41550-018-0414-3. arXiv: 1611.06644 [astro-ph.HE].

Macias, O. et al. (2019). "Strong evidence that the galactic bulge is shining in gamma rays". In: *JCAP* 2019.9, 042, p. 042. DOI: 10.1088/1475-7516/2019/09/042. arXiv: 1901.03822 [astro-ph.HE].

Maraston, C. (1998). "Evolutionary synthesis of stellar populations: a modular tool". In: *MNRAS* 300.3, pp. 872–892. DOI: 10.1046/j.1365-8711.1998.01947.x. arXiv: astro-ph/9807338 [astro-ph].

Marigo, P. et al. (2017). "A New Generation of PARSEC-COLIBRI Stellar Isochrones Including the TP-AGB Phase". In: *ApJ* 835.1, 77, p. 77. DOI: 10.3847/1538-4357/835/1/77. arXiv: 1701.08510 [astro-ph.SR].

McWilliam, A. et al. (2010). "Two Red Clumps and the X-shaped Milky Way Bulge". In: *ApJ* 724, pp. 1491–1502. DOI: 10.1088/0004-637X/724/2/1491. arXiv: 1008.0519.

Merritt, D. et al. (2006). "Empirical Models for Dark Matter Halos. I. Nonparametric Construction of Density Profiles and Comparison with Parametric Models". In: *Astronom. J.* 132.6, pp. 2685–2700. DOI: 10.1086/508988. arXiv: astro-ph/0509417 [astro-ph].

Mills, E. A. C. (2017). "The Milky Way's Central Molecular Zone". In: *arXiv e-prints*, arXiv:1705.05332, arXiv:1705.05332. arXiv: 1705.05332 [astro-ph.GA].

Minniti, D. et al. (2010). "VISTA Variables in the Via Lactea (VVV): The public ESO near-IR variability survey of the Milky Way". In: *New Astron.* 15.5, pp. 433–443. DOI: 10.1016/j.newast.2009.12.002. arXiv: 0912.1056 [astro-ph.GA].

Moskalenko, I. V. et al. (1998). "Production and Propagation of Cosmic-Ray Positrons and Electrons". In: *ApJ* 493.2, pp. 694–707. DOI: 10.1086/305152. arXiv: astro-ph/9710124 [astro-ph].

— (2000). "Anisotropic Inverse Compton Scattering in the Galaxy". In: *ApJ* 528.1, pp. 357–367. DOI: 10.1086/308138. arXiv: astro-ph/9811284 [astro-ph].

Nakanishi, H. et al. (2003). "Three-Dimensional Distribution of the ISM in the Milky Way Galaxy: I. The H I Disk". In: *PASJ* 55, pp. 191–202. DOI: 10.1093/pasj/55.1.191. eprint: astro-ph/0304338.

Nataf, D. M. et al. (2010). "The Split Red Clump of the Galactic Bulge from OGLE-III". In: *ApJ* 721.1, pp. L28–L32. DOI: 10.1088/2041-8205/721/1/L28. arXiv: 1007.5065 [astro-ph.GA].

Navarro, J. F. et al. (1996). "The Structure of Cold Dark Matter Halos". In: *ApJ* 462, p. 563. DOI: 10.1086/177173. eprint: astro-ph/9508025.

Ness, M. et al. (2016). "The X-shaped Bulge of the Milky Way Revealed by WISE". In: *Astronom. J.* 152.1, 14, p. 14. DOI: 10.3847/0004-6256/152/1/14. arXiv: 1603.00026 [astro-ph.GA].

Ness, M. et al. (2013). "ARGOS - IV. The kinematics of the Milky Way bulge". In: *MNRAS* 432.3, pp. 2092–2103. DOI: 10.1093/mnras/stt533. arXiv: 1303.6656 [astro-ph.GA].

Nishiyama, S. et al. (2013). "Magnetically Confined Interstellar Hot Plasma in the Nuclear Bulge of Our Galaxy". In: *ApJ* 769.2, L28, p. L28. DOI: 10.1088/2041-8205/769/2/L28. arXiv: 1305.0347 [astro-ph.GA].

Nogueras-Lara, F. et al. (2019). "The nuclear disc of the Milky Way: Early formation, long quiescence, and starburst activity one billion years ago". In: *arXiv e-prints*, arXiv:1910.06968, arXiv:1910.06968. arXiv: 1910.06968 [astro-ph.GA].

Oakes, L. (2019). "Combined Dark Matter Searches Towards Dwarf Spheroidal Galaxies with Fermi-LAT, HAWC, HESS, MAGIC and VERITAS". In: *36th International Cosmic Ray Conference (ICRC2019)*. Vol. 36. International Cosmic Ray Conference, p. 539. arXiv: 1909.06310 [astro-ph.HE].

O'Leary, R. M. et al. (2015). "Young Pulsars and the Galactic Center GeV Gamma-ray Excess". In: *arXiv e-prints*, arXiv:1504.02477, arXiv:1504.02477. arXiv: 1504.02477 [astro-ph.HE].

Pato, M. et al. (2015). "The Dark Matter Profile of the Milky Way: A Non-parametric Reconstruction". In: *ApJ* 803.1, L3, p. L3. DOI: 10.1088/2041-8205/803/1/L3. arXiv: 1504.03317 [astro-ph.GA].

Pietrinferni, A. et al. (2004). "A Large Stellar Evolution Database for Population Synthesis Studies. I. Scaled Solar Models and Isochrones". In: *ApJ* 612.1, pp. 168–190. DOI: 10.1086/422498. arXiv: astro-ph/0405193 [astro-ph].

Ploeg, H. et al. (2017). "Consistency between the luminosity function of resolved millisecond pulsars and the galactic center excess". In: *JCAP* 2017.8, 015, p. 015. DOI: 10.1088/1475-7516/2017/08/015. arXiv: 1705.00806 [astro-ph.HE].

Pohl, M. et al. (2008). "Three-Dimensional Distribution of Molecular Gas in the Barred Milky Way". In: *ApJ* 677.1, pp. 283–291. DOI: 10.1086/529004. arXiv: 0712.4264 [astro-ph].

Portail, M. et al. (2017). "Dynamical modelling of the galactic bulge and bar: the Milky Way's pattern speed, stellar and dark matter mass distribution". In: *MNRAS* 465.2, pp. 1621–1644. DOI: 10.1093/mnras/stw2819. arXiv: 1608.07954 [astro-ph.GA].

Portail, M. et al. (2015). "Made-to-measure models of the Galactic box/peanut bulge: stellar and total mass in the bulge region". In: *MNRAS* 448, pp. 713–731. DOI: 10.1093/mnras/stv058. arXiv: 1502.00633.

Porter, T. A. et al. (2017). "High-Energy Gamma Rays from the Milky Way: Three-Dimensional Spatial Models for the Cosmic-Ray and Radiation Field Densities in the Interstellar Medium". In: *Astrophys. J.* 846.1, p. 67. DOI: 10.3847/1538-4357/aa844d. arXiv: 1708.00816 [astro-ph.HE].

Rattenbury, N. J. et al. (2007). "Modelling the Galactic bar using OGLE-II red clump giant stars". In: *MNRAS* 378, pp. 1064–1078. DOI: 10.1111/j.1365-2966.2007.11843.x. arXiv: 0704.1614.

Renaud, F. et al. (2013). "A sub-parsec resolution simulation of the Milky Way: global structure of the interstellar medium and properties of molecular clouds". In: *MNRAS* 436, pp. 1836–1851. DOI: 10.1093/mnras/stt1698. arXiv: 1307.5639.

Ricker, N. (1943). "Further developments in the wavelet theory of seismogram structure*". In: *Bulletin of the Seismological Society of America* 33.3, pp. 197–228. ISSN: 0037-1106. eprint: https://pubs.geoscienceworld.org/bssa/article-pdf/33/3/197/2690607/BSSA0330030197.pdf.

Robin, A. C. et al. (2003). "A synthetic view on structure and evolution of the Milky Way". In: *A&A* 409, pp. 523–540. DOI: 10.1051/0004-6361:20031117.

Robin, A. C. et al. (2012). "Stellar populations in the Milky Way bulge region: towards solving the Galactic bulge and bar shapes using 2MASS data". In: *A&A* 538, A106, A106. DOI: 10.1051/0004-6361/201116512. arXiv: 1111.5744 [astro-ph.GA].

Robin, A. C. et al. (2014). "Constraining the thick disc formation scenario of the Milky Way". In: *A&A* 569, A13, A13. DOI: 10.1051/0004-6361/201423415. arXiv: 1406.5384 [astro-ph.GA].

Rojas-Arriagada, A. et al. (2014). "The Gaia-ESO Survey: metallicity and kinematic trends in the Milky Way bulge". In: *A&A* 569, A103, A103. DOI: 10.1051/0004-6361/201424121. arXiv: 1408.4558.

Roszkowski, L. et al. (2018). "WIMP dark matter candidates and searches—current status and future prospects". In: *Reports on Progress in Physics* 81.6, 066201, p. 066201. DOI: 10.1088/1361-6633/aab913. arXiv: 1707.06277 [hep-ph].

Saito, R. K. et al. (2012). "VVV DR1: The first data release of the Milky Way bulge and southern plane from the near-infrared ESO public survey VISTA variables in the Vía Láctea". In: *A&A* 537, A107, A107. DOI: 10.1051/0004-6361/201118407. arXiv: 1111.5511 [astro-ph.GA].

Sanders, J. L. et al. (2019). "Transverse kinematics of the Galactic bar-bulge from VVV and Gaia". In: *MNRAS*, p. 1626. DOI: 10.1093/mnras/stz1630. arXiv: 1903.02008 [astro-ph.GA].

Schlegel, D. J. et al. (1998). "Maps of Dust Infrared Emission for Use in Estimation of Reddening and Cosmic Microwave Background Radiation Foregrounds". In: *ApJ* 500.2, pp. 525–553. DOI: 10.1086/305772. arXiv: astro-ph/9710327 [astro-ph].

Sharma, S. et al. (2011). "Galaxia: A Code to Generate a Synthetic Survey of the Milky Way". In: *ApJ* 730.1, 3, p. 3. DOI: 10.1088/0004-637X/730/1/3. arXiv: 1101.3561 [astro-ph.GA].

Simion, I. T. et al. (2017). "A parametric description of the 3D structure of the Galactic bar/bulge using the VVV survey". In: *MNRAS* 471.4, pp. 4323–4344. DOI: 10.1093/mnras/stx1832. arXiv: 1707.06660 [astro-ph.GA].

Skrutskie, M. F. et al. (2006). "The Two Micron All Sky Survey (2MASS)". In: *Astronom. J.* 131, pp. 1163–1183. DOI: 10.1086/498708.

Sofue, Y. (2015). "Dark halos of M 31 and the Milky Way". In: *PASJ* 67.4, 75, p. 75. DOI: 10.1093/pasj/psv042. arXiv: 1504.05368 [astro-ph.GA].

Solomon, P. M. et al. (1987). "Mass, luminosity, and line width relations of Galactic molecular clouds". In: *ApJ* 319, pp. 730–741. DOI: 10.1086/165493.

Spera, M. et al. (2015). "The mass spectrum of compact remnants from the PARSEC stellar evolution tracks". In: *MNRAS* 451.4, pp. 4086–4103. DOI: 10.1093/mnras/stv1161. arXiv: 1505.05201 [astro-ph.SR].

Stanek, K. Z. et al. (1997). "Modeling the Galactic Bar Using Red Clump Giants". In: *ApJ* 477.1, pp. 163–175. DOI: 10.1086/303702. arXiv: astro-ph/9605162 [astro-ph].

Storm, E. et al. (2017). "SkyFACT: high-dimensional modeling of gamma-ray emission with adaptive templates and penalized likelihoods". In: *JCAP* 2017.8, 022, p. 022. DOI: 10.1088/1475-7516/2017/08/022. arXiv: 1705.04065 [astro-ph.HE].

Strigari, L. E. (2018). "Dark matter in dwarf spheroidal galaxies and indirect detection: a review". In: *Reports on Progress in Physics* 81.5, 056901, p. 056901. DOI: 10.1088/1361-6633/aaae16. arXiv: 1805.05883 [astro-ph.CO].

Strong, A. W. et al. (1998). "Propagation of Cosmic-Ray Nucleons in the Galaxy". In: *ApJ* 509.1, pp. 212–228. DOI: 10.1086/306470. arXiv: astro-ph/9807150 [astro-ph].

Su, M. et al. (2010). "Giant Gamma-ray Bubbles from Fermi-LAT: Active Galactic Nucleus Activity or Bipolar Galactic Wind?" In: *ApJ* 724.2, pp. 1044–1082. DOI: 10.1088/0004-637X/724/2/1044. arXiv: 1005.5480 [astro-ph.HE].

Surot, F. et al. (2019). "Mapping the stellar age of the Milky Way bulge with the VVV. II. Deep JKs catalogs release based on PSF photometry". In: *arXiv e-prints*, arXiv:1907.01972, arXiv:1907.01972. arXiv: 1907.01972 [astro-ph.GA].

Tahara, M. et al. (2015). "Suzaku X-Ray Observations of the Fermi Bubbles: Northernmost Cap and Southeast Claw Discovered With MAXI-SSC". In: *ApJ* 802.2, 91, p. 91. DOI: 10.1088/0004-637X/802/2/91. arXiv: 1501.04405 [astro-ph.HE].

Tan, A. et al. (2016). "Dark Matter Results from First 98.7 Days of Data from the PandaX-II Experiment". In: *Phys. Rev. Lett.,* 117.12, 121303, p. 121303. DOI: 10.1103/PhysRevLett.117.121303. arXiv: 1607.07400 [hep-ex].

Toomre, A. (1963). "On the Distribution of Matter Within Highly Flattened Galaxies." In: *ApJ* 138, p. 385. DOI: 10.1086/147653.

Udalski, A. et al. (1992). "The Optical Gravitational Lensing Experiment". In: *Acta Astron.* 42, pp. 253–284.

Vásquez, S. et al. (2013). "3D kinematics through the X-shaped Milky Way bulge". In: *A&A* 555, A91, A91. DOI: 10.1051/0004-6361/201220222. arXiv: 1304.6427 [astro-ph.GA].

Wegg, C. et al. (2013). "Mapping the three-dimensional density of the Galactic bulge with VVV red clump stars". In: *MNRAS* 435.3, pp. 1874–1887. DOI: 10.1093/mnras/stt1376. arXiv: 1308.0593 [astro-ph.GA].

Wegg, C. et al. (2015). "The structure of the Milky Way's bar outside the bulge". In: *MNRAS* 450, pp. 4050–4069. DOI: 10.1093/mnras/stv745. arXiv: 1504.01401.

Weiland, J. L. et al. (1994). "COBE diffuse infrared background experiment observations of the galactic bulge". In: *ApJ* 425, pp. L81–L84. DOI: 10.1086/187315.

Wilks, S. S. (1938). "The Large-Sample Distribution of the Likelihood Ratio for Testing Composite Hypotheses". In: *Ann. Math. Statist.* 9.1, pp. 60–62. DOI: 10.1214/aoms/1177732360. URL: https://doi.org/10.1214/aoms/1177732360.

Wolleben, M. (2007). "A New Model for the Loop I (North Polar Spur) Region". In: *ApJ* 664.1, pp. 349–356. DOI: 10.1086/518711. arXiv: 0704.0276 [astro-ph].

Wright, E. L. et al. (2010). "The Wide-field Infrared Survey Explorer (WISE): Mission Description and Initial On-orbit Performance". In: *Astronom. J.* 140, pp. 1868–1881. DOI: 10.1088/0004-6256/140/6/1868. arXiv: 1008.0031 [astro-ph.IM].

Yuan, Q. et al. (2014). "Millisecond pulsar interpretation of the Galactic center gamma-ray excess". In: *Journal of High Energy Astrophysics* 3-4, pp. 1–8. ISSN: 2214-4048. DOI: https://doi.org/10.1016/j.jheap.2014.06.001. URL: http://www.sciencedirect.com/science/article/pii/S2214404814000147.

Zavala, J. et al. (2019). "Dark Matter Haloes and Subhaloes". In: *Galaxies* 7.4, p. 81. DOI: 10.3390/galaxies7040081. arXiv: 1907.11775 [astro-ph.CO].

Zoccali, M. et al. (2008). "The metal content of bulge field stars from FLAMES-GIRAFFE spectra. I. Stellar parameters and iron abundances". In: *A&A* 486.1, pp. 177–189. DOI: 10.1051/0004-6361:200809394. arXiv: 0805.1218 [astro-ph].

Zoccali, M. et al. (2017). "The GIRAFFE Inner Bulge Survey (GIBS). III. Metallicity distributions and kinematics of 26 Galactic bulge fields". In: *A&A* 599, A12, A12. DOI: 10.1051/0004-6361/201629805. arXiv: 1610.09174 [astro-ph.GA].

Appendix A

Analytic Likelihood Gradient

The analytic gradient of $\ln \mathcal{L}$ were determined as follows. We take ρ to be a field over (s, l, b) so that a single density value, $\rho_\delta = \rho(s, l, b) = \rho_{h,j,k}$ where $\{h', j', k'\} \in \{s, l, b\}$. Each of the ρ_δ represents a free parameter in our model. The gradient of $\ln \mathcal{L}$ with respect to ρ_δ is then

$$\frac{\partial}{\partial \rho_\delta} \ln \mathcal{L} = \frac{\partial}{\partial \rho_\delta} \ln \mathcal{L}_{\mathrm{P}} + \frac{\partial}{\partial \rho_\delta} \ln \mathcal{L}_{\mathrm{MEM}} + \frac{\partial}{\partial \rho_\delta} \ln \mathcal{L}_{\mathrm{smooth}} \tag{A.1}$$

where $\ln \mathcal{L}_{\mathrm{P}}$ is the Poisson log-likelihood, $\ln \mathcal{L}_{\mathrm{MEM}}$ is the maximum entropy penalty term and $\ln \mathcal{L}_{\mathrm{smooth}}$ is the smoothness penalty term. The gradient of the Poisson term is then

$$\frac{\partial}{\partial \rho_\delta} \ln \mathcal{L}_{\mathrm{P}} = \sum_{\{i,j,k\} \in \{K_s, l, b\}} \left(\frac{n_{i,j,k}}{N_{i,j,k}} - 1 \right) \left(\frac{\partial N}{\partial \rho_\delta} \right)_{i,j,k} \tag{A.2}$$

where the derivative of the model, N, is determined by differentiating Eq. 3.4 with respect to ρ_δ so that

$$\left(\frac{\partial N}{\partial \rho_\delta} \right)_{i,j,k} = \Delta\Omega \Delta K_s \left(\int_4^{13} \frac{\partial \rho}{\partial \rho_\delta} \Phi \left(K_s - 5 \log s - 10 \right) s^2 \, \mathrm{d}s \right)_{i,j,k} . \tag{A.3}$$

The integral above can be approximated by the midpoint rule:

$$\left(\frac{\partial N}{\partial \rho_\delta}\right)_{i,j,k} = \Delta\Omega\Delta K_s \Delta s \left(\sum_{h\in s}\left(\frac{\partial \rho}{\partial \rho_\delta}\right)_{h,j,k} \Phi_{h,i,j,k} s_h^2\right)_{i,j,k} \tag{A.4}$$

Where $\Phi_{h,i,j,k}$ is the discretised version of the luminosity function which needs an index for s, K_s, l, and b. Since ρ_δ is single value at $(h,j,k) = (h',j',k')$ in the field ρ, then $\frac{\partial \rho}{\partial \rho_\delta} = \delta_{hh'}\delta_{jj'}\delta_{kk'}$, where the δ here are the Kronecker delta. Substituting this into Eq. A.4 and simplifying gives

$$\left(\frac{\partial N}{\partial \rho_\delta}\right)_{i,j,k} = \Delta\Omega\Delta K_s \Delta s\, \delta_{jj'}\delta_{kk'}\Phi_{h',i,j,k} s_{h'}^2\,. \tag{A.5}$$

Substituting Eq. A.5 into Eq. A.2 gives the final form of the Poisson component of the gradient as

$$\frac{\partial}{\partial \rho_\delta} \ln \mathcal{L}_{\mathrm{P}} = \Delta\Omega\Delta K_s \Delta s \sum_{i\in K_s}\left(\frac{n_{i,j',k'}}{N_{i,j',k'}} - 1\right)\Phi_{h',i,j',k'} s_{h'}^2. \tag{A.6}$$

The gradient for the Poisson component is equal to zero when $n = N$, so that the log-likelihood has an extremum when the model, N, and the data, n, are equal.

The gradient of the maximum entropy penalty was determined by taking the derivative of Eq. 3.5 with respect to ρ_δ and applying the chain rule

$$\frac{\partial}{\partial \rho_\delta} \ln \mathcal{L}_{\mathrm{MEM}} = \frac{\partial}{\partial \kappa}\left(-\lambda \sum_{\{h,j,k\}\in\{s,l,b\}} (1 - \kappa_{i,j,k} + \kappa_{i,j,k} \ln \kappa_{i,j,k})\right)\frac{\partial \kappa}{\partial \rho_\delta} \tag{A.7}$$

where $\kappa = \frac{\rho}{\rho_{\mathrm{prior}}}$ is the ratio between the density field and a smooth prior estimate, ρ_{prior}. Evaluating the derivative in Eq. A.7 and substituting in $\frac{\partial \kappa}{\partial \rho_\delta} = \frac{1}{(\rho_{\mathrm{prior}})_\delta}$ gives

$$\frac{\partial}{\partial \rho_\delta} \ln \mathcal{L}_{\mathrm{MEM}} = -\frac{\lambda}{(\rho_{\mathrm{prior}})_\delta} \ln\left[\frac{\rho_\delta}{(\rho_{\mathrm{prior}})_\delta}\right], \tag{A.8}$$

which equals zero (thus giving the extremum) when $\rho_\delta = (\rho_{\text{prior}})_\delta$. It follows from this equation that

$$\frac{\partial^2}{\partial \kappa_\delta^2} \ln \mathcal{L}_{\text{MEM}} \bigg|_{\kappa_\delta = 1} = -\lambda. \tag{A.9}$$

We can then evaluate the expected deviation from the prior using the standard Gaussian approximation for estimating errors in maximum likelihood:

$$\sigma_{\text{MEM}} \equiv \sigma_\kappa = \left(- \frac{\partial^2}{\partial \rho_\delta^2} \ln \mathcal{L}_{\text{MEM}} \bigg|_{\rho_\delta = (\rho_{\text{prior}})_\delta} \right)^{-1/2} = \frac{1}{\sqrt{\lambda}} \tag{A.10}$$

The gradient of the smoothing term was obtained by direct differentiation of the last three lines of Eq. 3.10 so that

$$\begin{aligned}
\frac{\partial}{\partial \rho_\delta} \ln \mathcal{L}_{\text{smooth}} = & \\
& - \frac{\eta_s}{\rho_\delta} [(\ln \rho_{h'-2,j',k'} - 4 \ln \rho_{h'-1,j',k'} + 6 \ln \rho_{h',j',k'} \\
& -4 \ln \rho_{h'+1,j',k'} + \ln \rho_{h'+2,j',k'})] \\
& - \frac{\eta_l}{\rho_\delta} [(\ln \rho_{h',j'-2,k'} - 4 \ln \rho_{h',j'-1,k'} + 6 \ln \rho_{h',j',k'} \\
& -4 \ln \rho_{h',j'+1,k'} + \ln \rho_{h',j'+2,k'})] \\
& - \frac{\eta_b}{\rho_\delta} [(\ln \rho_{h',j',k'-2} - 4 \ln \rho_{h',j',k'-1} + 6 \ln \rho_{h',j',k'} \\
& -4 \ln \rho_{h',j',k'+1} + \ln \rho_{h',j',k'+2})]
\end{aligned} \tag{A.11}$$

It is easy to check by that this equation is equal to zero when $\rho_{h,j,k}$ is an exponential function of the form:

$$\rho_{h,j,k} = A \exp(A_h h + A_j j + A_k k) \tag{A.12}$$

where A, A_h, A_j, and A_k are constants. It follows from Eqs. A.11 and A.12 that the relative deviation from an exponential function is given by:

$$\sigma_{\text{curvature}} \equiv \frac{\sigma_\rho}{\rho_\delta} = \frac{1}{\sqrt{6\eta}}. \tag{A.13}$$